ACQUISITION AND QUANTIFICATION TECHNIQUES FOR PROTON MAGNETIC RESONANCE SPECTROSCOPY AT 7 T

Dong Hyun Hong

Eriwn L. Hahn Institute for Magnetic Resonance Imaging

ISBN: 978-94-6380-583-4

LAY-OUT: Proefschriftmaken

PRINT: Proefschriftmaken | https://www.proefschriftmaken.nl

Acquisition and quantification techniques for proton magnetic resonance spectroscopy at 7 T

Proefschrift

ter verkrijging van de graad van doctor aan de
Radboud Universiteit Nijmegen
op gezag van de
rector magnificus

prof. dr. J.H.J.M. van Krieken,

volgens besluit van het college van decanen
in het openbaar te verdedigen op

maandag 11 november 2019
om 12.30 uur precies

door

Dong Hyun Hong

geboren op 12 oktober 1981
te Seoul, Republiek Korea

Promotor:

Prof. dr. David. G. Norris

Manuscriptcommissie:

Prof. dr. Arend Heerschap
Prof. dr. Roland Kreis (universiteit Bern, Zwitserland)
Prof. dr. Jamie Near (McGill universiteit, Canada)

Acquisition and quantification techniques for proton magnetic resonance spectroscopy at 7 T

Doctoral Thesis

to obtain the degree of doctor from
Radboud University Nijmegen
on the authority of the
Rector Magnificus

prof. dr. J.H.J.M. van Krieken,

according to the decision of the Council of Deans
to be defended in public on

Monday, November 11, 2019
at 12.30 hours

by

Dong Hyun Hong

Born on October 12, 1981
in Seoul, Republic of Korea

Supervisor:

Prof. dr. David G. Norris

Doctoral Thesis Committee:

Prof. dr. Arend Heerschap
Prof. dr. Roland Kreis (University of Bern, Switzerland)
Prof. dr. Jamie Near (McGill University, Canada)

Table of Contents

This work was funded by the Helmholtz Alliance ICEMED – Imaging and Curing Environmental Metabolic Diseases, through the Initiative and Networking Fund of the Helmholtz Association.

CHAPTER 1.

Basic Principles

Block, and Purcell discovered nuclear magnetic resonance (NMR) in 1946 (Bloch, 1946; Purcell et al., 1946). Since then, NMR has made important contributions in physics, biology, chemistry, and medicine. Magnetic resonance spectroscopy (MRS) is one application of NMR, a widely used noninvasive technique to quantify the metabolic profiles of humans and animals. Proton (^{1}H) MRS enables the detection of metabolites with hydrogen-containing compounds in the voxel, playing a pivotal role in clinical and neuroscientific research.

This thesis aims to improve the sensitivity and reproducibility of acquisition for proton spectroscopy in the human brain. In particular, this work focuses on γ-aminobutyric acid (GABA) measurement and quantification using single-voxel spectroscopy (SVS) at 7 T.

1.1 Nuclear magnetic resonance spectroscopy

NMR exploits the magnetic properties of nuclei. In a strong magnetic field (i.e., a B_0 field), nuclei with non-zero spin quantum numbers will be distributed over various eigenstates according to the Boltzmann distribution (see Figure 1.1). Application of a radio-frequency (RF) pulse at the transition frequency will modify the relative population of the states, and in the appropriate circumstances, it can lead to the generation of transverse magnetization. NMR spectroscopy is based on the measurement of the electromotive force induced by the precession of the net magnetization according to Faraday's law. The specific resonance frequency depends on the strength of the magnetic field and the magnetic properties of the chemical environment of the nuclei. The NMR response to an RF pulse (i.e., free induction decay (FID)) is recorded in the time domain. After Fourier transforming the FID, a series of peaks can be visualized in the frequency domain, which corresponds to nuclei rotating frequency along a chemical shift axis after Fourier transform.

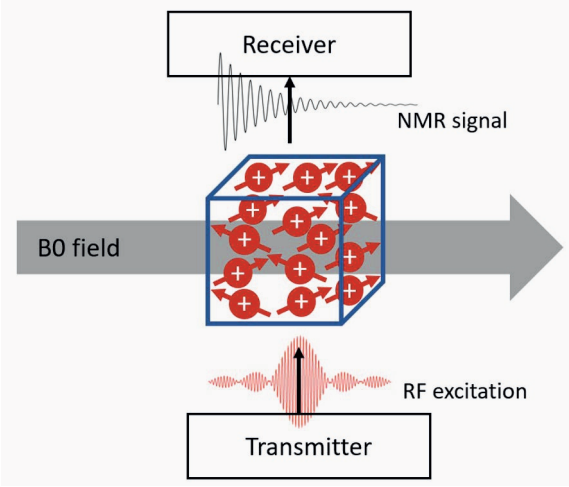

Figure 1.1 Concept of Nuclear Magnetic Resonance (NMR).

In a strong static field, nuclei are aligned with the magnetic field (α-spin status) or against the magnetic field (β-spin status). This phenomenon is called the Zeeman effect (see Figure 1.2). The intrinsic frequency of the precession is the Larmor frequency ω_0. The perturbation in the energy of the Zeeman state with magnetic quantum number m can be expressed as:

$$\Delta E = -\mu_0 B_0 = -m\hbar\gamma B_0 = m\hbar\omega_0 \tag{1.1}$$

where μ_0 denotes the magnetic dipole moment, B_0 is the static field strength, γ is a gyro magnetic ratio, and $\omega_0 = -\gamma B_0$ is the Larmor frequency,

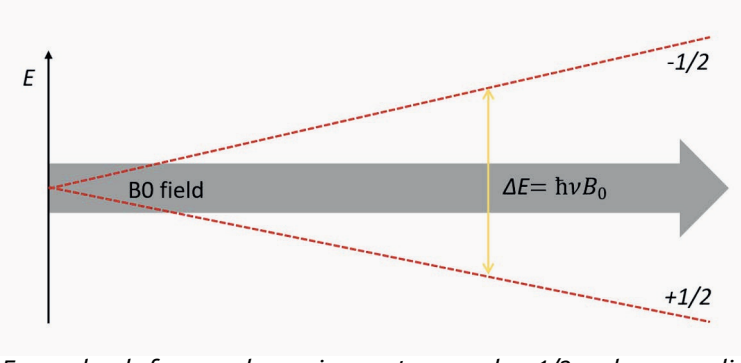

Figure 1.2. Energy levels for a nucleus spin quantum number 1/2 under an applied magnetic field.

For a spin ½ nucleus, the higher energy state (excited state) is defined as the α state, whereas the lower energy state (ground state) is defined as the β state. The difference in energy levels (ΔE) between the two states can be

written as:

$$\Delta E = \hbar \nu B_0 \tag{1.2}$$

where ħ is a Planck's constant, which is 6.663 × 10^{-34} J/s. Because $\Delta E = \hbar\omega$, the frequency of the required electromagnetic radiation for the transition has the form:

$$\omega = \gamma B_0. \tag{1.3}$$

The NMR signal intensity is owing to the population difference between the two Zeeman states at the transition. The Boltzmann distribution governs the populations of the energy states. The ratio of the populations in the states is quantitatively described by the Boltzmann equation:

$$\frac{N_\alpha}{N_\beta} = \mathrm{e}^{-\Delta E/kT} = \mathrm{e}^{-\gamma \hbar B_0/kT} \tag{1.4}$$

where N_α and N_β denote the population of α and β states, respectively, T is the absolute temperature, and k is the Boltzmann constant (1.3805 x 10^{-23} J/Kelvin)

1.2 Nuclei for MRS

Subatomic particles (protons and neutrons) of the nucleus contain an intrinsic property called spin. However, not all nuclei have nonzero spin. Nuclei that have both even atomic mass and even atomic number are NMR inactive (total spin = 0). All other nuclei that have an integer and half-integer nuclear spin quantum numbers (I) possess net spin. Table1.1 summarizes representative nuclei that show NMR phenomena, with their properties

Table 1.1. erties of nPropuclear spins that show NMR phenomena

Type	Number of protons (Z)	Number of neutrons (N)	Nuclear spin number (I)	Example nuclei
1	Even	Even	0	^{4}He, ^{12}C, ^{16}O, ^{32}S
2	Odd	Even	1/2, 3/2, 5/2, etc.	^{1}H (I = 1/2)
3	Even	Odd	1/2, 3/2, 5/2, etc.	^{13}C (I = 1/2), ^{15}N (I = 1/2)
4	Odd	Odd	1, 2, 3, etc.	^{2}H (I =1), ^{14}N (I = 1)

Most spectroscopy studies use the proton (^{1}H) nucleus because of its high natural abundancy and its high sensitivity because of its high gyromagnetic ratio (Y). In addition, proton spectroscopy is favorable because it can be performed with the same hardware used for MRI experiments. In addition to protons, other nuclei such as phosphorus (^{31}P), sodium (^{23}Na), and carbon

(^{13}C) are also widely used when appropriate MR hardware is available, e.g., RF coils and amplifiers. Table 1.2 summarizes potential nuclei for NMR spectroscopy with their gyromagnetic ratio, spin, and natural abundancy (James 1975).

Table 1.2. Properties of widely used nuclei for biological NMR studies

Nucleus	Symbol	Gyromagnetic ratio (Y) (MHz/T)	Spin	Natural abundancy (%)	Sensitivity (vs. ^{1}H) (%)
Proton	^{1}H	42.577	1/2	99.98	100
Phosphorus	^{31}P	17.235	1/2	100.00	6.63
Sodium	^{23}Na	11.262	3/2	100.00	9.27
Carbon	^{13}C	10.708	1/2	1.10	1.59
Nitrogen	^{15}N	-4.316	1/2	0.37	0.104
Oxygen	^{17}O	-5.772	5/2	0.04	3.70
Fluorine	^{19}F	40.052	1/2	100.00	83.3

1.3 Chemical shift

Nuclei in different molecular environments resonate at slightly different frequencies because the electron cloud shields the nuclei from B_0. The change in the shielding factor can be caused by variations in the electron density. For example, when the observed nucleus is near a strongly electronegative group, the shielding factor decreases (less shielding, de-shielding or downfield); then, the chemical shift increases. This difference makes it possible to distinguish magnetically inequivalent nuclei in a molecule. However, isochronous (i.e., the same chemical shift) will not necessarily be magnetic equivalent because protons may form different types of bonds, homotopic, enantiotopic, and diastereotopic, which determine the appearance of the spectra. The chemical shift is a measure of how far the proton signal is from the reference signal. Therefore, this determines the position of the signal on the NMR spectrum.

The chemical shift is expressed in ppm (parts per million), which is a field strength-independent unit. The ppm scale runs from the right (downfield) to the left (upfield).

$$\text{chemical shift} = \frac{\text{signal frequency} - \text{reference frequency}}{\gamma * \mathrm{B_0}} 10e6 \qquad (1.5)$$

In-vivo proton spectroscopy measures the relative frequency of the proton nucleus of a metabolite compared with the proton resonance of tetramethylsilane (TMS) at 0 ppm.

1.4 J-coupling

Magnetically non-equivalent nuclei interact via the bonding electrons. This indirect interaction is called spin-spin coupling or J-coupling (Ramsey and Purcell, 1952). J-coupling between the same species of spins is homonuclear J-coupling (e.g., proton-proton), and J-coupling between different spins is heteronuclear J-coupling (e.g., proton-phosphorous). J-coupling is the result of an internal indirect interaction of two spins via the intervening electron structure of the molecule and modifies the spectral lineshape: J-coupling splits a single peak into multiple peaks. In addition, J-coupling modulates the signal intensity by TE, acquisition sequence, and parameters.

Because the spin of a proton A has two possible orientations relative to an external field B_0, the field BX at a neighboring proton X is either slightly increased or slightly decreased, leading to a splitting of the energy levels. The energies are shifted by

$$\Delta E = \hbar J_{AX} m_A m_X \tag{1.6}$$

where m is the projection of the spin of nucleus A onto the z-axis. The line separations in the splitting patterns are measured in Hz; they are characteristic of the efficiency of the spin interaction and are referred to as coupling constants (symbol: J). The coupling constant is independent of the external B_0 field strength and has typical values of approximately 7 Hz for neighboring protons in proton spectroscopy.

A single-spin system (A) only has two energy levels: α and β, which are separated by Bohr's frequency condition $\Delta E_{\alpha\beta} = \hbar f_A$. Because only one possible energy level transition exists, the nucleus will have a single resonance at the frequency f_A (see Figure 1.3A). If we assume that there are two coupled nuclei, A and X, of the two-spin system, each of the single resonances at frequencies f_A and f_X will split into two equal peaks. However, the peak amplitudes are smaller than that of the singlet. This is referred to as a doublet (Figure 1.3B). The fundamental rule governing multiplet intensities for spin 1/2 nuclei with all identical couplings is Pascal's triangle (n = number of equivalent couplings, see Table 1.3).

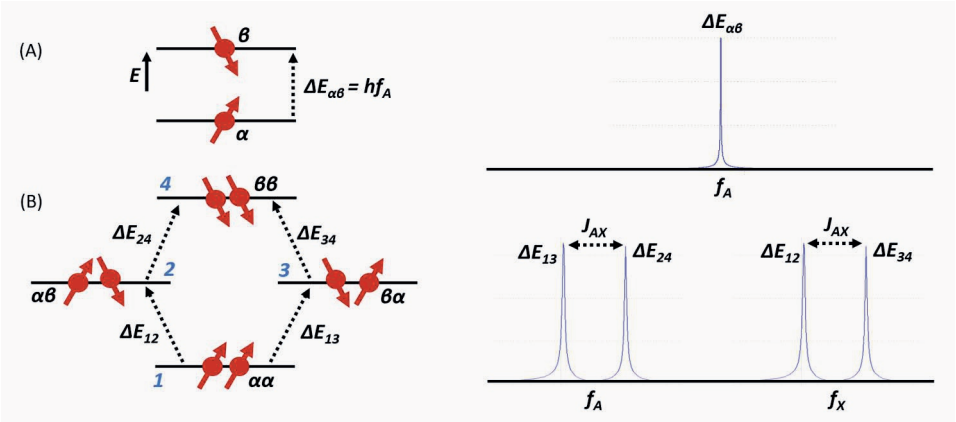

Figure 1.3. The energy level and corresponding NMR spectra for (A) uncoupled spin and (B) coupled two-spin systems. Uncoupled spin simply shows a singlet. Note that this diagram shows a simple doublet under the assumption that the chemical shift between A and X is greater than J.

Table 1.3. Pascal's triangle according to AX con igurations

n	2^n	Configuration	Name	Multiplet Intensities - Pascal's triangle
0	1	A	Singlet	1
1	2	AX	Doublet	1 1
2	4	AX_2	Triplet	1 2 1
3	8	AX_3	Quartet	1 3 3 1
4	16	AX_4	Pentet	1 4 6 4 1

CHAPTER 2.

Acquisition and Quantification

2.1 Acquisition methods

Single voxel spectroscopy (SVS) is widely used because of its robustness and the simplicity of its implementation and use. SVS acquires spectra that provide biochemical information and elucidation of molecular structure from a single target voxel that is relatively large (typically from 8 to 27 ml voxel). Therefore, this technique provides a spectrum with a high signal-to-noise ratio (SNR) in a short scan time (less than 5 min). This technique is appropriate wherever the target region is homogeneous, and its size is not too small.

In contrast with the MR imaging sequence (Figure 2.1A), the single voxel spectroscopy sequence (Figure 2.1B) does not have phase encoding steps. Instead, a localization technique is used to specify a voxel of interest (VOI).

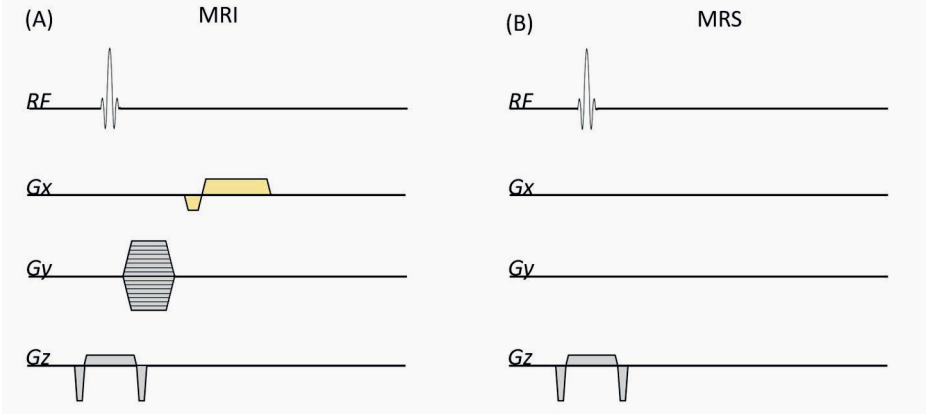

Figure 2.1. Sequence comparison between MRI (A) and MRS (B).

Three sequential B_0 field gradient pulses in three dimensions (x, y, and z) select three orthogonal slices to define a single VOI and only collect the signal from the VOI (see Figure 2.2). Because the signal intensity is proportional to the volume, a large spectroscopy volume is favorable to obtain a signal with a good SNR. However, if the voxel is too large, there is a risk of partial volume artifacts, which represents a situation that multiple brain regions or tissue types are contained in the single VOI. To minimize the partial volume effect and maximize spectral SNR, careful voxel positioning and voxel size optimization are required. The typical volume of the SVS is 8 ml.

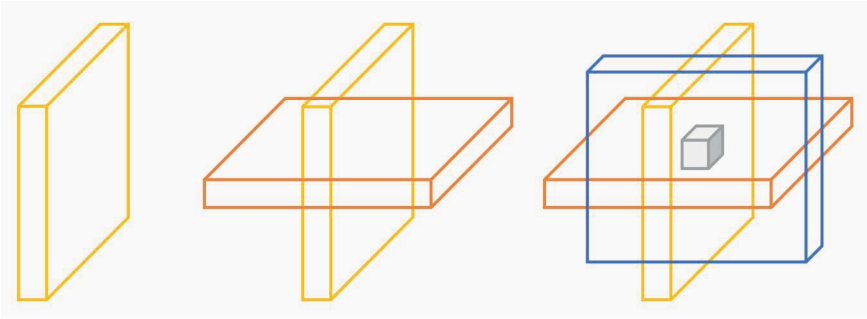

Figure 2.2. Spatial localization technique achieved by three slice-selective RF pulses that intersect the voxel of interest (gray cube), where the spectroscopy signal is collected.

2.1.1 Standard acquisition

Two fundamental acquisition techniques: PRESS (Point Resolved Spectroscopy) (Bottomley et al., 1988; Bottomley, 1984; Ordidge and Cresshull, 1986) and STEAM (Stimulated Echo Acquisition Mode) (Frahm et al., 1987; Granot, 1986; Kimmich and Hoepfel, 1987) have made this technique attractive in the spectroscopy community. Figure 2.3. shows the sequence diagrams of these two approaches.

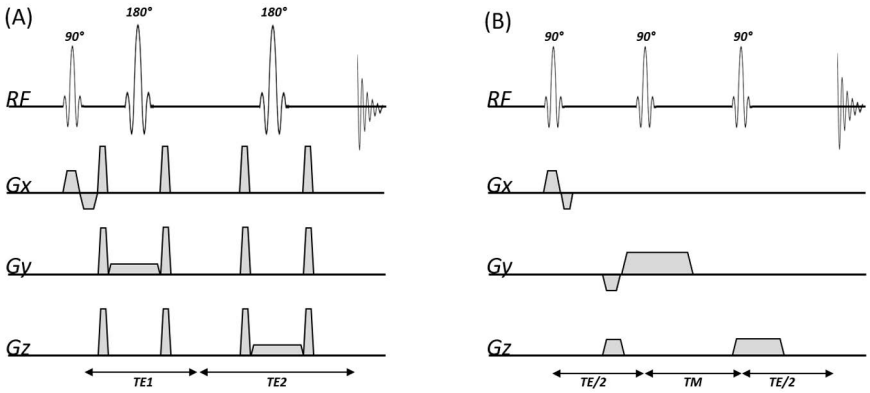

Figure 2.3. Comparison of two key acquisition sequences: PRESS (A) and STEAM (B).

PRESS (Figure 2.3A) is a dominant acquisition approach used for proton spectroscopy. This sequence is composed of two spin-echoes, in which a slice-selective excitation pulse is combined with two slice-selective refocusing pulses. Therefore, this technique is also called the double spin-echo method. In PRESS, three radio frequency (RF) pulses, with flip angles of 90° - 180° - 180°, produce a spin echo signal from the selected voxel. Conversely, STEAM uses three 90° pulses (Figure 2.3B) to collect the stimulated echo signal from the VOI. The mixing time (TM) of STEAM is the

time delay between the second and third RF pulses. During the TM, spins rotate along the magnetic field, and there is no signal decay because of T_2 relaxation. Therefore, the TM is not included in TE.

PRESS provides an SNR twice as high as STEAM if identical VOI is assumed and the same acquisition parameters, such as NEX, TE, and TR, are used because the STEAM signal is created from only half of the available equilibrium magnetization, whereas PRESS uses the full magnetization. However, STEAM shows the following advantages using only 90° pulses: In comparison with PRESS, STEAM allows the implementation with shorter TE, which leads to reducing the signal loss because of T_2 relaxation, as it uses a TM, and the 90° pulse can generally be shorter than the 180° pulse. In addition, because the 90° pulse usually has a sharper slice profile, requires less power than a 180° pulse, and shows less chemical shift displacement error (CSDE), STEAM is more favorable for ultrahigh fields (UHF) MRS (Tkáč et al., 2001).

2.1.2 Editing acquisition

Editing techniques (Mescher et al., 1998; Mescher et al., 1996; Rothman et al., 1993) are designed to discriminate J-coupled spins from noncoupled spins by exploiting the unique nuclear J-coupling properties of molecules. Spectral editing enables the observation of selective J-coupling interactions of a single coupled resonance. Using the fact that noncoupled and J-coupled spins show different responses to selective RF pulses, the difference between the selectively perturbed and nonperturbed spectra, which were individually acquired with and without the editing pulse, reveals the resonance of interest. Because metabolites that do not affect this particular perturbation show identical signals in perturbed and nonperturbed spectra; these resonances do not appear in the edited spectrum after subtraction.

Most editing sequences (Mescher et al., 1998; Mescher et al., 1996; Rothman et al., 1993) utilize the fact that the phase of J-coupled spins is modulated in an echo sequence during the echo delay. A series of spectra, acquired with and without the editing pulse, may allow the separation and identification of overlapping signals from different molecules because of their different J-modulation. Figure 2.4 demonstrates the spin evolution by refocusing pulses for AX and AX2 spin systems. For fixed TE (TE = 1/J for AX, 1/2J for AX_2), the peaks of coupled resonances are shifted by 180° in relation to those of uncoupled resonances. The second selective refocusing pulse will undo the coupled resonance phase shift without affecting the entire spectrum. If we subtract both spectra, the

uncoupled resonances with the same phase in both cases will be removed. The coupled "edited" resonances add up, because they are usually in the anti-phase, which constitutes the basic principle of spectral editing. Spectral editing can be applied to any scalar coupled spin system. GABA (Mescher et al., 1998; Mescher et al., 1996), lactate(Sotak and Freeman, 1988), glutathione(Terpstra et al., 2003), and 2-hydroxyglutarate (2HG)(Choi et al., 2012b) are widely used metabolites as an in-vivo editing target.

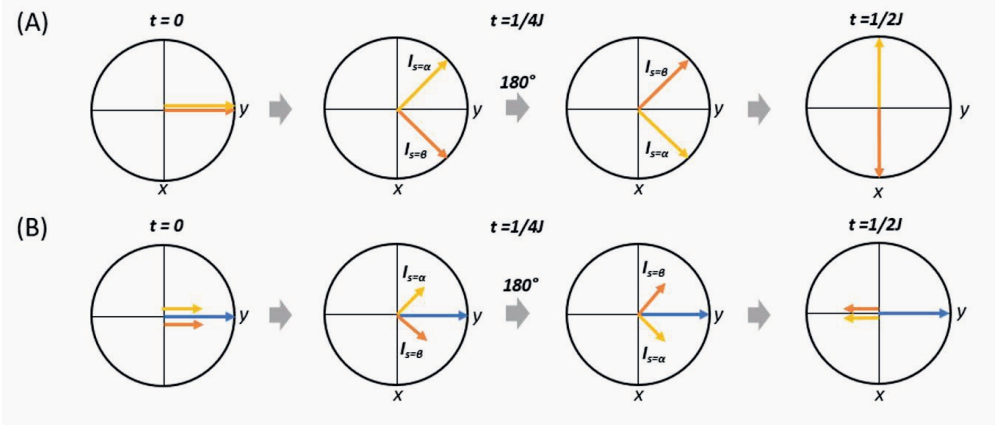

Figure 2.4 Spin evolution by a refocusing pulse after the time 1/4J for the AX (A) and AX_2 (B) systems. As the refocusing pulse simultaneously mirrors the coherences along the y-axis and inverts the spin-X populations, the echoes of the coherence will refocus with a phase shift of 180° between them. (Adapted from(Bogner et al., 2017))

2.1.3 GABA spectroscopy

γ-aminobutyric acid (GABA) is a major inhibitory neurotransmitter that is present at a concentration of approximately 1 mM in the human brain. GABA plays a vital role as a potential biomarker in neurological and neuropsychiatric disorders. GABA is composed of three methylene (CH_2) groups, which form two triplet resonances at 3.01 and 2.28 ppm, and one quintet at 1.89 ppm (Figure 2.5). Because all three resonances are overlapped by adjunct metabolites with more intense concentrations, GABA is not discriminable in the standard spectroscopy spectrum without additional quantification steps, such as spectral fitting. Hence, the spectral editing approach is commonly used to detect GABA.

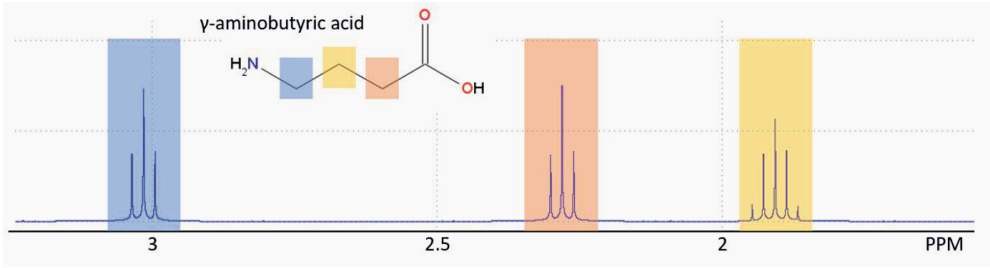

Figure 2.5 Chemical structure and simulated proton spectroscopy spectrum of γ-aminobutyric acid (GABA) at 7 T. GABA is composed of three methylene (CH_2) groups and forms three resonance peaks at 3.01, 2.28, and 1.89 ppm. The color indicates each CH_2 proton and its corresponding resonance.

J-difference editing (Rothman et al., 1993) using MEGA-PRESS (Mescher et al., 1998; Mescher et al., 1996) is a representative editing technique for detecting GABA because this technique makes it possible to directly measure the 3 ppm GABA peak. Figure 2.6A shows the sequence diagram of the MEGA-PRESS sequence. MEGA-PRESS was primarily designed to edit the GABA-$^4CH_2$ resonance at 3.01 ppm by selectively inverting the magnetization of the GABA-$^3CH_2$ protons. Two additional slice-selective pulses are located in the middle of time delays between the PRESS-refocusing pulses. Figure 2.6 shows simulated example spectra of the GABA resonance at 3 ppm for J-difference editing for MEGA-PRESS at 7 T with TE =68 ms. In principle, this technique allows the detection of the outer two peaks of the GABA triplet at 3.0 ppm because the central peak of the triplet is canceled.

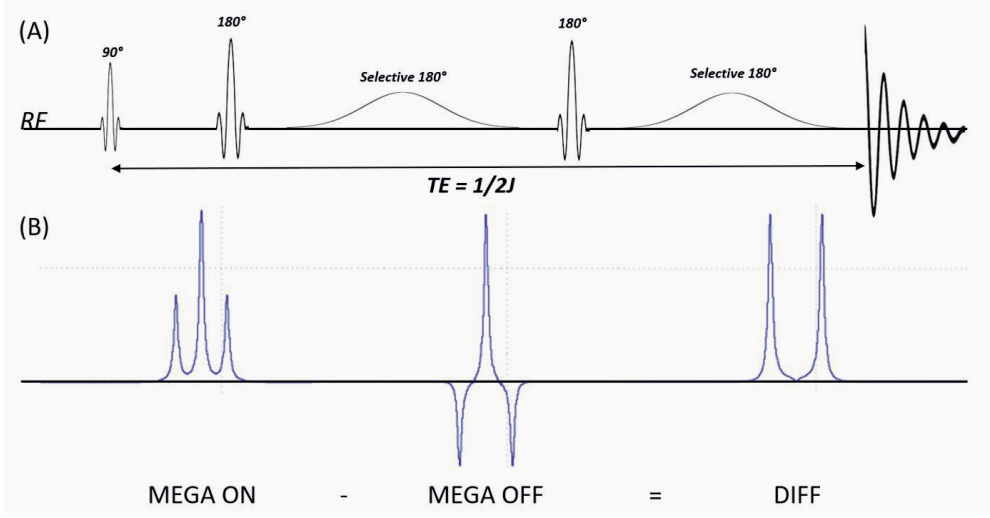

Figure 2.6 (A) Sequence diagram of MEGA-PRESS. Two additional frequency-selective RF pulses are combined with the conventional PRESS sequence. Simulated GABA-$^4CH_2$ spectra of MEGA-ON, OFF, and DIFF. MEGA-ON: Spectrum with editing pulses at 1.89 ppm, MEGA-OFF: Spectrum without editing pulses, DIFF: Difference spectrum that isolates the GABA-$^4CH_2$ resonances by subtracting the MEGA-OFF spectrum from the MEGA-ON spectrum.

2.1.4 Spectroscopy at ultrahigh field

As the static field strength increases, NMR spectroscopy yields several apparent benefits, improved SNR and increased spectral dispersion of the resonance frequencies owing to the chemical shift and simplification of J-coupling (Uğurbil et al., 2003). These result in an increased number of detectable metabolites with improved accuracy and precision. Therefore, the significance of magnetic resonance spectroscopy (MRS) continues to grow in UHFs. However, UHF MRS is accompanied by technical challenges such as B_0 and B_1 field inhomogeneities, CSDE, specific-absorption-rate (SAR) restrictions, susceptibility artifacts, shortened T_2, and prolonged T_1 relaxation times.

Improved acquisition sequences for 7 T MRS have been introduced to overcome these difficulties in comparison with the conventional acquisition methods such as STEAM and PRESS. Scheenen et al. (Scheenen et al., 2008a; Scheenen et al., 2008b) proposed a semi-localized by adiabatic selective refocusing (semi-LASER: sLASER) sequence that uses a nonadiabatic slice-selective excitation pulse and two pairs of adiabatic refocusing pulses. This sequence provides a shorter minimum TE, decreased CSDE, and lower SAR than those of the full LASER sequence, because only five RF pulses are used instead of seven. In addition to sLASER, MEGA-sLASER (Andreychenko et al., 2012), which is a combination of the conventional sLASER and two additional editing pulses, is also a conventional technique used to perform GABA editing at 7 T. These two sequences were primarily used to acquire SVS data in this work. Detailed descriptions of these acquisition sequences are provided in Chapter 3.

2.1.5 Phased-array coil

Modern magnetic resonance (MR) systems are widely equipped with a multichannel receiver array to acquire MR data efficiently. A multichannel coil is an essential piece of MR hardware that makes it possible to improve the SNR and decrease the scan time in combination with parallel imaging techniques (Griswold et al., 2002; Pruessmann et al., 1999). Because MRS does not have phase encoding steps, it is not possible to accelerate the scan speed by a factor of the coil element number with the parallel imaging technique. However, because the SVS acquires signals from a relatively small voxel, all receiver coil elements acquire the same signal. Therefore, a receiver coil with increased coil elements can acquire a signal with quality similar to the signal acquired with a decreased coil number and an increased average time. Thus, an increased number of coil elements decreases the scan time.

Figure 2.7 demonstrates the operating principle of the four-channel phased-array coil. Their corresponding weighting scores weight individually acquired spectra.

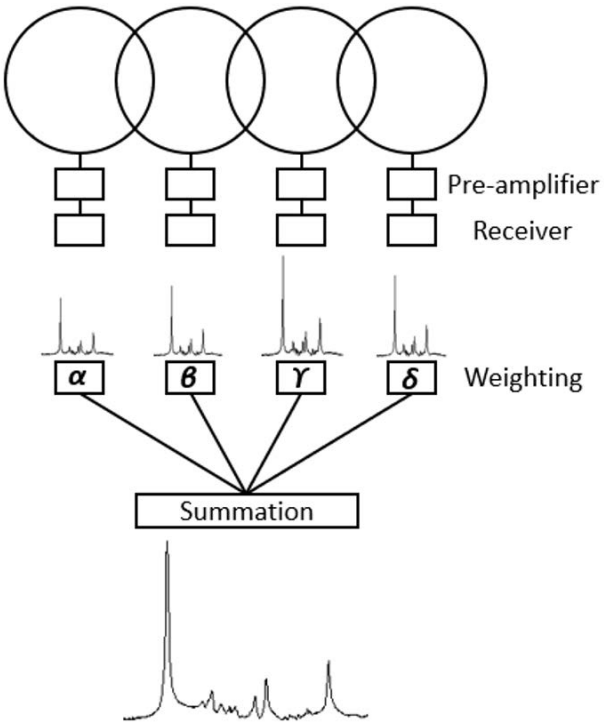

Figure 2.7 Overview of multichannel array receiver. Individually acquired signals from each coil element are combined using the combination strategy.

The combined signal *M* from *N* coil elements can be written as:

$$M(r) = \frac{\sum_{i=1}^{N_c} C_i(r) m_i(r)}{\sqrt{\sum_{i=1}^{N_c} |C_i(r)|^2}} \tag{2.1}$$

where *C* is the weighting score of each coil element. *m* represents a signal from each coil elements Hitherto, the signal combination method (Roemer et al., 1990), which combines each coil data with the coil sensitivity in the time domain, has been widely used as a default combination method by scanner manufacturers because of its simplicity and speed. However, this method requires a weakly suppressed water signal to assess the sensitivity of each coil element. More importantly, this signal weighting scheme is not optimal for the low-concentration metabolites such as GABA. Detailed optimal coil weighting strategies are described in Chapter 4.

2.2 Quantification methods

2.2.1 Brain metabolites

The fundamental goal of proton spectroscopy is to measure hydrogen-containing metabolites in human and animal tissue noninvasively. It is widely known that approximately 20–25 metabolites are detectable by proton spectroscopy in the human brain; these have been found in previous in-vivo (Kreis, 1997) and ex-vivo (Perry et al., 1971a; Perry et al., 1971b) studies. Table 2.1 summarizes typical metabolites that are detectable using proton spectroscopy in the human brain.

Table 2.1 Typical metabolites which are detectable using proton spectroscopy in the human brain

Metabolite	Formula	Chemical shift (ppm) (Govindaraju et al., 2000)	Concentration (mM/kg ww)
Alanine (Ala)	$C_3H_7NO_2$	3.775/1.467	0.3
Ascorbate (Asc)	$C_6H_8O_6$	4.449/4.002/3.743/3.716	1.4
Aspartate (Asp)	$C_4H_7NO_4$	3.891/2.801/2.653	2.1-3.1
Choline (Cho)	C5H14NO	3.185/4.054/3.501	0–0.01
Phosphorylcholine (PCh)	$C_5H_{15}NO_4P+$	3.027/3.913	0–0.95
Glycerophosphorylcholine (GPC)	$C_8H_{20}NO_6P$	3.650/3.672/3.903/3.871/3.946	0.5
Creatine (Cr)	$C_4H_9N_3O_2$	3.0270/3.9130	3.2–5.8
Phosphocreatine (PCr)	$C_4H_{10}N_3O_5P$	3.0290	2.2–4.5
γ-Aminobutyric acid (GABA)	$C_4H_9NO_2$	3.9300	1.3–2.5
Glutamine (Gln)	$C_5H_{10}N_2O_3$	3.7530/2.2190/2.1090/2.4320/2.4540	1.6–2.2
Glutamate (Glu)	$C_5H_9NO_4$	3.7433/2.0375/2.2100/2.3378/2.3520	8.9–12.8
Glutathione (GSH)	$C_{10}H_{17}N_3O_6S$	3.3769/4.5608/2.2964/2.9747/3.7690…	1.1–1.4
Glycine (Gly)	$C_2H_5NO_2$	3.5480	1.2
Glucose (Glc)	$C_6H_{12}O_6$	5.216/3.519/3.698/3.395/3.822/3.826…	1.4–2.2
Myo-Inositol (MI)	$C_6H_{12}O_6$	3.5217/4.0538/3.5217/3.6144/3/2690…	4.9–5.7
Scyllo-Inositol (Scyllo)	$C_6H_{12}O_6$	3.3400	0.3–0.4
Lactate (Lac)	$C_3H_6O_3$	4.0974/1.3242	0.5–0.7
N-Acetylaspartate (NAA)	$C_6H_9NO_5$	2.2208/4.3817/2.6727/2.4863/7.8205	11.0–13.5
N-Acetylaspartylglutamate (NAAG)	$C_{11}H_{16}N_2O_8$	4.12/2.06/1.90/2.20/2.21/7.95/4.63…	1.0–1.1
Phosphorylethanolamine (PE)	$C_2H_8NO_4P$	3.9765/3.2160	1.6–2.8
Taurine (Tau)	$C_2H_7NO_3S$	3.4206/3.2459	1.3–3.3

2.2.2 Spectral quantification

Observed in-vivo spectroscopy signals are considered to be a linear summation of each metabolite signal. Therefore, the acquired in-vivo signal *S* can be simply described as:

$$S_{in-vivo} = \sum_{k=1}^{n} C_k M_k + \varepsilon \tag{2.2}$$

where *C* is the concentration of the metabolite, *M* represents the metabolite signal, and e is a noise or error term. Because potential metabolites in the VOI are already known, spectral quantification is a procedure to estimate the concentration of each metabolite based on the spectral model *M*. The spectral model of each metabolite can be acquired by scanning the metabolite separately in a phantom (Govindaraju et al., 2000), or simulated by quantum mechanical calculations (Smith et al., 1994) based on the measured chemical shift and J-coupling from high-resolution spectra acquired at physiological values of temperature and pH. The simulation method is used because of its convenience and simplicity.

Metabolite concentrations can be estimated by spectral fitting in the time or frequency domain. Table 2.2 summarizes various established fitting methods and their main features. Because a Fourier transform is a linear operation, the two domains are equivalent. Therefore, the quantification results should be similar regardless of the domain or quantification approach. However, the acquired spectrum does not always show an ideal form because of unwanted external factors such as B_0 field inhomogeneity, eddy currents, the patient's motion, and insufficient water suppression. Therefore, the optimal selection of the analysis domain and method plays a vital role in a successful quantification outcome since each method deals with these problems by the different optimization algorithms of the acquisition and spectral preprocessing.

Table 2.2. Comparison of spectral fitting algorithms and their features.

Name	Domain	Fitting algorithm	Optimization	Baseline correction	Reference
LCModel	FD	Linear least square fitting	VARPRO	Yes	(Provencher, 1993)
AMARES	TD	Nonlinear least square fitting	Nonlinear least square solver	No	(Vanhamme et al., 1997)
QUEST	TD	Linear least square fitting	Levenberg-Marquardt	Yes	(Van der Veen et al., 1988)
AQSES	TD	Linear least square fitting	VARPRO	Yes	(Poullet et al., 2007)
MIDAS	TD	Nonlinear least square fitting	Levenberg-Marquardt	Yes	(Maudsley et al., 2006)
PROFIT	TD/FD	Linear least square fitting	VARPRO	Yes	(Schulte and Boesiger, 2006)

2.2.3 LCModel

We mainly used LCModel (Linear Combination Model) (Provencher, 1993, 2001) as the quantification tool in this study, for which this subsection provides a detailed description. LCModel is a commercial software package that analyzes MRS data in the frequency domain and is currently the most widely used software package in spectroscopy because it supports formats from all scanner manufacturers

such as Siemens, GE, Philips, and Bruker. In addition, LCModel has an almost automated software: phase, frequency, and baseline corrections are included by default. LCModel quantifies the observed in-vivo spectrum as a linear combination of in-vitro spectral models acquired from metabolite solutions or simulation under an identical in-vivo scan environment. This prior knowledge is called the "basis-set."

LCModel performs the least square fitting in the frequency domain. The measured in-vivo spectrum is compared with a linear combination of individual spectra from this basic set. The coefficient for each basis function is estimated to obtain the best fit to the in vivo spectrum. These linear combination coefficients give the maximum-likelihood estimate of the concentration of each metabolite. LCModel performs optimization steps for the lineshape and linewidth distortion by the B_0 field inhomogeneity, the frequency shifts by the magnetic susceptibility difference, phase, and baseline, along with the linear spectral coefficients. The goodness of fit is also estimated according to the Cramér–Rao lower bound (CRLB), which represents the lower limit of the statistical errors of the fitted parameters, which are determined by the SNR of the spectrum and the mutual interdependence of the model parameters (Kreis, 1997).

LCModel quantifies the absolute concentration of each metabolite in mM/kg wet weight using water scaling (Provencher, 1993, 2001,2016). The calculated absolute quantification of the metabolites C_m is

$$C_m = \frac{A_m}{A_w} \cdot \frac{Att_w}{Att_m} \cdot C_w \tag{2.3}$$

where A_m and A_w are the areas under the fitted metabolite line and water line acquired additionally without water suppression, respectively. Att_m and Att_w are corrections for the T_1 and T_2 relaxation times for water and metabolite, respectively. C_w is the known water concentration (assumed water content of 43300 mM for gray matter and 35880 mM for white matter) (Ernst et al., 1993; Kreis et al., 1993).

2.2.4 Correction factors

1. Tissue volume fraction

Each metabolite has unequal concentrations in gray matter (GM) and white matter (WM). Table 2.3 summarizes the literature values of metabolic distribution in GM and WM for normal human brain metabolites that are detectable using proton spectroscopy. Because the voxel size of SVS is relatively large, the tissue volume fraction of the VOI needs to be

considered. Because T_1 weighted images are routinely acquired to position the spectroscopy voxel, we can separate the GM, WM, and CSF volume by the image segmentation technique (Ashburner and Friston, 2005). The following equation compensates tissue volume-induced concentration variations,

$$S_{weighted}(M) = S_{measured}(M)\left(\frac{1}{f_{GM}*D_{GM}+f_{WM}*D_{WM}}\right) \quad (2.4)$$

where S(M) is the signal intensity of the metabolite, f is a volumetric fraction, and D is the metabolic distribution of the tissue.

Table 2.3 Metabolite concentration and fractional contribution in GM and WM measured by previous in-vivo and ex-vivo studies.

Metabolite	*In-vivo* proton spectroscopy							*Ex-vivo* amino acid analyzer (Perry et al., 1971a)			
	Concentration (mmol/kg, wet weight* mmol/kg, water** a.u.***)		Fraction value (%)		Brain Region	Technique	Reference	Concentration (mmol/kg, wet weight)		Fraction value (%)	
	GM	WM	GM	WM				GM	WM	GM	WM
Ala								1.3±0.22	1.1±0.20	54.17	45.83
Asp	3.8±0.6*	2.9±0.6	56.72	43.28	Cingulate & Corona Radiata	SVS	(Bank et al., 2015)	2.56±0.81	1.16±0.38	68.82	31.18
Cho	1.35±1.5*	1.58±1.1	46.08	53.92	Multiple	Multiple	(Kreis, 1997)				
	679±12***	858±15	44.18	55.82	Frontal	MRSI	(Maudsley et al., 2009)				
	1.2±0.2*	1.4±0.2	46.15	53.85	Total	MRSI	(Tal et al., 2012)				
PCh	0.2±0.2*	0.0±0.1	100	0	Centrumsemiovale & Occipital	SVS	(Hofmann et al., 2002)				
GPC	1.3±0.3*	1.9±0.3	40.62	59.38	Centrumsemiovale & Occipital	SVS	(Hofmann et al., 2002)				
PCh +GPC	1.3±0.1*	1.9±0.3*	40.62	59.38	Cingulate & Corona Radiata	SVS	(Bank et al., 2015)				
Cr	8.36±0.7*	6.27±1.0	57.14	42.86	Multiple	Multiple	(Kreis, 1997)				
	3145±42***	2936±59	51.72	48.28	Frontal	MRSI	(Maudsley et al., 2009)				
	6.7±0.6*	4.8±0.4	58.26	41.74	Total	MRSI	(Tal et al., 2012)				
	17.40±1.51**	9.05±0.93	65.81	34.09	Multiple	MRSI	(Gasparovic et al., 2009)				
GABA	2.87±0.61**	0.33±0.1	89.69	10.31	Sensorimotor	SVS	(Bhattacharyya et al., 2011)	2.32±0.34	0.26±0.12	89.92	10.08
	1.1±0.1**	0.4±0.1	73.33	26.67	Prefrontal	SVS	(Choi et al., 2006)				
	1.3±0.36**	0.16±0.16	89.04	10.96	Posterior	MRSI	(Choi et al., 2007)				
	1.00*	0.15	86.96	13.04	Occipital	SVS	(Ganji et al., 2014)				
	1.91±2.65***	1.29±2.11	59.69	40.31	Cingulate	SVS	(Geramita et al., 2011)				
	0.96±0.24**	0.44±0.16	68.57	31.43	Posterior	MRSI	(Jensen and Renshaw, 2005)				
	4.67***	3.16	59.64	40.36	Posterior	MRSI	(Zhu et al., 2011)				
Glc	1.1±0.66**	1.7±0.88	39.29	60.71	Visual	SVS	(De Graaf et al., 2001)				
Gln	3.02±0.46*	1.9±0.54	61.38	38.62	Anterior Cingulate	SVS	(Zhang and Shen, 2015)	3.75±0.25	2.56±0.38	59.43	40.57
Glu	21.44**	8.39	71.87	28.13	Total	MRSI	(Gasparovic et al., 2009)	8.64±0.83	5.54±1.01	60.93	39.07
	11.11±0.89**	8.21±0.95	57.51	42.49	Anterior Cingulate	SVS	(Zhang and Shen, 2015)				
Gly	1.1±0.1*	0.1±0.1	91.67	8.33	Frontal Cortex	SVS	(Banerjee et al., 2012)	1.80±0.55	1.44±0.39	55.56	44.44
MI	5.92±1.6*	4.85±2.1	54.97	45.03	Multiple	Multiple	(Kreis, 1997)				
	5.4±0.7*	4.6±0.7	54.00	46.00	Total	MRSI	(Tal et al., 2012)				
GSH	3.3±0.1	2.1±0.4	61.11	38.89	Multiple	MRSI	(Srinivasan et al., 2010)				
Lac	0.8±0.3*	0.9±0.3	47.06	52.94	Cingulate & Corona Radiata	SVS	(Bank et al., 2015)				
NAA	10.32±0.9*	9.86 + 0.7	51.14	48.86	Multiple	Multiple	(Kreis, 1997)				
	8.4±0.9**	8.0±0.9	51.22	48.78	Multiple	SVS	(Pouwels and Frahm, 1998)				
	4523±59***	4857±67	48.22	51.78	Frontal	MRSI	(Maudsley et al., 2009)				
	8.4±0.7*	7.6±0.5	52.50	47.50	Multiple	MRSI	(Tal et al., 2012)				
	20.96±0.84**	17.22±1.61	54.86	45.14	Multiple	MRSI	(Gasparovic et al., 2009)				
NAAG	0.9±0.5**	2.3±0.4	28.13	81.87	Multiple	SVS	(Pouwels and Frahm, 1998)				
PCr	8.1±0.5*	7.8±0.5	50.94	49.06	Cingulate & Corona Radiata	SVS	(Bank et al., 2015)				
PE								1.03±0.25	0.45±0.10	80.47	19.53
Scyllo	0.3±0.1*	0.3±0.1	50.00	50.00	Cingulate & Corona Radiata	SVS	(Bank et al., 2015)				
Ser								0.81±0.19	0.67±0.20	54.73	45.27
Tau								1.24±0.45	1.33±0.35	48.25	51.75

2. T_2 relaxation time

Two spectra acquired at different TEs show necessarily different signal intensities because of the T_2 relaxation effect. The signal intensity differences were also compensated (Edden et al., 2012a) for T_2. The TE dependence of the GABA signal relative to the signal at TE = 0 ms for the sLASER approach can be described as:

$$S(TE) = S(0)\, exp(-\frac{TE}{T2}) \tag{2.5}$$

For the GABA editing approach, we need an additional sine term because of coupling evolution, as we are measuring the side-lobes of the triplet that has a J-modulated intensity variation with TE. Then, the TE dependency of the edited GABA signal is

$$S(TE) = S(0)\, exp\left(-\frac{TE}{T2}\right) Sin^2(\pi JTE) \tag{2.6}$$

Table 2.4 summarizes T_1 and T_2 relaxation times in the GM and WM for representative brain metabolites at 7 T.

Table 2.4 T_1 and T_2 relaxation times for representative metabolites at 7 T

Metabolite	T_1 (s)	T_2 (ms)	Reference
Cho	1.24 ± 0.21	131 ± 16	(Li et al., 2012)
Cr	1.78 ± 0.23	121 ± 12	
NAA	1.73 ± 0.22	170 ± 11	
GABA	1.33 ± 0.58	63 ± 19	(Andreychenko et al., 2013; Intrapiromkul et al., 2013)

2.3 Thesis outline

Chapter 3 compares two representative GABA measurement methods, GABA-editing and non-editing acquisition in combination with the LCModel quantification. This study determines which approach is optimal for estimating GABA in terms of spectral fitting quality at 7 T. Simultaneous interleaved acquisition with our modified sequence minimizes the differential effect of extraneous factors and enables an accurate comparison of two measurements.

In **Chapters 4** and **5**, we discuss two approaches for improving spectral quantification. A multichannel phased-array coil is a widely used piece of hardware for magnetic resonance imaging (MRI) and MRS, which improves the SNR and reduces the scan time. Chapter 4 modifies existing combination methods to maximize the advantage of multichannel acquisition in terms of GABA quantification and the spectral fitting quality. Chapter 5 proposes

a new quantification approach to overcome B_0 field inhomogeneity. A good B_0 field homogeneity is an essential requirement for accomplishing the fundamental objective, which is estimating metabolite concentrations within the voxel. Because shimming is challenging at UHFs, the results of the tests of water lineshape fitting models, which are mostly independent of B_0 field homogeneity, are presented in this chapter.

Chapter 6 investigates one problem that has largely been ignored by the spectroscopy community, i.e., a potential frequency shift caused by the magnetic susceptibility differences between gray and white matter. We also demonstrate its utilization to quantify the relative metabolic distribution in gray and white matter.

Chapter 7 summarizes and discusses this work.

CHAPTER 3.

A comparison of sLASER and MEGA-sLASER using simultaneous interleaved acquisition for measuring GABA in the human brain at 7T

Abstract

γ-Aminobutyric acid (GABA), the major inhibitory neurotransmitter, is challenging to measure using proton spectroscopy due to its relatively low concentration, J-coupling and overlapping signals from other metabolites. Currently the prevalent methods for detecting GABA at ultrahigh field strengths (>= 7 T) are GABA-editing and model fitting of non-editing single voxel spectra. These two acquisition approaches have their own advantages: the GABA editing approach directly measures the GABA resonance at 3 ppm, whereas the fitting approach on the non-editing spectrum allows the detection of multiple metabolites, and has an SNR advantage over longer echo time (TE) acquisitions. This study aims to compare these approaches for estimating GABA at 7 T. We use an interleaved sequence of semi-LASER (sLASER: TE = 38 ms) and MEGA-sLASER (TE = 80 ms). This simultaneous interleaved acquisition minimizes the differential effect of extraneous factors, and enables an accurate comparison of the two acquisition methods. Spectra were acquired with an 8 ml isotropic voxel at six different brain regions: anterior-cingulate cortex, dorsolateral-prefrontal cortex, motor cortex, occipital cortex, posterior cingulate cortex, and precuneus. Spectral fitting with LCModel quantified the GABA to total Cr (tCr: creatine + phosphocreatine) concentration ratio. After correcting T_2 relaxation time variations, GABA/tCr ratios were similar between the two acquisition approaches. GABA editing showed smaller spectral fitting errors according to Cramér–Rao lower bound than the sLASER approach for all regions examined. We conclude that both acquisition methods show similar accuracy but the precision of the MEGA-editing approach is higher for GABA measurement. In addition, the 2.28 ppm GABA resonance was found to be important for estimating GABA concentration without macromolecule contamination in the GABA-edited acquisition, when utilizing spectral fitting with LCModel.

3.1 Introduction

γ-Aminobutyric acid (GABA), the major inhibitory neurotransmitter, is present at about one millimolar concentration in the human brain (McCormick, 1989). GABA plays an important role as a potential biomarker in neurological and neuropsychiatric disorders such as cancer (Bellance et al., 2012), multiple sclerosis (Cawley et al., 2015), Alzheimer's disease (Bai et al., 2015), epilepsy (Petroff et al., 1995), schizophrenia (Marsman et al., 2014), and autism (Oblak et al., 2011).

Existing *in-vivo* approaches for measuring GABA include positron emission tomography (PET) (Lingford-Hughes et al., 2002), single photon emission tomography (SPECT) (Verhoeff et al., 1999), proton magnetic resonance spectroscopy (^{1}H MRS) (Keltner et al., 1996) and chemical exchange saturation transfer (CEST) (Cai et al., 2012; Yan et al., 2016). Among these, MRS at ultrahigh filed (UHF >= 7 T) is widely used due to high sensitivity and specificity for measuring GABA (Godlewska et al., 2017a). Nevertheless, GABA MRS is still challenging by reason of its low concentration and resonances overlapping with higher concentration signals (Puts and Edden, 2012). Previously, various acquisition strategies for proton MRS have been proposed for measuring GABA, such as J-editing (Rothman et al., 1993) (e.g. MEGA-PRESS (MEsher-GArwood Point RESolved Spectroscopy) (Mescher et al., 1998; Mescher et al., 1996)) and double quantum filters (Shen et al., 2002).

The MEGA-editing method (Puts and Edden, 2012) is the most commonly used approach. A MEGA pulse is used to distinguish the GABA signal at 3 ppm from the overlapping creatine signal, based on the J difference editing approach (Mescher et al., 1998; Mescher et al., 1996). MEGA-editing combines conventional localization techniques with one or more additional frequency selective editing pulses, which invert the signal at 1.9 ppm. As the GABA resonance at 3 ppm signal is coupled to the 1.9 ppm GABA resonance, the difference between the signals obtained with and without the editing pulses should give an unambiguous GABA signal at 3 ppm. However, the MEGA-editing method also has disadvantages. It theoretically works best at certain echo times (TEs), when the GABA is refocused in anti-phase to the signal obtained without editing pulses (TE = (2n-1) / 2J, where J is 7.35 Hz, n = 1, 2, 3…). Therefore, the TE for GABA editing is largely standardized at 68 ms as the next possible TE beyond 68 ms (204 ms) would imply a significant T_2 decay of the signal. At 7 T, it is quite challenging to implement the MEGA-semi-LASER(MEGA-sLASER) sequence with TE = 68 ms due to the lack of time to insert all pulses within 68ms. Therefore, longer TEs have frequently been used (e.g., 72 ms (Chen et al., 2017) and 74 ms

Houtepen et al., 2017; Marsman et al., 2014). However, Edden, *et al*. (Edden et al., 2012b) reported that a TE of 80 ms showed a reduction in co-edited macromolecule (MM) compared to TE 68 ms even though the GABA SNR is reduced by approximately 7 % in comparison with that of TE = 68 ms due to the combined but opposing effects of increased editing efficiency and greater T_2-relaxation. In addition, motion, respiration, and frequency drift induce experimental instabilities that may result in subtraction artifacts (Harris et al., 2014).

Another extensively used GABA measurement method is to obtain a non-edited spectrum, and measure the GABA signals using spectral fitting via LCModel (Provencher, 1993, 2001). As these data are normally acquired at a shorter TE, the acquired spectrum is superior to the edited spectrum in terms of sensitivity. In addition, not only GABA but also all metabolites are quantified simultaneously. However, a spectral fitting procedure is required in order to measure metabolite concentrations. Previously, a number of studies have shown the feasibility of GABA detection in combination with LCModel analysis at different field strength: 3 T (Napolitano et al., 2013; Near et al., 2013), 4 T (Öz et al., 2006) and 7 T (Ganji et al., 2014; Wijtenburg et al., 2013). Even though GABA is detectable at various field strengths, it has also been reported that spectra that are acquired at higher field strength show superior fitting precision due to the high spectral dispersion, better SNR and simplified spectra (Pradhan et al., 2015).

Given these two leading but different GABA measurement techniques: GABA-editing and non-editing acquisitions, there have been various attempts to assess their relative merits. Terpstra, *et al* (Terpstra et al., 2005) compared STEAM (Stimulated Echo Acquisition Mode (Frahm et al., 1987; Granot, 1986; Kimmich and Hoepfel, 1987), TE = 5 ms) with MEGA-PRESS (TE = 68 ms) at 4 T in a validation study measuring glutathione (GSH). The concentrations of GSH measured with these two methods in that study were similar, suggesting a similar sensitivity of the two techniques for those conditions. Sanaie Nezhad, *et al* (Sanaei Nezhad et al., 2017) compared the accuracy and sensitivity of PRESS (Point RESolved Spectroscopy (Bottomley et al., 1988; Ordidge et al., 1986), TE = 35 ms) and MEGA-PRESS (TE = 130 ms) at 3 T to measure GSH, and found that PRESS is not an accurate and reliable method to measure GSH *in vivo*. They also showed that the spectral fitting of the PRESS spectra cannot reliably quantify the concentration of GSH when the concentration is 4 mM or less. In addition, one conference proceeding by Chen, *et al* (Chen et al., 2015) reported that the GABA to total Cr (tCr: creatine (Cr) + phosphocreatine(PCr)) ratios from occipital cortex (OC) and motor cortex (MC), measured by the MEGA-sLASER (TE = 72ms) and STEAM (TE = 17ms) approaches, are comparable after T_2 relaxation

correction. However, after MM correction, GABA editing results were superior to those of the non-editing spectral acquisitions in terms of both reliability and reproducibility. Nevertheless, the authors still suspected that MM contamination and editing efficiency might have had an influence on GABA quantification.

In addition, it is widely known that the 3 ppm signal measured with the GABA-editing technique is typically contaminated by co-edited MM due to the overlapped resonance frequencies of the GABA and MM by the editing pulse, and this is generally considered to be a methodological limitation of this approach (Behar and Ogino, 1993; Behar et al., 1994; Puts and Edden, 2012). Therefore, this measured 3 ppm signal is commonly referred to as GABA+: GABA 'plus' co-edited MM (Mescher et al., 1998).

A standard approach to obtain (relative) GABA concentrations from non-edited single voxel spectroscopy (SVS) spectra is to use LCModel (Provencher, 1993, 2001) that fits metabolites together with additional MM, and lipid baselines. Furthermore, the GABA signal is fitted to all three methylene groups of GABA, of which the resonance at 2.28 ppm is uncontaminated by the MM signal. This should ensure that the GABA estimated in this way does not include MM. We hypothesize that if the MEGA-edited spectrum also contains a visible signal at 2.28 ppm then the application of LCModel will similarly yield estimates of GABA concentration that are free of MM contamination. We can test this hypothesis by obtaining spectra from the same voxel using both acquisition techniques, to test whether the GABA concentrations obtained are the same. This study aims to compare two GABA measurement methods in combination with LCModel fitting by comparing relative GABA concentrations and corresponding spectral fitting quality at various brain regions of healthy individuals. In order to minimize the effect of external factors, a single interleaved sequence, which acquires spectra of the two measurement methods simultaneously was used. As a result, factors such as motion, shim, and B_1 inhomogeneity should be the same for both techniques.

3.2 Materials and Methods

3.2.1 Sequence implementation

The MEGA method can be implemented with conventional SVS acquisition methods. It was initially implemented in a PRESS sequence (Bottomley et al., 1988; Mescher et al., 1998; Mescher et al., 1996; Ordidge et al., 1986). However, at the ultrahigh field, PRESS loses efficiency because of B_1 filed inhomogeneity. In contrast, the sLASER

sequence (Scheenen et al., 2008a) offers improved performance mainly because of the use of adiabatic refocusing pulses that are insensitive to B_1 field inhomogeneity and have high bandwidth, leading to a small chemical shift displacement error (CSDE) (Scheenen et al., 2008b).

In this study, the sLASER sequence was used to acquire non-editing *in-vivo* spectra, and MEGA-editing was performed on the basis of the same sLASER sequence, termed MEGA-sLASER (Andreychenko et al., 2012). MEGA-sLASER and sLASER SVS spectra were acquired using a single interleaved sequence shown in Figure 3.1. It consists of the repeated application of four sub sequence blocks: a MEGA-off sLASER, a MEGA-on sLASER, and two sLASER acquisitions. The repetition time (TR) of each sub sequence block was 4500 ms.

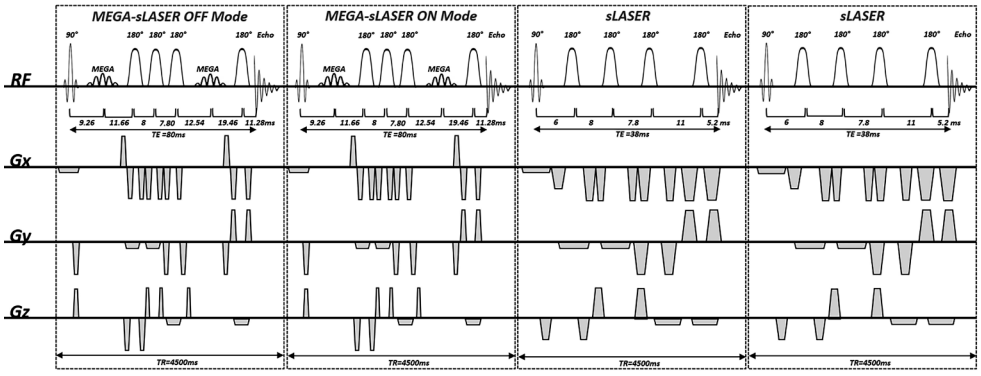

Figure 3.1. The pulse sequence diagram of the interleaved MEGA-semi-LASER (TE = 80 ms) and semi-LASER (TE = 38ms) sequence implemented in the current study. This sequence is composed of four sub-sequence blocks, which have identical TRs of 4500 ms.

In the implementation of the sLASER sequence with TE = 38 ms, a Shinnar-Le Roux (SLR) 90° excitation pulse (duration = 3.4 ms and bandwidth = 3.5 kHz) was used for slice selection in one direction and two pairs of hyperbolic secant 180° refocusing pulses (duration =5 ms and bandwidth = 5.3 kHz) were used for slice selection in the two other directions. The spoiler gradients had an amplitude of 25 mT/m and their duration varied between 0.8 and 2 ms. WET (Water suppression Enhanced through T1 effects) water suppression (Ogg et al., 1994) with four RF pulses was used to suppress the water signal. This has a lower sensitivity to B_1 variations compared with the three RF pulses WET water suppression. The water suppression block was placed before the localization block of the sequence and is not depicted in the sequence diagram. TE of 38 ms for this sequence is a slightly conservative choice to ensure elimination of unwanted signal and but comparable to those of other sLASER studies at the same field

strength; 24 ms (Terpstra et al., 2016), 25 ms (Boer et al., 2011), 28 ms (Marsman et al., 2014), 32 ms (Pradhan et al., 2015) and 36ms (Ip et al., 2017).

MEGA-sLASER was implemented with a TE of 80 ms (Edden et al., 2012b). Increased number of gradient pulses were required to have sufficient gradient performance, TE is slightly longer than the ideal value. Localization components of this sequence were the same as for the sLASER, as described above. A pair of dual-band inversion pulses (duration = 11.52 ms and bandwidth = 133 Hz) was used for both the MEGA-editing and extra water suppression. This editing pulse inverts at 1.9 and 4.7 ppm in on-mode, and at 4.7 and 7.5 ppm in off-mode. Since additional MM suppression was not included in the acquisition sequence except a prolonged TE of 80 ms, our measured GABA signal at 3 ppm is also GABA plus.

3.2.2 Ethics statement

The study was conducted at the Erwin L. Hahn Institute for Magnetic Resonance Imaging, University of Duisburg-Essen, Essen, Germany. The experimental protocol was approved by the Ethics Commission of the Medical Faculty of the University Duisburg-Essen (study number 11–4898-BO). All participants provided written informed consent in accordance with the declaration of Helsinki

3.2.3 Data acquisition

12 healthy volunteers (9 male and 3 female subjects, 29.33 ± 4.49 years old) participated in this study. Experiments were performed on a 7 T whole body system (Magnetom, Siemens, Erlangen, Germany) with a 1 Tx-birdcage/32 Rx-loops array (Nova Medical, Wilmington, MA). First, T_1 weighted images were acquired as an anatomical reference using a three-dimensional magnetization-prepared rapid gradient-echo (3D MPRAGE) (Mugler and Brookeman, 1990) with the following scan parameters: 256 slices, slice thickness = 1 mm, TR = 2500 ms, TE = 1.35 ms, inversion time (TI) = 1100 ms, flip angle = 6°, field of view = 256 x 256 x 256 mm^3, scan time ≈ 5 min. B_0 shimming was performed using FASTESTMAP (Gruetter and Tkáč, 2000). Single voxel MRS data were collected from 20 x 20 x 20 mm^3 voxels positioned at anterior cingulate cortex (AC), dorsolateral prefrontal cortex (DLPFC), MC, OC, posterior cingulate cortex (PC), and precuneus (PRC) using the interleaved MEGA-sLASER and sLASER sequence (TR = 4500 ms, TEs = 80, 80, 38 and 38 ms, 32 averages of each sub-sequence, bandwidth = 3000 Hz, data points = 1024 and total scan time ≈ 10 min).

3.2.4 Data processing

The signals from each coil element were combined by the signal weighting method (Roemer et al., 1990) that the manufacturer provides by default. MEGA difference spectra were calculated with the jMRUI software package (Version 6.0, http://www.jmrui.eu) (Naressi et al., 2001a; Naressi et al., 2001b). The nominal spectral resolution was increased to 0.27 Hz by zero filling for a more exact adjustment. The MEGA-edited spectra were acquired by subtracting MEGA-on and MEGA-off spectra after alignment with the 3ppm peak by the horizontal shift along the frequency axis, to avoid subtraction artifacts (Harris et al., 2014) caused by frequency drift. After subtraction, 1 Hz line broadening was applied to remove the zero-filling induced high-frequency noise. The same levels of zero-filling and line broadening were applied to the GABA-editing and the non-editing acquisition spectra.

3.2.5 Data analysis

Spectral quality was evaluated on the basis of the SNR and the linewidth was measured using the 2 ppm resonance of total N-acetylaspartate (NAA) and the standard deviation of the white noise area in the 7 to 9 ppm range, for both GABA-editing and non-editing acquisition spectra.

LCModel software (Version 6.3-1L, Stephen Provencher, Ontario, Canada) (Provencher, 1993, 2001) was used to estimate metabolite concentrations. The Cramér–Rao lower bound (CRLB), was taken as giving the error in the metabolite quantification (expressed in %SD) (Provencher, 1993). For the basis set for the LCModel analysis, parametric spectral models of alanine (Ala), aspartate (Asp), ascorbate (Asc), glycerophosphocholine (GPC), choline (Cho), phosphocholine (PCh), Cr, PCr, GABA, glucose (Glc), glutamine (Gln), glutamate (Glu), glycine (Gly), GSH, myo-inositol (mI), lactate (Lac), NAA, N-acetylaspartylglutamate (NAAG), phosphoethanolamine (PE), scyllo-inositol (Scyllo) and taurine (Tau) were simulated using the NMRSIM module included in TOPSPIN suite (Version 3.6, Bruker, Rheinstetten, Germany) with identical parameters (e.g. RF pulse profile, RF pulse timing, resonance frequency, and acquisition bandwidth) to those used for the in-vivo acquisition. Chemical shift and J-coupling values for each metabolite were taken from (Govind et al., 2015; Govindaraju et al., 2000).

For the sLASER data, the basis set for the LCModel analysis consisted of all twenty-one simulated metabolites. For the GABA editing method, six edited metabolites were modelled: GABA, Glu, Gln, NAA, NAAG, and GSH were included in the basis set. Each edited spectral model was created by subtracting a simulated MEGA-off spectrum from a simulated MEGA-on spectrum. As LCModel performs a phase correction during spectral fitting, additional phase correction steps were not applied

For MM and lipid signals, the non-parametric basis sets that LCModel provides by default were used (Provencher, 2016). However, one singlet peak with Lorentzian lineshape was also included in the GABA-editing basis set model the MM signal at 3 ppm, and thus avoid over-estimation of GABA due to the co-edited MM (Bhagwagar et al., 2007).

We report regional GABA concentrations as a ratio relative to tCr that was normalized across the scans. We used the tCr signal in the MEGA-off spectrum as an internal reference for the MEGA-editing approach. Previous studies used cut-off criteria of 20 % (Raschke et al., 2012) or 30% (Chowdhury et al., 2015) for CRLB, our study included all GABA and Cr results to avoid CRLB thresholding leading to a bias in measuring low concentration metabolites (Kreis, 2016). Spectral fitting quality was compared with CRLB. In addition, absolute uncertainty was calculated by multiplying the relative CRLB by the estimated concentration (Kreis, 2016).

As the data were acquired at different TEs, the signal concentration differences were also compensated (Edden et al., 2012a) for T_2. We assumed similar T_2 relaxation times in GM and WM for each metabolite, and used values taken from the literature of: $T_{2\ tCr}$ = 121 ms and $T_{2\ GABA}$ = 63 ms (Intrapiromkul et al., 2013) at 7 T. T_1 weighted images of each spectroscopy voxel of interest (VOI), which were also used for spectroscopy voxel placement, were segmented using SPM12 (Wellcome Trust Centre for Neuroimaging, University College London, UK) unified segmentation routines to determine the relative proportions of GM, WM and cerebrospinal fluid (CSF) within the spectroscopy voxel. We calculated a volume fraction for each tissue component.

Regional GABA concentrations and CRLBs were also compared with a one-way ANOVA was performed using SPSS (Ver. 22, IBM, NY). The null hypothesis was that there is no difference between regions. A p-value less than 0.05 was considered statistically significant. Bland-Altman analysis (Bland and Altman, 1986) as implemented in MedCalc Statistical

Software v18.11.6 (MedCalc Software bvba, Ostend, Belgium) was used to compare the raw GABA concentrations (determined by LCModel analysis) acquired by the two acquisition approaches over all voxels.

Potential MM contributions in the edited 3 ppm peak of the MEGA approach were also approximated by amplitude ratios between the fitted GABA line by LCModel and the acquired GABA+ peak at 3 ppm.

3.3 Results

Water linewidths obtained after performing 2 - 3 iterations with the FASTESTMAP sequence were below 14 Hz for all voxels. Figure 3.2A depicts locations of VOIs on the GM (gray) and WM (white) maps after the T_1 weighted image segmentation. Figure 3.2B shows examples of fitting GABA with LCModel using sLASER (top) and the MEGA-sLASER (bottom) for all six regions. Table 3.1 summarizes mean concentration ratios between GABA and tCr, CRLB values and absolute uncertainties for GABA and tCr at six different brain regions for the two different acquisition approaches. Measured spectral SNRs are also summarized in Table 3.1.

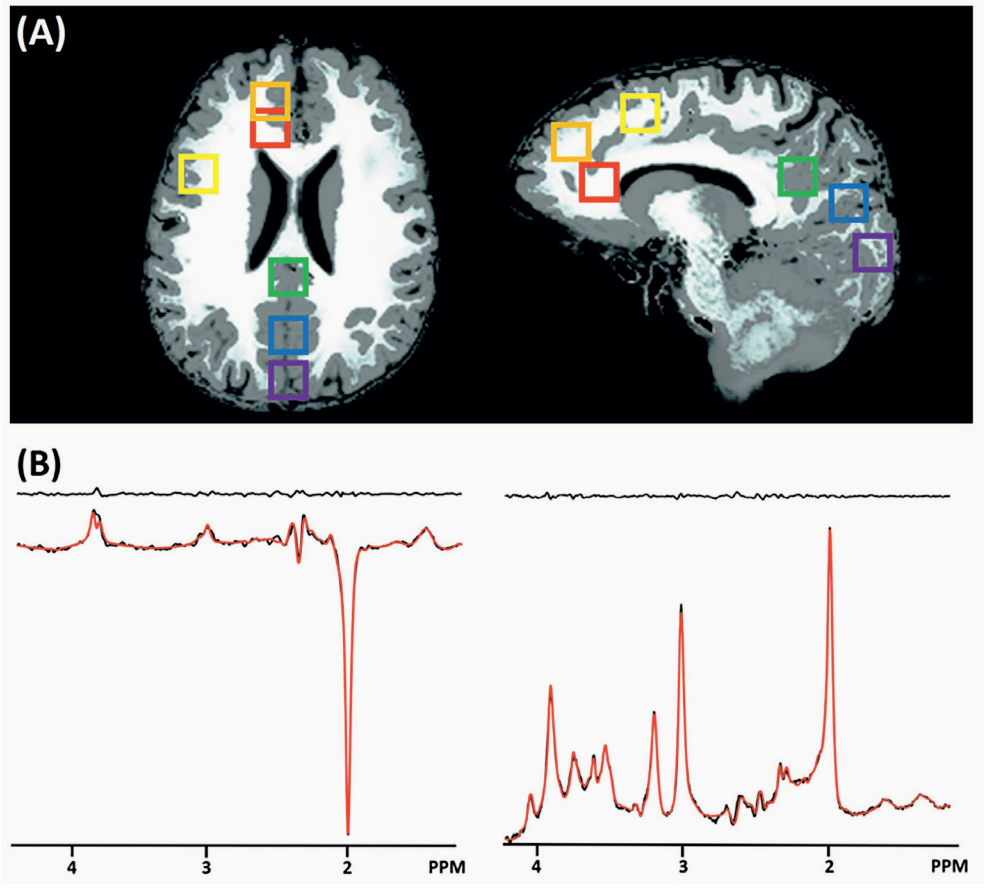

Figure 3.2. (A) Six spectroscopy voxel positions: anterior cingulate cortex (AC: red), dorsolateral prefrontal cortex (DLPFC: orange), motor cortex (MC: yellow), occipital cortex (OC: purple), posterior cingulate cortex (PC: green), and precuneus (PRC: blue). on the GM (gray) and WM (white) map. (B) Example results of the LCModel analysis for the MEGA-sLASER (left) and the sLASER (right) that were acquired with the interleaved acquisition from a single voxel at PRC. The fitted line is plotted in red and residual signal (the difference between in-vivo and fitting lines) is plotted at the top.

Table 3.1. Averaged SNR and LCModel results from six brain regions by the semi-LASER (sLASER) and the MEGA-semi-LASER (MEGA-sLASER) approaches. LCModel estimated relative GABA concentrations to total Cr (tCr) with Cramér–Rao lower bound (CRLB) for the sLASER and MEGA-sLASER. SNR was measured using the peak amplitude of the total NAA peak at 2 ppm and the standard deviation of the white noise area in the 7 to 9 ppm range These metabolic concentrations are directly measured values by LCModel before correcting for T_2-relaxation. Absolute uncertainties were calculated by multiplying the relative CRLB from the estimated concentration (Kreis, 2016). The measured value was expressed as mean ± SD

	SNR		Concentration ratio GABA/tCr		CRLB (%) GABA		CRLB (%) tCr		Absolute uncertainty ratio GABA/tCr	
Technique	sLASER	MEGA-sLASER	sLASER	MEGA-sLASER	sLASER	MEGA-sLASER	sLASER	MEGA-sLASER	sLASER	MEGA-sLASER
TE (ms)	38	80	38	80	38	80	38	80	38	80
AC	*511.80 ± 90.25*	*325.17 ± 62.40*	*0.13 ± 0.06*	*0.07 ± 0.03*	*41.20 ± 8.42*	*21.33 ± 6.60*	*1.00 ± 0.00*	*1.83 ± 0.67*	*5.17 ± 2.02*	*1.10 ± 0.94*
DLPFC	*435.37 ± 146.20*	*388.87 ± 93.90*	*0.22 ± 0.09*	*0.10 ± 0.02*	*31.33 ± 6.70*	*26.00 ± 6.68*	*1.33 ± 0.47*	*1.33 ± 0.47*	*6.25 ± 2.84*	*2.07 ± 0.68*
MC	*540.78 ± 155.41*	*294.18 ± 57.73*	*0.16 ± 0.03*	*0.11 ± 0.05*	*36.50 ± 4.11*	*19.50 ± 12.08*	*1.17 ± 0.37*	*1.17 ± 0.37*	*3.96 ± 1.50*	*1.74 ± 0.84*
OCC	*417.24 ± 37.00*	*410.63 ± 126.73*	*0.28 ± 0.03*	*0.19 ± 0.04*	*29.00 ± 7.09*	*29.33 ± 8.76*	*1.33 ± 0.47*	*1.17 ± 0.37*	*6.50 ± 3.60*	*4.81 ± 0.74*
PC	*441.11 ± 102.62*	*277.74 ± 78.50*	*0.26 ± 0.09*	*0.18 ± 0.04*	*31.83 ± 4.30*	*28.50±11.72*	*1.17 ± 0.37*	*1.33 ± 0.47*	*8.75 ± 2.14*	*3.70 ± 0.84*
PRC	*487.66 ± 143.81*	*314.86 ± 102.78*	*0.25 ± 0.05*	*0.18 ± 0.03*	*31.00 ± 6.58*	*27.50 ± 5.19*	*1.17 ± 0.37*	*1.17 ± 0.37*	*7.62 ± 3.59*	*4.27 ± 0.94*

Figure 3.3. shows the correlation between GABA/tCr and GM volume fraction in the spectroscopy voxel estimated with the two different acquisitions after T_2 correction between sLASER (TE = 38 ms) and MEGA-sLASER (TE = 80 ms). We found a linear correlation between the GABA/tCr concentration ratio and GM tissue distribution (linear regression line: $y_{TE=38\ sLASER} = 29.27x + 4.68$ and $y_{TE=80\ MEGA-sLASER} = 33.18x + 2.54$, %). In addition, these regression lines were almost identical for the two methods. This result shows a large dependence of measured GABA concentration on GM volume fraction, independent of the two acquisition methods. On the assumption that CSF does not contain significant quantities of metabolites (Joanna et al., 1993), estimated percentage GABA distributions in the GM and WM using the linear regression lines were (GM%: WM%) 86%: 14% for sLASER and 93%: 7% for MEGA-sLASER, very much in line with the literature values for the relative distribution between GM and WM (Bhattacharyya et al., 2011)

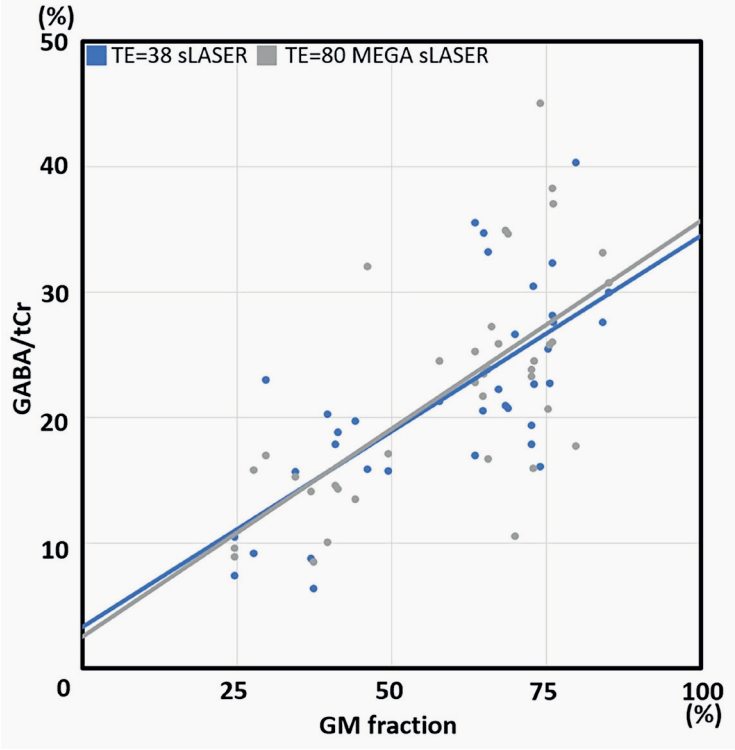

Figure 3.3. Correlation between GABA/tCr and GM volume fraction in the spectroscopy voxel measured by two different approaches (blue: TE = 38 sLASER, gray: TE = 80 MEGA-sLASER) across all examined voxels after the T_2 correction. GABA concentration was in directly proportional to the GM tissue fraction. The linear regression lines of these two methods are almost identical. Equations of the linear regression lines were $y_{TE=80\ MEGA-sLASER} = 33.18x + 2.54$,and $y_{TE=38\ sLASER} = 29.27x + 4.68$,unit(%)

We also found similar GABA to tCr ratios acquired with the two methods for each voxel (Figure 3.4A). Error bars indicate 95 % confidence intervals. Regional GABA concentrations showed statistically significant differences between group means as determined by a one-way ANOVA ($F(5,36) = 0.302$, $p = 0.019$) for the sLASER method, and ($F(5,36) = 6.015$, $p < 0.001$) for the GABA editing method. OC, PC, and PRC showed similarly high mean GABA/tCr ratios as compared with the other three regions: AC, DLPFC, and MC.

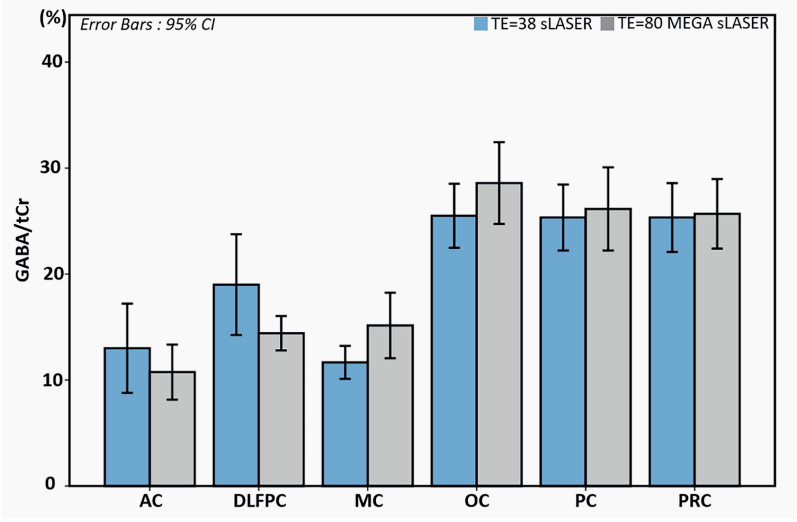

Figure 3.4. GABA/tCr comparisons after considering both the GM and WM volume weighting and the T_2 relaxation times of GABA and NAA. T_2 correction factor for TE=80 MEGA-sLASER was 1.488 or GABA/tCr. Ater applying this actor, we ound no statistically significant difference in GABA/tCr ratio between the two methods. P-values were above 0.05 for all regions. Error bars indicate 95% confidence intervals.

Figure 3.5 shows CRLB comparisons of GABA (A) and tCr (B), estimated by the two different acquisition strategies. For both metabolites, the MEGA-editing approach showed slightly better spectral fitting quality than that of the non-editing acquisition approach according to CRLB for all regions examined. Error bars also indicate 95% confidence intervals.

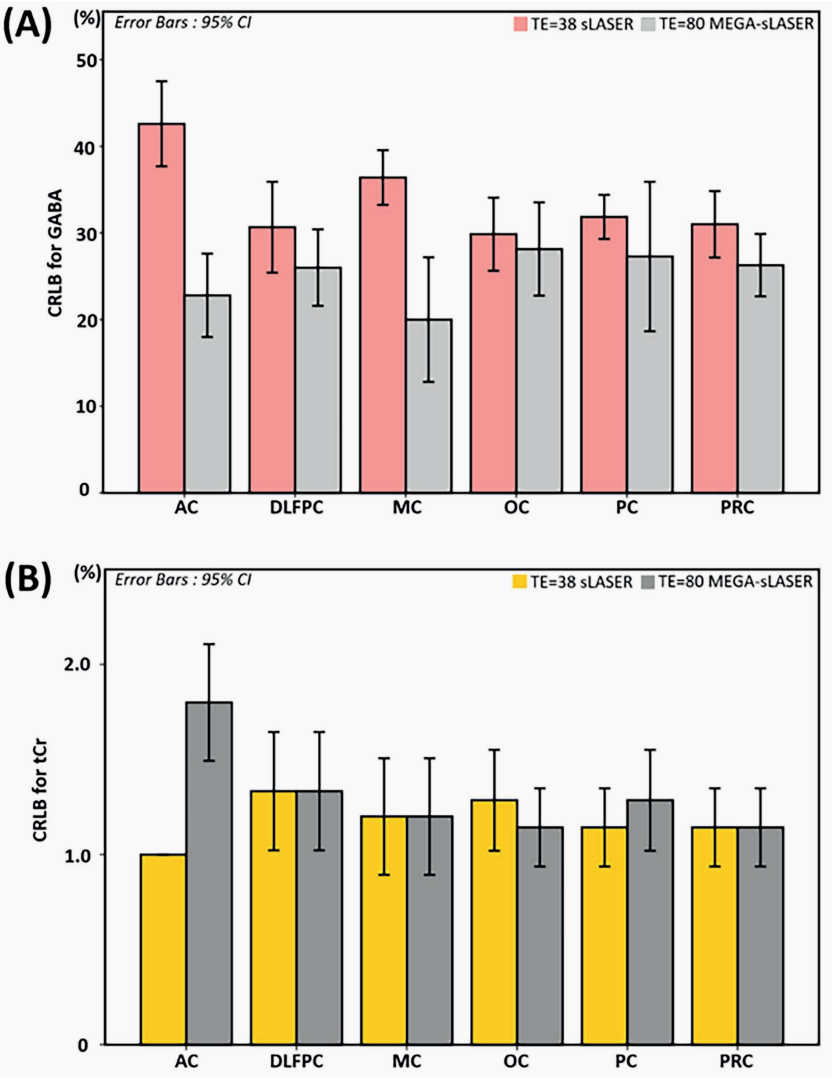

Figure 3.5. CRLB comparison of (a) GABA and (b) tCr between sLASER and MEGA-sLASER for the six brain regions examined. Error bars indicate 95% confidence intervals, in accordance with table 3.1.

The Bland-Altman plot in Figure 3.6 shows the mean bias ± SD with 95 % confidence intervals between the sLASER and MEGA-sLASER results as 0.06 ± 0.73 (blue line), and the limits of agreement were −1.36 and 1.50 (brown lines).

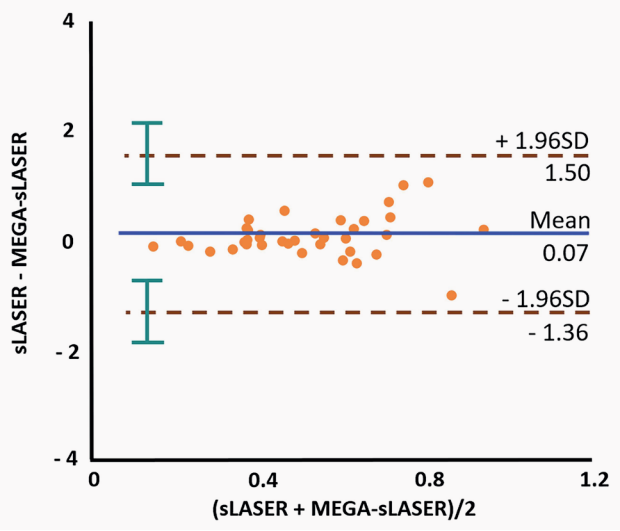

*Figure 3.6 Bland-Altman plot of the GABA concentration from the interleaved measurements using the semi-LASER and MEGA-semi-LASER approaches afterthe LCModel analysis. The blue horizontal line shows a mean value and two brown lines show ± 1.96 * SD with 95 % confidence intervals (green) across all measurements.*

One example of the GABA edited spectrum (gray) with metabolite fitting lines: GABA (red), NAAG (green), NAA (purple), Gln (yellow) and Glu (blue), which were estimated from LCModel is shown in Figure 3.7. GABA estimation is clearly determined by the fit to the 2.28 ppm peak. Pure GABA accounts for 47.21 ± 17.04 percent of the total 3 ppm signal, calculated as the ratio of the LCModel GABA fitted line at 3 ppm to the total measured 3 ppm peak averaged over all subjects.

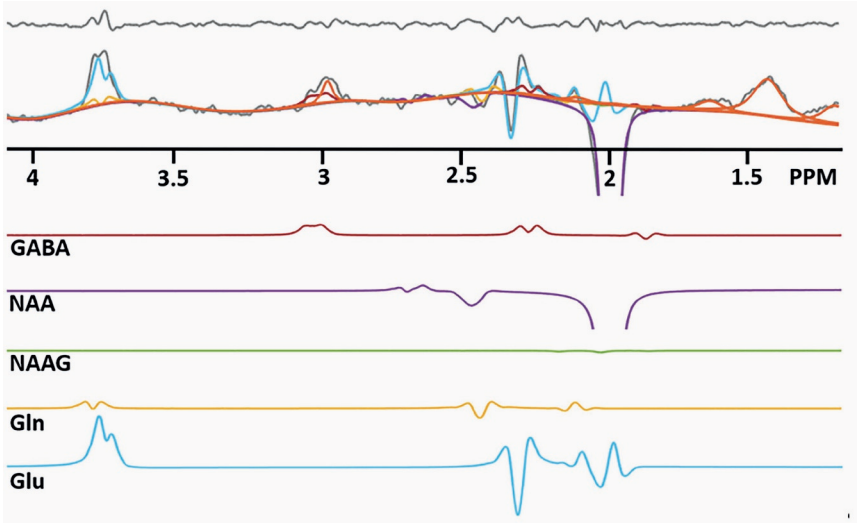

Figure 3.7. one example o GABA edited spectrum (gray) with metabolite fitting lines: GABA (red), NAAG (green), NAA (purple), Gln (yellow), Glu (blue), Glu (blue) and MM (orange), which were estimated from LCModel. The top panel indicates residual, which is a difference between in-vivo and fitting lines. Directly observable GABA-$^2CH_2$ resonance at 2.28 ppm plays an important role in the GABA quantification with spectral fitting. GABA estimation is limited by the 2.28 peak, which is the true GABA. It prevents over-estimating GABA by co-edited macromolecule. Note that the bottom part of the NAA signal is truncated in this figure

3.4 Discussion

The interleaved sequence, which we implemented in this study, provides simultaneous MEGA-editing and non-editing acquisitions in a single sequence. By acquiring concurrently, the interleaved acquisition balances any instability across the two techniques. Therefore, we could avoid potential problems of registration, motion, B_1-inhomogeneity or different shim quality that may have occurred if we would have acquired sequentially. It is widely known that the adiabatic RF pulse based sLASER sequence has the advantage of the less level of CSDE in comparison to the PRESS sequence at the ultrahigh field (Scheenen et al., 2008a) owing to the use of adiabatic refocusing pulses. The sequence used in this study had a maximum CSDE of 8.4% (Rohani Rankouhi et al., 2018).

After applying the T_2 correction factor, which compensates the different TEs, the GABA/tCr ratios for the two acquisition techniques did not differ significantly. From the fact almost all difference values are within the confidence limits, and the p-value is greater than 0.05, we conclude that there was no significant difference between the GABA acquisition methods (see Figure 3.6).

In addition, the uniform distribution of difference values shows that there is no systematic bias between the two methods (calculated bias = 0.01). Judging from the results of the linear regression lines (see Figure 3.3) and the Bland-Altman analysis (see Figure 3. 6), the two different approaches showed similar consistency in terms of the GABA estimation across the brain regions in combination with proper compensation steps.

3.4.1 Regional GABA Concentration

Even though the main purpose of this study was to compare the two methodological approaches in combination with LCModel analysis, we were also able to compare GABA concentrations across different brain regions. As we mentioned in the Introduction, it is widely known that GABA is mostly concentrated in GM (approximately 90% in GM and 10% in WM). Not only spectroscopy studies (Bhattacharyya et al., 2011; Choi et al., 2006; Ganji et al., 2014) but also an *ex-vivo* study (Perry et al., 1971a) obtained similar GABA distribution ratios between GM and WM. Chen, *et al* (Chen et al., 2016) reported that GABA concentration linearly increased with GM volume fraction for one of the brain regions we also studied (AC). In our result, as we can see in Figure 3.3, GABA concentrations were largely driven by the GM tissue fraction. In addition, estimated GABA distribution ratios in the GM and WM by the linear regression lines are in close agreement with the literature value. This result confirms that GABA is heavily concentrated in GM, and highlights the importance of the tissue volume correction for GABA quantification (Mikkelsen et al., 2016a).

In addition to the current study, other studies, which investigated regional GABA concentration differences while accounting for tissue volume variations, found differences in the regional GABA level. However, there is some inconsistency in the literature. For instance, Ganji, *et al* (Ganji et al., 2014) reported higher concentrations of GABA in the frontal lobe than in the OC at using PRESS (TE = 92 ms) at 7 T. Öngür, *et al* (Öngür et al., 2010) found higher GABA/Cr ratio in a frontal region (AC) than in an occipital region (parieto-occipital cortex) measured with the MEGA-editing method at 4 T. On the other hand, Bhagwagar, *et al* (Bhagwagar et al., 2008) found higher GABA/Cr ratio measured with MEGA-editing in the occipital region (OC) than that in AC. Durst, *et al* (Durst et al., 2015) also reported higher GABA in OC than in frontal lobe using 3 T MEGA-PRESS. Van der Veen, *et al* (Veen and Shen, 2013) similarly found higher GABA concentration in the OC than that of the

the anterior area (c. f., MPFC) with the MEGA-editing method comparing two voxels in frontal and occipital lobes. Van der Veen, et al (Veen and Shen, 2013) selected voxels that had the same GM and WM tissue volume to exclude tissue volume effects. They proposed therefore that the difference should be attributed to factors other than GM volume. The trend in our data is in accordance with that of the latter studies (Bhagwagar et al., 2008; Durst et al., 2015; Veen and Shen, 2013).

Recent molecular Imaging studies, which quantified $GABA_A$ receptor using positron emission tomography (PET) with ^{11}C flumazenil (D'Hulst et al., 2015; Richardson et al., 1996), and single-photon emission computed tomography (SPECT) with ^{123}I-iomazenil (Nagamitsu et al., 2016) have visualized $GABA_A$ receptor densities in the human brain. These reports have shown not only that the $GABA_A$ receptor is more heavily concentrated in GM, but also its density in posterior brain areas is higher than that of anterior areas. This supports our finding that GABA concentration in posterior regions such as OC, PC, and PRC showed higher GABA levels than those of anterior regions: AC, DLPFC, and MC.

3.4.2 MM contamination

We found no statistically significant difference for the quantified GABA concentrations with LCModel between two acquisition techniques. Our finding could potentially be explained by one of two possibilities: The LCModel fitting result of the non-editing spectrum also contains MM contamination, or LCModel efficiently quantifies the GABA signal from the GABA edited spectrum without the interference of the co-edited MM.

LCModel estimates MM and lipid signals at each fixed chemical shift location with non-parametric spectral models including a smoothing B-spline as a baseline (Provencher, 1993). Because these MM and lipid signals are not only measured values but also part of the formulaic model, these quantification approaches still risk over-, or under-estimating metabolic concentrations in the co-edited signal. It is quite challenging to determine from our LCModel quantification results of sLASER whether the estimation of GABA is contaminated by MM. However, we can assume the presence of MM contamination in the MEGA-sLASER spectra. In contrast to MM and lipid signals, metabolic signal quantification uses parametric spectral models, which are included in a basis set. LCModel finds metabolic concentrations by changing the amplitudes of simulated metabolic models with their lineshapes unchanged. Therefore, all resonances of GABA also play an important role in solving the optimization problem.

In our spectral fitting results, we found that the directly discernible 2.28ppm GABA signal was essential for distinguishing the GABA signal from GABA+ (see Figure 3.7). GABA estimation was largely determined by the size of GABA-$^2CH_2$ resonance at 2.28 ppm. Because the 2.28 ppm region is not related to the co-edited MM, the visible GABA resonance at 2.28 ppm represents an uncontaminated GABA signal. This result suggests that GABA quantification with spectral fitting is able to separate pure GABA from GABA+ provided that the 2.28 ppm GABA resonance is also recorded. Previous studies by Ganji, *et al* (Ganji et al., 2014) and Choi, *et al* (Choi et al., 2012a) also highlighted the significance of this GABA-$^2CH_2$ resonance in terms of the spectral fitting procedure.

LCModel provides a GABA-editing exclusive control file called 'mega-press-3' (Provencher, 2016). This setting excludes quantification of the baseline and MM signals assuming baseline and MM signals are identical between MEGA-on and -off spectra, and that they hence cancel in the subtraction. Since this setting mainly attempts to estimate the 3 ppm peak as GABA+, this necessarily overestimates the GABA concentration as co-edited MM will not be eliminated. Therefore, we did not use this approach.

We corrected for T_2 relaxation using the T2-value of 63 ms taken from the study by Intrapiromkul, *et al* (Intrapiromkul et al., 2013). After correction the values obtained were similar between the two methods (see Figure 3.3 and Figure 3.4A). This consistency strongly supports the correctness of the T2-value used, and also that the analyses have yielded results without MM contamination. Our estimate that MM constitutes approximately 53% of the signal at 3 ppm is at the upper limit of, but not inconsistent with previous literature values 44% (Rothman et al., 1993), 41 - 49% (Shungu et al., 2016), and 52-57% (Mikkelsen et al., 2016b)

3.4.3 Spectral fitting quality

Since the thresholded CRLB estimation may cause a bias (Kreis, 2016), we included all GABA and tCr results. We also compared absolute uncertainties for the GABA estimation for both acquisition methods. As a result, we found that CRLBs and absolute uncertainties of estimated GABA for the MEGA-editing method are lower than those for non-editing acquisition method for all six regions (see Table 3.1 and Figure 3.5A).

Compared with the non-editing acquisition, the GABA editing method provides a much simpler spectral pattern with only six metabolic signals present, that are relatively well separated. This explains why the spectral fitting precision of the MEGA-editing results for estimating GABA is superior to that of the sLASER result, despite the editing method eliminating also a number of lines from the GABA spectrum. MEGA-sLASER and sLASER showed similar CRLB values for tCr (Figure 3.5B) which is unsurprising given that the tCr concentration of the MEGA-sLASER was estimated from the MEGA-off spectra using a non-editing acquisition. The reasonably good CRLB values of tCr for both approaches confirm that spectral quality and spectral fitting quality with LCModel were good enough for accurate quantification.

3.5 Conclusion

This study compared GABA concentration for six different brain regions with the non-editing spectral acquisition approach and the GABA editing approach using a single interleaved sequence acquisition. The simultaneous acquisition of sLASER and MEGA-sLASER minimized differences in confounds which could have occurred in individual acquisitions. Our finding confirms that GABA is heavily concentrated in GM. Therefore, regional GM volume is an important contributor to measured GABA concentration variation. In addition, the ability to reliably measure the GABA resonance at 2.28 ppm would appear to lead to accurate estimates of GABA concentration without MM contamination. A similar concentration of GABA signal measured with the two methods for each voxel was obtained after correction for T_2, showing that the two acquisition strategies are both reliable and have a similar accuracy to measure GABA. However, The GABA-editing approach was superior in terms of precision, as assessed by lower CRLB values.

CHAPTER 4.

Optimal phased-array signal combination strategies from separate coil elements for GABA spectroscopy at 7T

Abstract

The use of phased array coils for signal reception can increase the signal to noise ratio (SNR) of single voxel spectroscopy. To take full advantage of the phase arrayed coil, an optimal signal combination strategy is required. This is especially important for detecting low concentration metabolites such as gamma-aminobutyric acid (GABA). In this study, we modified coil combination methods by excluding the contribution from coils with low signal in order to maximize SNR. Two representative GABA acquisition methods: the non-editing and GABA editing approaches, were used to acquire single voxel spectroscopy data from twenty healthy volunteers using a 32-channel phased array receiver coil at 7 T. When the number of channels was reduced and an optimized coil weighting method used, we found a reduction in ghost artifact level, and an improved SNR in comparison with the conventional coil combination method.

4.1 Introduction

The phased-array receiver coil is standard equipment in the modern magnetic resonance scanner, as it can both be used to increase the signal to noise ratio and decrease scan time (Hardy et al., 1992; Roemer et al., 1990). To take maximum advantage of a phase arrayed coil, an optimal signal combination strategy is required. Since the signal weighting method was proposed with 4 channels (Roemer et al., 1990), various signal combination schemes have been proposed for proton spectroscopy, which combine separate signals from each coil element in the time domain (Brown, 2004; Erdogmus et al., 2004; Roemer et al., 1990), or the frequency domain (Hall et al., 2014; Wald et al., 1995). Among these, the signal weighting method (Brown, 2004) is now widely accepted as a default method of the commercial MR scanner due to its speed and simplicity (Rodgers and Robson, 2016). However, because this method uses signal intensities as assessed by the dominant signals (e.g., N-acetylaspartate (NAA), or weakly suppressed water signal) as weighting scores, it is not necessarily optimal for low SNR metabolites such as gamma-aminobutyric acid (GABA) where sensitivity is a primary concern.

In comparison with imaging, single voxel spectroscopy acquires the signal from a relatively small voxel. Therefore, all channel elements do not contribute equally. Especially, in the situation that the voxel is located at the periphery, high sensitivity signal is only recorded at a limited number of coils, that are positioned close to the voxel, whereas remote coil elements detect signals with a low SNR level. More remote coils may only add noise to the spectrum. Therefore, in this study, we extended previously proposed coil combination strategies (Brown, 2004; Erdogmus et al., 2004; Hall et al., 2014; Roemer et al., 1990; Wald et al., 1995) in order to maximize SNR by excluding low SNR data.

We compared the use of an optimal number of coils with the conventional approaches, which use all coil data, for two representative GABA measurement techniques: GABA editing using MEGA (Mescher et al., 1998; Mescher et al., 1996; Rothman et al., 1993) and a non-editing acquisition where spectral fitting is used to assess the GABA concentration.

Since GABA quantification requires spectral fitting steps in the time (Poullet et al., 2007) or frequency (Provencher, 1993) domains in order to resolve GABA accurately from overlapped signal (e.g., creatine (Cr), glutamate (Glu) and co-edited macromolecule (MM)), spectral fitting quality should also be taken into account in evaluating the optimal coil

combination strategy for GABA. Therefore, we also evaluated coil weighting methods on the basis of the spectral fitting precision as well as the SNR improvement and investigate which signal combination method is optimal in terms of GABA quantification using LCModel fitting (Provencher, 1993, 2001).

4.2 Materials and Methods

4.2.1 Data Acquisition

A 7 T whole body system (Magnetom, Siemens, Erlangen) equipped with a 1 Tx-birdcage/32 Rx-loops array (Nova medical, Wilmington, MA) was used for MRI and MRS acquisitions. First, T_1 weighted images with a three dimensional MPRAGE (Magnetization Prepared Rapid Acquisition Gradient Echo) sequence were collected for voxel positioning with the following parameters; matrix size = 256 * 256 * 256, 1 ml isotropic voxel without slice spacing, flip angle (FA) = 6°, repetition time (TR) = 2300 ms, echo time (TE)= 1.35 ms, and inversion time (TI) = 1100 ms.

FASTESTMAP (Gruetter and Tkáč, 2000) was used to shim the spectroscopy voxel before the spectral acquisition. MEGA-sLASER (Andreychenko et al., 2012) and sLASER (Scheenen et al., 2008a; Scheenen et al., 2008b) sequences were employed to acquire single voxel spectroscopy data from 8 ml isotropic voxels at occipital cortex of 20 healthy volunteers (11 males and 9 female subjects; 27.2± 7.23 years old) with following parameters: MEGA-sLASER: TE = 80 ms, TR = 4500 ms and number of averages = 64, and sLASER: TE = 38 ms TR = 4500 ms and number of averages = 64. Weak water suppression was used for both acquisition approaches.

4.2.2 Combination strategies

Combination methods make a weighted linear sum of multiple signals. In order to align spectra, a phase correction step was performed to maximize the SNR (Brown, 2004). Combined signal $S(t)$ from individual signal $s_n(t)$ of the n-channel receiver coil after phase correction can be written as:

$$s(t) = A * \ exp[(-i\omega - 1/T2)t + i\Phi] \tag{4.1}$$

$$S(t) = \sum w_n s_n(t) e^{i\Phi} \ / \sqrt{\sum (w_n)^2} \tag{4.2}$$

where A is signal amplitude; ω the angular frequency; Φ the phase; w a weighting vector and *n* the coil number. Various methods for obtaining the values of *w* will be described below. All signal combination steps were processed using custom written scripts in Matlab (version. 2016b,

Mathwork, Natick, MA). We used a measurement history file, called TWIX in the Siemens system, which stores raw data from each coil element. First, we performed the 0th order phase correction to align all spectra individually over the iteration and channel in the time domain, and then combined the signals using the strategies described below. The following description describes the coil combination schemes used in this study.

1. *Signal weighting method*

The signal weighting method (Hardy et al., 1992; Roemer et al., 1990) is the most commonly used approach due to its simplicity and accuracy. Subsequently, Brown (Brown, 2004) proposed another signal weighting algorithm, that uses the conjugate value of the first time point of the time domain signal since the first time-domain point represents both the phase angle and the coil sensitivity. This method which we employ, performs the phase correction and the weighting simultaneously by multiplying the conjugate number as a weighting score with the time domain signal. The combined signal S(t) from the individual signal $s_n(t)$ by the signal weighting combination step can be written as:

$$S(t) = \sum \bar{s}_n(1)\, s_n(t) / \sqrt{\sum \bar{s}_n(1)\, s_n(t))} \quad (4.3)$$

where, $\bar{s}_n(1)$ denotes a conjugate value of the first time point from nth coil data.

2. *Signal to noise (SNR) weighting and signal to noise squared (SN^{2}R) weighting methods*

This SNR weighting method uses the SNR of a certain peak (e.g. NAA or residual water), in the frequency domain signal as a weighting coefficient (Deelchand et al., 2010; Wald et al., 1995) to compensate noise variations between channel elements on the assumption that the noise of each coil element is not correlated. Spectra are combined with the weighted sum by the Eq. 4.2. Hall, et al (Hall et al., 2014) latterly proposed the SN^{2}R combination method. They showed the SN^{2}R weighting method slightly improved the spectral SNR in comparison with the SNR weighting method. For the SNR weighting, the SNR of the targeted peak in the frequency domain provides the weighting coefficient. For the editing approach, SNR of the 3 ppm peak, which is widely referred to as GABA plus (GABA+) due to the co-edited MM (Mescher et al., 1998; Mullins et al., 2014), was used as the target peak in the GABA edited spectrum.

As GABA is not discernible in the non-editing acquisition spectrum, the SNR of GABA could not be used to give the weighting coefficient. Instead, the SNR of the 3 ppm peak, which 67is composed of total Cr (tCr: Cr + phosphocreatine (PCr)) and GABA was used. The SNR was calculated as the ratio of the peak amplitude to the standard deviation of the white noise area in the range 7 – 9 ppm. For the SN2R method, the same approach was used as the SNR weighting method except for the fact that the weighting coefficient is the SN^2R of the targeted peak.

3. Singular value decomposition (SVD) method

The SVD method (Erdogmus et al., 2004) separates the metabolite signal from noise on the assumption that the first singular value is an ideal spectrum without noise, and noise is uncorrelated between channels. The principal signal component was extracted from noise by the noise covariance matrix, which follows a multivariate normal distribution. The SVD of the noise decorrelated signal S (assuming the m*n matrix, where m: channel number and n: spectral resolution) is the factorization:

$$S = U\Sigma V^T \tag{4.4}$$

in which, U is an m*m unitary eigenvector matrix of noise covariance, Σ is an m*n diagonal matrix, and V^T is an n*n unitary matrix, and the conjugate transpose of V. After SVD, the first principal column of V^T is considered as an optimally combined signal. The noise covariance matrix was computed by white noise in the range from 2200 to 2500 Hz in time domain signal.

4.2.3 Coil combination with the reduced number of channels

In this study, we modified the above mentioned coil combination methods to only use the most sensitive coil data. For the signal weighting method, we sorted all coil data by the magnitude of the first data point in descending order and iterated the weighting step until the combined signal reached the maximum SNR. For the SNR and SN^2R weightings, we sorted all coil data by the SNR of the 3ppm peak. For SVD, we also iterated SVD steps from the highest magnitude coil in the same way.

4.2.4 Quantification and Evaluation

LCModel (ver. 6.3-1L, Stephen Provencher Inc, Oakville, Ontario, Canada) was used to quantify metabolite concentration and the Cramér-Rao lower bound (CRLB) as an estimate of the goodness of fit. The basis-set for

LCModel quantification includes 20 metabolites: aspartate (Asp), ascorbate (Asc), glycerophosphocholine (GPC), choline (Cho), phosphocholine (PCh), Cr, PCr, GABA, glucose (Glc), glutamine (Gln), Glu, glycine (Gly), glutathione (GSH), myo-inositol (mI), lactate (Lac), NAA, N-acetyl aspartyl glutamate (NAAG), phosphoethanolamine (PE), scyllo-inositol (Scyllo) and taurine (Tau) for analyzing the sLASER acquisition, and six edited metabolites: GABA, Glu, Gln, NAA, NAAG and GSH for the MAGA-sLASER. These parametric models were simulated using the NMRSIM module of the TOPSPIN suite (Version 3.6, Bruker, Rheinstetten, Germany). In order to avoid an over-estimation of GABA due to the co-edited MM for the GABA editing approach, we included one Lorentzian lineshape singlet peak as an MM signal at 3 ppm in the MEGA-sLASER basis set. Estimated metabolite concentrations that related to the total NAA (tNAA: NAA + NAAG) and CRLBs were compared between weighting strategies.

The combined spectra for different weighting approaches was evaluated by the SNR of the 3 ppm peak and the spectral fitting quality according to CRLB for the non-editing and GABA editing spectra. In order to avoid differences due to phasing between spectra, the spectral SNR was calculated in the magnitude mode. For the obtained results, a two-way analysis of variance (ANOVA) compared the group mean of the SNR for 3 ppm peaks and the CRLB values for the GABA estimation across the weighting methods using SPSS (ver. 22, IBM, Armonk, NY) in order to explore the main effect of coil number and weighting schemes and the interaction effect between them on the SNR and spectral fitting quality. The null hypothesis was that there would be no difference between coil number and weighting methods. A p-value of less than 0.05 was considered statistically significant.

4.3 Results

Figure 4.1 demonstrates SNR changes of the 3ppm peak with the number of coils used for the selective coil weighting from one representative subject. As coil numbers increase, the SNR of the 3ppm peak increases until a maximum is reached (red line). After adding data from the next coil, the SNR falls. This combination method selects the coil contributions which achieve the maximum SNR. However, for SVD, the maximum SNR, which was achieved with the reduced coil number is identical to that with full coil numbers. The average numbers of coils used for the different weighting techniques were: signal weighting: 11.4 ± 2.3, and 9.5± 1.7; SNR weighting: 10.2 ± 3.6, and 8.5± 2.1; SN^2R weighting: 7.2 ± 5.2, and 10.7± 5.3; SVD weighting: 28.3 ± 3.2 and 28.4 ± 2.5 for the non-editing and GABA editing approaches, respectively.

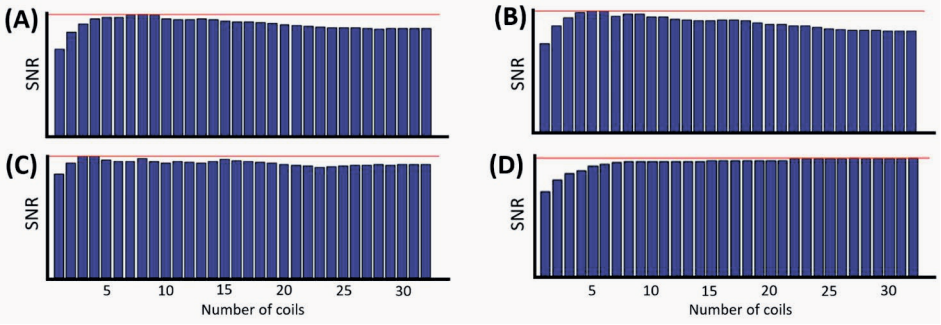

Figure 4.1. SNR changes of the 3ppm peak as a function of the number of coils used for the signal for different weighting schemes: Signal (A), SNR (B), SN^2R (C), and SVD (D) coil weighting methods from one representative subject for the non-editing acquisition. As the number of coils increases, the SNR of the 3ppm peak reaches maximum SNR at a certain coil element (red horizontal line). After adding the coil data, the SNR starts to deteriorate. However, the SVD method achieved when 22 coil date was used and its SNR is identical to that with all coil signals.

Figure 4.2 compares spectra that were combined with four different weighting methods from one exemplary subject for the non-editing acquisition (A) and GABA editing (B) methods when all coil signals (black) or selected coil signals for maximum SNR (blue) were used. The Gray line in the top panel of each fit indicates the difference between the black and blue signals. The non-editing acquisition spectra show no significant macroscopic differences in the metabolite area between weighting methods. However, when the proposed method was used that utilizes only good SNR signals (see blue lines), we found that the ghost artifact was effectively eliminated for the signal, SNR and SN^2R methods. For the SVD method, the two approaches showed identical results. For GABA editing spectra, frequency domain methods that use GABA signal as a weighting coefficient showed a clear GABA+ signal at 3 ppm in comparison with the signal weighting and SVD methods. SVD showed a relatively lower noise level in comparison with other spectra for both acquisition strategies. Note that this example case is not the best spectrum we acquired. We selected this case since it shows a typical ghost artifact reduction and qualitative differences of the 3ppm signal for different weighting schemes.

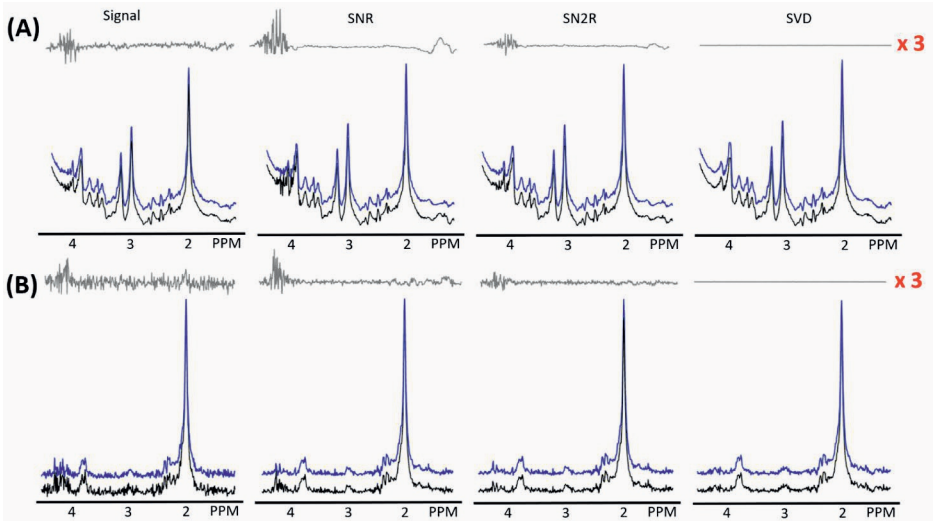

Figure 4.2. Comparison of the combined spectra processed with the four different strategies for the non-editing (A) and GABA editing (B) approaches. When all coil data (black) and the reduced number of coil data (blue) were used. The non-editing acquisition spectra show no significant macroscopic differences between weighting methods, whereas, the SNR and SN²R methods showed improved SNR of the 3ppm signal for the GABA editing approaches. Note that in order to avoid spectral pattern differences due to the different phase angle between spectra, this figure compares the magnitude mode spectra

Measured SNR of the 3 ppm peak for both acquisition approaches: the non-editing (A) and GABA edited (B) acquisitions after weighting with each combination method are shown in Figure 4.3. When all coil data were used, the non-editing and GABA edited spectra showed a similar pattern in that the SVD weighting method showed a relatively higher SNR and the signal weighting showed a lower SNR for the 3 ppm peak. When only the high SNR coils were used, all four methods showed similar SNR levels for the non-editing approach whereas the SN²R results showed the highest SNR in comparison with other three methods for the GABA editing approach.

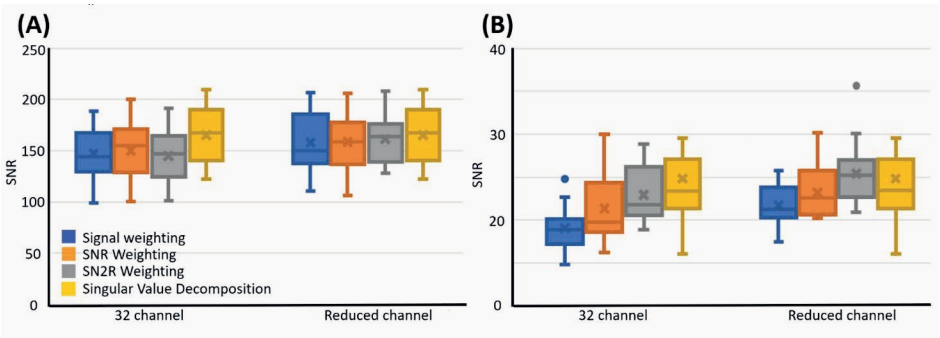

Figure. 4.3. Boxplots compare SNRs of the 3ppm peak in the non-editing (A) and GABA editing (B)approaches. In both cases, we found a somewhat higher SNR for the SVD weighting approach

in comparison with the other three approaches when we used all coil data. However, when only high SNR coil data were used, all combination approaches showed statistically similar SNRs for both acquisition approaches. Note that the horizontal lines in the middle are median values and cross marks are average values.

The ANOVA analysis showed that for the non-editing acquisition approach, the main effect for the channel number yielded an F ratio of F(1, 133) = 9.20, P=.003 indicating a significant difference between the full coil approach (147.41 ± 26.64) and reduced coil approach (160.78 ± 26.04). The main effect for weighting scheme yielded an F ratio of F(3, 133) =.304, p=.822 indicating that the differences are not significant between weighting schemes: signal (152.66 ± 25.42), SNR (154.24 ± 27.31), SN^2R (153.11 ± 25.11), and SVD (165.33 ± 27.30). The interaction effect also was not significant F(2, 133) =.222, P=.801.

For the GABA editing approach, the main effect for the channel number yielded an F ratio of F(1, 133) = 21.828, P<0.001 indicating significant difference between the full coil approach (10.85 ± 3.33) and reduced coil approach (13.62 ± 3.92). The main effect for weighting scheme yielded an F ratio of F(3, 133) = 7.828, p<0.001 indicating a significant difference between weighting schemes: signal (10.28 ± 2.72), SNR (12.07 ± 3.72), SN^2R (14.78 ± 3.63), and SVD (15.05 ± 3.91). The interaction effect was not significant F(2, 133) =.167, P=.847.

Combined signals obtained by the four different combination methods were compared with a corresponding fitting line by the LCModel analysis for the non-editing (Figure 4.4A and 4.4B) and GABA editing (Figure 4.4C and 4.4D) approaches when all coil data were used (Figure 4.4A and 4.4C) and only high sensitivity coils were used (Figure 4.4B and 4.4D). For the non-editing acquisition, there are not any clearly visible differences in fitted lines between different weighting results. However, For the GABA editing, the fitted line of the SNR weighted method showed a doublet lineshape which is consistent with that expected for edited GABA signal at 3 ppm. In the combined spectra by the SNR and SN^2R methods, we could also find a clear GABA signal at 2.28 ppm which is a partially discriminable. In addition, fitted lines showed good agreements with these signals. (highlighted in green in Figure 4.4C and 4.4D)

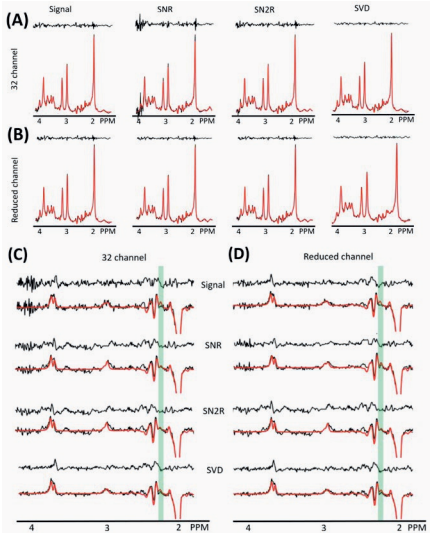

Figure 4.4. Comparison of the spectral fitting line (red) estimated by LCModel analysis for the non-editing (A and B) and GABA editing (C and D) approaches with corresponding underlying spectra (black) from the exemplary subject of Figure 4.2. When only high SNR coils were used, all combination methods showed less noise for both acquisition methods (B and D). There are not any visible differences in fitted lines between different weighting results for the non-editing acquisition. However, For the GABA editing, frequency domain methods: SNR and SN^2R weighting, showed clear 3 ppm signal as compared with that of the time-domain methods: signal and SVD methods. In addition to the 3ppm signal, partially discriminable GABA signal at 2.28 ppm showed a good agreement with the fitting lines (highlighted in green)

Figure 4.5 compares GABA concentration ratios relative to the tNAA concentration and CRLB of GABA that were estimated by the LCModel analysis across the weighting methods of the non-editing (A) and GABA editing (B) acquisition approach with an error bar of the 95% confident interval. For both approaches, there were no apparent differences in estimated GABA concentration between weighting methods. However, we found the lowest fitting error for the SVD weighting as compared with the other three approaches, which were similar when all coil data were used. However, when high SNR coil data were only used, all other methods showed improved fitting precisions and the SN^2R methods showed the lowest CRLB.

For CRLB of the GABA editing, two-way ANOVA results showed that reduced coil number and weighting schemes were significantly improved spectral fitting quality for GABA ($F(3, 133) = 16.420$, $p<0.001$ for coil number; $F(3, 133) = 3.814$, $p=.012$ for weighting scheme). However, there was no significant interaction between the effects of coil number and weighting methods, $F(1, 133) =.035$, $p = .966$. We could not find significant differences in the estimated GABA concentration across the coil number and the weighting schemes.

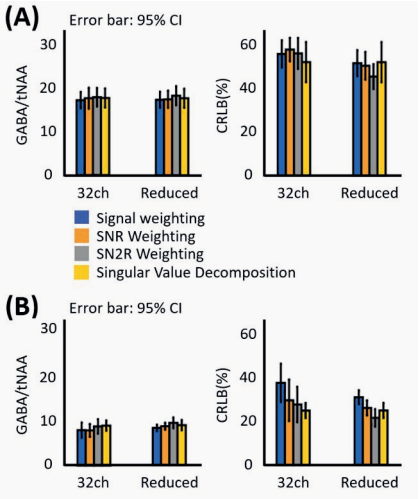

Figure 4.5. Estimated *GABA concentration ratio related to tNAA (left) and CRLB (right) estimated by LCModel analysis for the no (A) non-editing the GABA editing (B) acquisition results. There were no apparent differences in estimated GABA concentration between weighting methods. For the fitting precision, the SVD method showed good fitting reliability for GABA when all coil data used. Whereas, when high SNR coil data were only combined, all methods showed improved fitting precision. The SN^2R method showed the lowest CRLB values for GABA.*

4.4 Discussion

4.4.1 Overview

This study proposed coil combination methods that exclude low SNR coil data in order to maximize the SNR of the combined spectrum and evaluated weighted spectra based on the SNR and the spectral fitting quality for GABA quantification. The SVD method that extracts the principal signal from the noise showed a good denoising effect and also completely removed the ghost artefact. Therefore, this combination method showed a good overall SNR as compared with other approaches for both GABA acquisition approaches. However, when only high SNR data were combined, the signal, SNR and SN^2R methods also achieved a statistically similar SNR level to that of the SVD method. In addition to the SNR improvement, the high SNR coil combination methods also showed reduced levels of the ghost artifact that was present when all coil data were weighted. Improved spectral SNR resulted in improved fitting precision for estimating GABA.

4.4.2 Coil weighting with high SNR data

Since our proposed approach finds the best SNR value by varying the number of coils considered, it guarantees the same or better performance

than that achieved by fully use of all coil information. If the coil design were perfectly optimized for the position of the selected voxel then the SNR of the combined signal should improve as the number of coils used increases. However, in realistic spectroscopy situations where a single phased-array coil is used for all voxel positions, if the SNR is too low, the effect of using some coils' signals is to reduce SNR (see Figure 4.1). By excluding suboptimal coil data, the coil weighting method with the reduced coil number improved SNR of the combined spectrum. In comparison with the weighted signal with all coil data, results with the reduced coil approach showed less noise (see Figure 4.2). Accordingly, our proposed method achieved both the SNR and spectral precision improvements for the selected signal regardless of the acquisition and coil combination techniques.

One point warranting further discussion is the SVD method. This method also achieved the maximum SNR when a reduced number of coils was used, however, this achieved SNR is identical to that achieved with all coil data. In addition, this method required a number of coils close to the maximum to accomplish the best SNR. From the fact that SVD extracts the principle data from noise, we can expect it to be less sensitive to the presence of additional noise.

4.4.3 Non-editing acquisition

For the non-editing acquisition spectrum, since the 3 ppm peak, which was used to obtain the weighting coefficients, is still one of the highest concentrated signals, we found no significant differences in the spectral pattern in the metabolite area (see Figure 4.2A). Judging from the signal level at 4.2 ppm area, the SVD method effectively eliminated the ghost artifact which is a result of insufficient spoiler gradient performance for water suppression (Kreis, 2004). When all 32-channel data were used, the SVD method showed the best performance in terms of the SNR. However, the three other weighting methods: the signal, SNR and SN^2R methods that showed inferior spectral SNR with 32 coil data combination, also improved to an SNR level similar to that of the SVD result, and their SNR levels were statistically comparable. From the two-way ANOVA result, the reduced coil data approach played a more important role in improving SNR than the weighting schemes.

Our results showed that there was no significant difference in the estimated GABA concentration and the corresponding spectral fitting quality across the weighting schemes and the coil numbers. As we mentioned earlier, since the 3ppm signal, which is used as a weighting coefficient, is one of the highest peaks, weighted spectra

across the different weighting methods showed comparable spectral patterns. Accordingly, GABA estimation results were comparable. Even if the signal level at around 4.2 ppm area was different between weighting scheme and coil numbers, these differences had negligible impact on the GABA fitting since this this area is not related to the GABA resonances. An attempt to obtain coil weights that would yield a better result for GABA estimation would require LC Model analysis of individual coil data.

4.4.4 GABA editing acquisition

For the GABA editing spectra, the frequency domain approaches: SNR and SN^2R weightings showed better delineated signals at 3 ppm in comparison with the time domain approaches: signal and SVD weighting. As compared with the time domain methods that used the total signal as a weighting co-efficient, the frequency domain methods directly use the GABA+ at 3 ppm. This necessarily resulted in somewhat different spectral pattern of the weighted line at 3 ppm between time and frequency domain methods. We found a clear 3 ppm signal by the frequency domain methods. Even though the GABA editing approach has lower artifact levels since the data subtraction can eliminate persistent artifacts, the SVD method still showed a superior performance for eliminating the ghost artifact at around 4.2 ppm area and for overall noise reduction as compared with the other methods. Accordingly, the SVD method showed a good SNR improvement for the measured 3 ppm signal in comparison to the signal weighting method. LCModel analysis found statistically similar GABA concentrations regardless of the weighting scheme (see Figure 4.5B). When all coil data were combined, the SVD also showed a good spectral fitting quality for GABA. However, when high SNR data were only used, the SN2R weighting method showed the best precision across all weighting methods for the GABA fitting. Judging from the GABA $^2CH_2$ resonance which is partially discriminable at 2.28 ppm, combined in-vivo spectra by the frequency domain methods showed a good agreement with the fitting line. It is a clear evidence that the frequency domain methods are optimal for enhancing GABA for the GABA editing approach (see Figure 4.4C and 4.4D). From the fact that our two-way ANOVA results showed p-values which were smaller than 0.05 for both the SNR and CRLB, we could conclude that weighting methods and reduced coil data similarly played important roles to improve the SNR and spectral fitting precision for detecting GABA

4.4.5 Advantages

The conventional signal weighting method that uses the signal intensity of the time-domain signal as a weighting coefficient requires a dominant signal for accurate coil sensitivity estimation. Therefore, weak water suppression is recommended since this approach provides the coil weights without an additional water unsuppressed scan. However, an insufficiently suppressed water signal results in limited analog-to-digital (ADC) resolution and background noise. Moreover, the distorted baseline due to the deficient water suppression hinders accurate spectral quantification (Xi and Rocke, 2008). Whereas, since the frequency domain methods, including the selective coil weighting, do not require a dominant signal, as metabolite signals are directly used as weighting coefficients, and hence we can use strong water suppression. which can eliminate baseline distortion and spurious signals, and lead to the reliable and consistent detection of low concentration metabolites.

4.4.6 Optimal method

In comparison with other weighting methods, the SVD method showed an exceptional de-noising performance by extracting pure spectroscopy signals from noise. This advantage has also been reported by previous studies (Nguyen et al., 2013). In the situation that an acquired in-vivo spectrum contains an artifactual signal that is induced by external factors such as a patient motion or an insufficient spoiler gradient performance, SVD method is a good choice in order to improve spectral SNR and the fitting precision. This study showed it is feasible to use the SVD method with computed noise covariance matrices calculated with an internal white noise area in the in-vivo spectrum. Since the acquisition bandwidth is normally much wider than the metabolite range, this additional information is easily calculable without requiring additional scan time for the noise relation matrix, which can also be acquired by turning off the gradient pulses.

In accordance with a report by Hall et al (Hall et al., 2014), our result also showed that the SN^2R weighting method is somewhat superior to the SNR method in terms of the SNR and GABA fitting precision improvement regardless of the number of the coil. The SN^2R method in combination with the optimal coil selection showed a good GABA fitting reliability and SNR. Therefore, this approach is the preferred method for the GABA quantification for the GABA editing method.

CHAPTER 5.

Effect of linewidth on estimation of metabolic concentration when using water lineshape spectral model fitting for single voxel proton spectroscopy at 7 T

Abstract

Good B_0 field homogeneity is considered an essential requirement to obtain high quality MRS data. However, B_0 inhomogeneity can both broaden the linewidth and modify the lineshape. Deteriorated spectral quality due to the B_0 inhomogeneity hinders the precious spectral quantification. In this study, it is hypothesized that a realistic metabolite fitting model, which accounts for B_0 homogeneity on the basis of the water lineshape, will improve the consistency of estimation of metabolite concentrations across linewidths. In-vivo water suppressed/ unsuppressed single voxel spectroscopy signals were acquired under three different B_0 field homogeneity regimes. Individual realistic basis sets were created for each acquisition. Frequency-domain spectral fitting with LCModel was used to quantify the metabolite concentrations with fitting uncertainties given in terms of the Cramer-Rao lower bound. The quantification results obtained using the water lineshape basis set yielded similar concentrations independent of linewidth, and showed a larger fitting error as the linewidth increased. The conventional approach, however, quantifies metabolite concentrations with greater variations despite showing a supposedly improved fitting quality. The water lineshape basis set achieved single voxel spectroscopy consistency that is less sensitive to the linewidth compared to the conventional spectral fitting method for the range of linewidths used in this study, but the precision deteriorated with worsening B_0 field inhomogeneity. The beneficial effect was ascribed to a reduction in the number of degrees of freedom when using the water lineshape to generate the basis set.

5.1 Introduction

Nuclear magnetic resonance (NMR) spectroscopy is a widely used non-invasive technique to obtain biochemical information from the human brain. A fundamental objective of NMR spectroscopy is to measure metabolite levels within the voxel of interest (VOI). To this end, spectral fitting is commonly used along with various quantification algorithms (Provencher, 1993; Stefan et al., 2009; Wilson et al., 2011). Spectral fitting is challenging because metabolite signals have low concentrations and overlapping resonances. Moreover, unwanted factors, such as, B_0 field inhomogeneity and eddy currents, distort experimental lineshapes while simultaneously reducing the signal-to-noise ratio (SNR) (Starčuk and Starčuková, 2016). Above all, a favorable B_0 field homogeneity is an essential requirement because it directly affects the spectral lineshape. An inhomogeneous B_0 field leads to SNR reduction. It can both broaden the linewidth and cause it to deviate from a Lorentzian form. Although B_0 field shimming is a pre-requisite for spectral acquisition, shimming is not invariably successful and the well-shimmed B_0 field can be destroyed during the spectral acquisition. In particular, B_0 inhomogeneity at the ultrahigh field (UHF, 7 T and above) is more severe owing to magnetic susceptibility effects. While spectroscopy at UHF shows improved performance in detecting metabolites with enhanced SNR and spectral resolution due to the high spectral dispersion and increased sensitivity (Uğurbil et al., 2003), robust shimming techniques, such as, higher order (Chang et al., 2018) and dynamic shimming (Lemke et al., 2015) methods have been proposed to address the poorer B_0 inhomogeneity.

Most quantification methods assume that the ideal spectral lineshape can be represented using a Lorentzian function, which corresponds to exponential decay in the time domain. When experimental spectra have this ideal form with a narrow linewidth, the best quantification performance can be expected. Otherwise, additional steps are required to correct the lineshapes. Hitherto, there have been many attempts to convert arbitrary lineshapes into an analytic lineshape. We can broadly classify the previously proposed methods for correcting distorted lineshapes into those that use a reference lineshape and those that do not.

In the first approach, imperfect lineshapes due to B_0 field inhomogeneity or eddy currents are corrected by de-convolving the reference lineshape in the time domain. Some representative methods include QUALITY deconvolution (De Graaf et al., 1990) and SPREAD (Dong and Peterson, 2009; Dong et al., 2014), which use field mapping for B_0 field inhomogeneity, eddy current correction (ECC) (Klose, 1990)

for the distortion due to eddy currents, and QUECC, which is a combination of QUALITY deconvolution and ECC (Bartha et al., 2000) with advantages of both.

As mentioned earlier, in the second classification, a reference lineshape is not required. Convolution with an additional parametric or non-parametric lineshape is used. For instance, a lineshape obtained by the combination of Lorentzian and Gaussian lineshape functions, namely the Voigt lineshape, compensates the arbitrary lineshape (Marshall et al., 1997), or model-free fitting methods (Provencher, 2001; Slotboom et al., 1998) can be used to quantify metabolites using non-analytical lineshapes. The self-deconvolution method can in principle correct the distorted lineshape into an analytic form (Maudsley, 1995; Sima et al., 2009). However, in these approaches, many degrees of freedom need to be regularized by additional strategies such as the regularized lineshape deconvolution(Zhang et al., 2011; Zhang and Shen, 2013), or the regularized semi-parametric model (Sima and Van Huffel, 2006)

As multiple factors can cause the experimental lineshape to deviate from a Lorentzian form, it is challenging to precisely correct the distorted lineshapes using regular mathematical algorithms. In addition, while correcting a resultant spectrum, there is a risk of losing critical spectral information and compromising the SNR. In this study, we hypothesize that a realistic metabolite fitting model considering the B_0 homogeneity can be used to better estimate the metabolite concentration, thus obtaining fitting results that are less dependent on high B_0 field homogeneity. Similar approaches that utilize water reference lines in order to compensate for B_0 field inhomogeneity have previously been reported (Adalid et al., 2017; Li et al., 2015; Slotboom et al., 1998), the combination with LCModel, which is one of the most widely used quantification approaches, combined with human brain spectroscopy at 7T remains unexplored.

The aim of this study is to examine the degree to which the LCModel analysis is dependent on the linewidth, thus potentially improving spectral measurement in the presence of relatively broad spectral lines.

5.2 Materials and Methods

5.2.1 Basic concept of model fitting

The commonly used spectral fitting methods, which work in the frequency domain, such as, LCModel (Provencher, 2001), MIDAS (Maudsley et al., 2006), TARQUIN (Wilson et al., 2011), TDFDFit (Slotboom et al., 1998),

and ProFit (Schulte and Boesiger, 2006), quantify the relative metabolic concentrations with similar algorithms that utilize time domain fitting models in order to exploit advantages of the time domain with regard to the frequency shift, eddy current, phase and lineshape (Bottomley and Griffiths, 2016). Assuming that the experimental signal is a linear combination of the metabolite signals, the metabolite levels are determined by combining each of the simulated signals. In the case of LCModel, which is used in this study, model spectra are fitted to each metabolic signal using the Levenberg–Marquardt non-linear fitting algorithm (Levenberg, 1944), which involves solving an optimization problem. The non-parametric baseline, lipid and macromolecule (MM) signals are additionally fitted using the cubic *b*-spline simultaneously.

The ideal spectral profile of each metabolite under given experimental conditions can be predicted using quantum-mechanical calculations (Bühl and van Mourik, 2011), and these are widely accepted as prior knowledge for spectral fitting. This is the basis of spectral fitting using simulated metabolite spectra, which has proven to be a powerful approach to quantify metabolite levels. However, thus far, potential spectral lineshape modifications due to B_0 field inhomogeneity have been widely ignored in the spectral models, even though they may lead to inaccurate quantification. Instead, researchers widely depended on additional correction steps before fitting (De Graaf et al., 1990; Morris, 1988; Ordidge and Cresshull, 1986), or an additional non-parametric function during spectral fitting procedures (Kreis et al., 2005; Maudsley, 2004; Provencher, 1993; Slotboom et al., 1998; Soher et al., 1998).

The water lineshape fitting method proposed in this study can be used to directly fit the *in-vivo* spectra with their corresponding realistic lineshape models. Several assumptions are made in this approach: 1) that the lineshapes of all the metabolites are identical, and are defined by the envelope of the free induction decay (FID), and are equal to that of the water signal. 2) The chemical shifts and J-coupling for each metabolite can be specified. From these assumptions, we designed realistic metabolite models that meet these conditions using the water lineshape. We then used a water lineshape basis set for spectral fitting without modifying the resultant *in-vivo* spectra.

5.2.2 Data acquisition

MRI and MRS were performed on ten healthy human subjects (eight males; two females; 31.70 ± 4.99 years old) using a 7 T whole-body scanner (Magnetom, Siemens, Erlangen, Germany) with a 1

Tx-birdcage/ 32 Rx-loops array (Nova Medical, Wilmington, MA). Written consent was collected from each subject. The experimental protocol was approved by our institutional review board (IRB).

T_1 weighted images with 3D magnetization-prepared radio-frequency pulses and rapid gradient-echo (MPRAGE) (Mugler and Brookeman, 1990) were acquired before the spectroscopic scan as an anatomical reference. Spectroscopy was performed at the occipital cortex using the semi-localization by adiabatic selective refocusing (semi-LASER) sequence (Scheenen et al., 2008a; Scheenen et al., 2008b) with the following parameters: 8 ml isotropic voxel volume; echo time (TE) = 38 ms; repetition time (TR) = 4500 ms; number of averages = 64; bandwidth (BW) = 3500 Hz; and spectral resolution = 1024 data points.

The MRS acquisitions were repeated under three different B_0 field homogeneity conditions. The target ranges of the water linewidth under the three conditions were poor (30 to 40 Hz), medium (20 to 30 Hz), and good (10 to 20 Hz). The B_0 field homogeneity was modified by repeating FASTESTMAP (Gruetter and Tkáč, 2000) until the water linewidth reached the target condition starting at the poor linewidth and then iterating the shimming procedure so that all three bins were measured. In the situation where the initial linewidth was narrower than the target range after the first attempt by FASTESTMAP, we manually adjusted the shimming by changing the first order linear gradients (A11, B11 and A10) and second order shim currents (A20, A21, B21, A22 and B22) by the same percentage to increase the linewidth. We acquired the corresponding water lineshape by turning off the water suppression in each shim case. For the water signal acquisition, the transmitter (TX) frequency was switched to water. The number of averages for water signal acquisition was 16. The remainder of the acquisition parameters (e.g., acquisition sequence, TE, TR, B_0 field homogeneity, and spectral resolution) were kept constant between shim conditions.

5.2.3 Data processing

The model spectra of 22 metabolites: alanine (Ala), aspartate (Asp), glycerophosphocholine (GPC), choline (Cho), phosphocholine (PCh), creatine (Cr), phosphocreatine (PCr), gamma-aminobutyric acid (GABA), glucose (Glc), glutamine (Gln), glutamate (Glu), glycine (Gly), glutathione (GSH), myo-inositol (mI), lactate (Lac), N-acetyl aspartic acid (NAA), N-acetyl aspartyl glutamate (NAAG), phosphoethanolamine (PE), serine (Ser), scyllo-inositol (Scyllo), and taurine (Tau), which are typically detectable in the human brain using proton spectroscopy,

were created according to previously reported chemical shifts and coupling constants (Govind et al., 2015; Govindaraju et al., 2000). The NMRSIM module of the TOPSPIN suite (Ver. 3.6, Bruker, Rheinstetten, Germany) was used to simulate each metabolite with identical acquisition sequence and parameters that include identical radio frequency (RF) pulse profiles and timing that were used for the in-vivo acquisition.

A conventional basis set was simply created by combining the simulated metabolite models. This conventional basis set was used for all in-vivo results. The water lineshape basis set was created individually for each acquisition by multiplying the corresponding water signal with the signal profile of each metabolite in the time domain. The water signal was normalized to its maximum intensity to exclude the effect of reference voltage variations. As the amplitude of the water signal was the same for all cases, this water lineshape basis set shows identical signal amplitude ratios in every case. The only difference was in terms of the lineshape. To create the water lineshape basis set, an additional water signal is required at the expense of prolonged scan time. However. the water signal is widely required as a routine protocol to have an absolute concentration quantification and an ECC.

5.2.4 Data analysis

To verify the spectral quality under the three different B_0 field homogeneity conditions, we measured the linewidth at the half maximum points from the water signal. The SNR of the in-vivo spectrum was also measured from the NAA peak and the white noise area from 7 to 9 ppm for each case.

Linewidths of metabolites and water were also compared in order to determine whether differences in T_2 had a discernible effect on the line width. Full-width at half maximum (FWHM) of the water un-suppressed signal and clearly visible metabolite signals at 3.2 ppm (tCho: Cho + PCh + GPC), 3 ppm (tCr: Cr + PCr) and 2 ppm (tNAA: NAA + NAAG) for the three different shim conditions were measured with jMRUI software (ver. 6.0, http://www.jmrui.eu) (Stefan et al., 2009).

LCModel (Version 6.3-1L, SW Provencher, Oakville, Canada) was used to quantify the absolute metabolic concentration and estimate quantification uncertainties, using the Cramer–Rao lower bound (CRLB), which is defined as the lowest possible standard deviation of all unbiased model parameter estimates obtained from the in-vivo data (Cavassila et al., 2000; Cavassila et al., 2001). For LCModel, the mean-squared error of

any unbiased estimator, which denotes spectral parameters such as metabolite concentrations, linewidth and phase, is lower bounded by the square roots of the diagonal entries of the inverse of the Fisher information matrix, which essentially describes the correlations between spectral parameters (Zhang and Shen, 2014). As an index for the reliability of detection, decreased CRLB value is interpreted as denoting increased reliability for metabolite detection (Provencher, 1993). Prior to the spectral fitting, frequency referencing, 0^{th} and 1^{st} order phasing and ECC were performed by LCModel. Individually acquired spectra over coil elements and averages were aligned and combined by the 1^{st} point signal weighting method (Brown, 2004). Spectral fitting was performed with two different basis sets, namely the conventional basis set and the water lineshape basis set with water scaling using individual water signals, which were acquired additionally in all cases. The LCModel parameter that controls the flexibility of the spline baseline (DKNTMN) was set to 0.1 as a default value. In order to explore the effect of the baseline spine function, the conventional basis set approach was also analyzed with DKNTMN set to values that gave a similar level of baseline fluctuation as that of the water lineshape basis set. For the lineshape, we did not modify the fitting parameter that controls linewidth (i.e. DEEXT2 and DESDT2). In addition, MM and lipid models were not considered in the baseline. However, since the lineshape and linewidth of the MM and lipid are not mathematically predictable, we used internally provided non-parametric spectral models for fitting MM and lipid signals. Therefore, we did not apply the water lineshape to the spectral models for MM and lipid. As LCModel recommends (Provencher, 2016), we also assumed that water concentrations of gray matter (GM), white matter (WM), and cerebrospinal fluid (CSF) are 43300, 35880, and 55556 mM, respectively. Quantified metabolic concentrations were expressed as mmol per kg wet weight. To exclude individual variations, metabolite concentrations were individually corrected by averaged concentrations over 10 subjects as estimated at the good shim condition. For this step, we assumed that the estimated metabolite concentrations from good shim data were close to the actual concentration. Metabolite concentrations and CRLB were compared between the conventional and water lineshape methods.

The typical acceptance value for the CRLB was under 30%, as recommended by other spectroscopy studies (Bank et al., 2015). Nevertheless, we only excluded CRLB values of 999%, which indicate the situation where metabolite was not detected. Previously, Kreis has warned that arbitrarily thresholded data may cause bias (Kreis, 2016). Therefore, we used a cut off as 998% as a previous study used (Soeiro-de-Souza et al., 2016) in order to include as many metabolites as possible

and show CRLB changes between the conventional and water lineshape methods. An additional comparison was performed for the number of metabolites that was detected with CRLB below 30% and between 31 and 998% by the two approaches. The statistical significance was determined by performing ANOVA analysis between three different linewidth groups, and two methods using SPSS (Ver. 22, IBM, NY). The null hypothesis was that there is no difference between the results obtained under different B_0 homogeneity conditions.

5.3 Results

The water linewidths were 12.65 ± 2.23, 22.65 ± 2.32, and 36.16 ± 3.06(Hz) corresponding to the good, medium, and poor field homogeneity conditions, respectively. The overall range of the water linewidth was from 9.98 to 39.52 Hz. The SNRs of the in-vivo spectra were 309.89 ± 77.30, 235.68 ± 59.44, and 184.61 ± 28.20 corresponding to the good, medium, and poor field homogeneity conditions, respectively (see Figure 5.1).

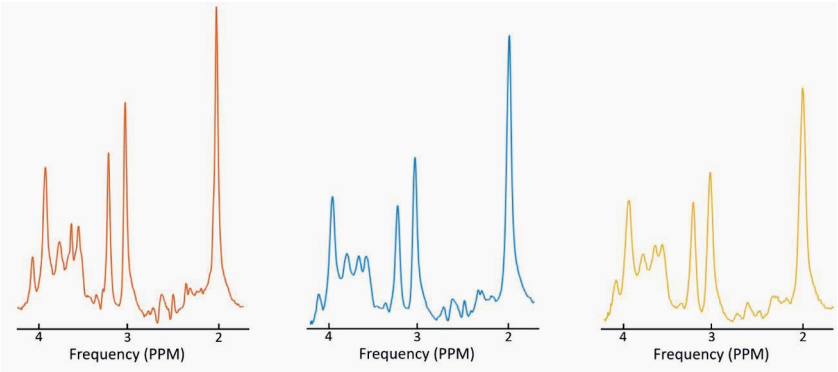

Figure 5.1. Comparison of in-vivo spectra under three B_0 field conditions from one representative subject. The mean linewidths measured from the water signal in the real mode were 12.65 ± 2.23, 22.65 ± 2.32, and 36.16 ± 3.06 (Hz) corresponding to the good (red), medium (blue), and poor (yellow) field homogeneity conditions, respectively. Their corresponding mean SNRs were 309.89 ± 77.30, 235.68 ± 59.44, and 184.61 ± 28.20, respectively.

Table 5.1 summarizes measured linewidths for the water and metabolite signals. For all shim conditions, we found comparable linewidths between the water and selected metabolite signals

Table 5.1 linewidth comparison for water and clearly visible metabolites: tCho, tCr and tNAA under three different shim condition, given as mean ± SD in Hz. Linewidths of the metabolites showed a good agreement with that of the water peak.

	Good	Medium	Poor
Water	12.7 ± 2.2	22.7 ± 2.3	36.2 ± 3.1
tCho	13.7 ± 2.5	24.4 ± 2.5	37.7 ± 1.4
tCr	13.5 ± 2.1	26.0 ± 2.6	39.3 ± 1.7
tNAA	12.1 ± 1.1	24.4 ± 2.9	37.5 ± 0.7

Figure 5.2 shows the steps for the spectral fitting model creation. The water lineshapes that acquired under each field homogeneity condition from one representative subject are compared, as shown in Figure 5.2A. As the B_0 field in the voxel becomes heterogeneous, the water lineshape changes from a Lorentzian form, and may become asymmetrical as shown for the broadest line. Figure 5.2B shows the NAA profile, which is calculated on the basis of spectral simulation using identical acquisition parameters to those used in vivo. Figure 5.2C shows a comparison of the modified basis sets under each field condition. The basis set was created by multiplying its corresponding water lineshape (see Figure 5.2A) with a simulated metabolite profile (see Figure 5.2B) in the time domain. The linewidth of the combined spectrum was dominated by that of the water. Therefore, the relatively narrow linewidth of the simulated spectrum did not affect the linewidth of the combined signal.

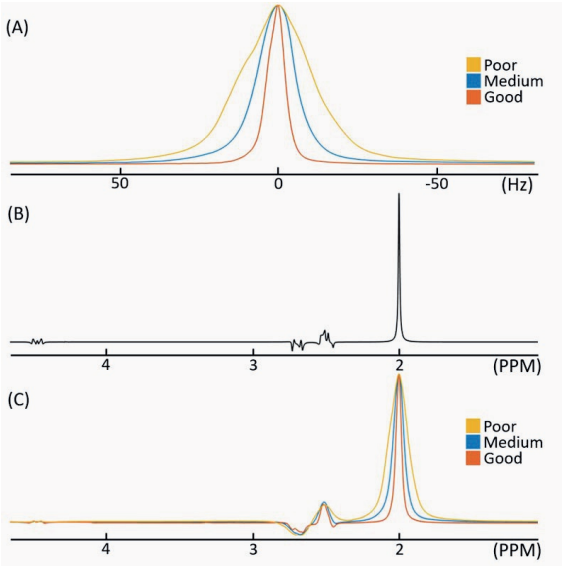

Figure 5.2. (A) Comparison of water lineshapes under three different B_0 field homogeneity conditions, namely good (red: linewidth of 11 Hz), medium (blue: 24 Hz), and poor (yellow: 39 Hz), from one representative subject. (B) Simulated NAA profile, which is widely used as a spectral fitting model. (C) Comparison of modified basis sets of NAA for the water lineshape fitting approach under each field condition. The water lineshape basis set is created by multiplying its corresponding (A) water signal with a (B) simulated metabolite profile in the time domain.

Figure 5.3 compares the average absolute concentration (A) and CRLB (B) as estimated using the conventional basis set, the conventional basis set with restricted baseline estimation and the water lineshape basis sets, for all metabolites quantified by LCModel fitting. When DKNTMN, which controls the baseline flatness, was set from 0.20 to 0.29, the baseline of the conventional basis set showed similar fluctuation levels to those of

the water lineshape basis set. Metabolites that were only detected by one method were excluded. In comparison with the conventional basis set, the water lineshape basis set tends to quantify the metabolite concentrations with lower variance for all three shimming groups. However, the water lineshape basis estimated metabolites with a greater fitting error for most metabolites. When the restricted baseline estimation is used, the conventional basis set approach estimates metabolite concentrations with a smaller variation and fitting error in comparison with the soft baseline approach for most metabolites.

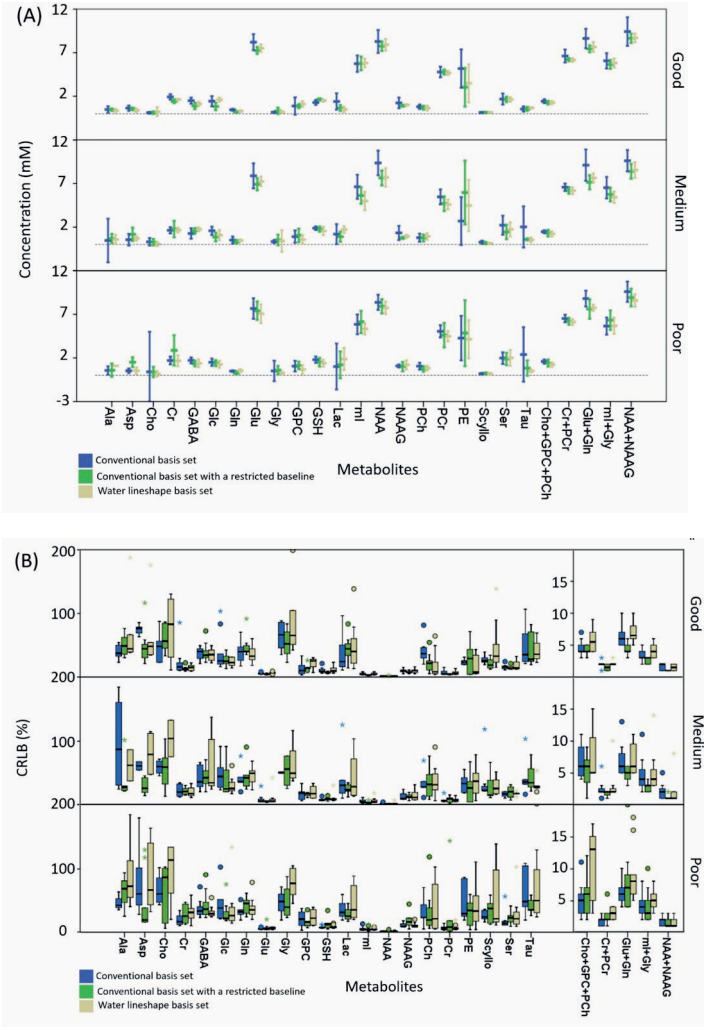

Figure 5.3. Estimated average absolute concentration with 95% confidence intervals (shown as error bars) (A) and CRLB (B) under three different shimming conditions for the conventional basis set, conventional basis set with a restricted baseline, and the water lineshape basis set, for all metabolites quantified by LCModel fitting. In comparison with the conventional basis set, the water lineshape basis set tends to show lower concentration and higher CRLB values for

most metabolites. The dotted line of the figure 5.3A indicates zero mM. Note that metabolites detected by all three approaches were only compared.

Figure 5.4 shows the comparison of the summed metabolite concentrations (A) and average CRLB (B) over all metabolites for the three different approaches under the three different static field conditions: good (10 to 20 Hz), medium (20 to 30 Hz), and poor (30 to 40 Hz) that were used for data acquisition. In this comparison, we included all detected metabolites in order to compare overall changes of concentrations and CRLBs by two methods. Below a linewidth of 30 Hz, the two methods did not show a statistical difference for either index according to the p-value, which was greater than 0.05. In the poor shim group, the three approaches showed statistically significant differences for both the concentration and the CRLB. Even if summed metabolite concentrations are not significantly different between three approaches below a linewidth of 30 Hz (p value > 0.05), the water lineshape approach showed a significantly lower variation than those of the conventional method and the conventional approach with a restricted baseline estimation for the concentration estimation. This effect was observable for all shimming groups. In addition, when the restricted baseline estimation was used, the conventional basis set method showed a smaller variation for both concentration and CRMB estimations compared to the smooth base line estimation. However, these improvements were inferior to those of the water lineshape basis set in terms of stability. This effect was observable for all shimming groups.

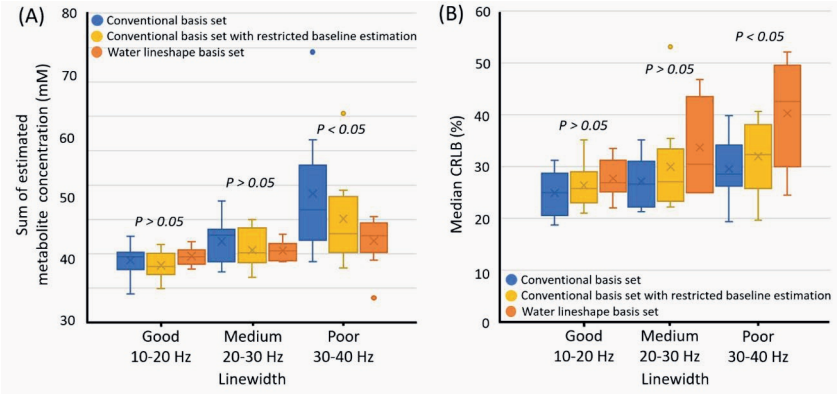

Figure 5.4. Comparisons of summed metabolite concentration (A) and median CRLB (B) over estimated metabolites by two three approaches between groups: good (10 to 20 Hz), medium (20 to 30 Hz), and poor (30 to 40 Hz) from the results shown in Figure 5.3. For linewidths of 10 to 30 Hz, the two methods did not show a statistical difference for both indexes, with p-values greater than 0.05. However, for 30 to 40 Hz linewidth, the two three approaches showed statistically significant differences for both the concentration and CRLB.

A one-way analysis of variance (ANOVA) showed that average metabolite concentrations estimated using the conventional basis set were significantly

different between shim groups ($F(2,30) = 5.184$, $p = 0.014$). On the other hand, the water lineshape basis set estimated metabolites concentrations similarly over groups ($F(2,30) = 1.484$, $p = 0.248$). The averaged CRLBs over all metabolites that were estimated with the conventional basis set and the water lineshape model basis set increased as the static field became more heterogenous (see Figure 5.4B). However, the average CRLB obtained using the water lineshape basis set increased more steeply than those of the conventional basis set. ANOVA results showed that the estimated CRLB by the conventional basis set are not significantly different between shim groups ($F(2,30) = 1.807$, $p = 0.187$); whereas, that by the water basis set are significantly different ($F(2,30) = 5.974$, $p = 0.008$).

Figure 5.5 shows the LCModel fitting results for an exemplary spectrum, with a linewidth of 39 Hz fitted using the conventional basis set, the conventional basis set with a restricted baseline estimation and the corresponding water lineshape basis set. This shows the fit for the most highly concentrated metabolites (NAA, PCh, Cr, Glu, and mI) and the baseline, for both quantification approaches. The conventional basis set showed a loose baseline constraint (Figure 5.5A) and when restricted baseline estimation was used, the conventional basis set showed a similar baseline fluctuation level to that of the water lineshape basis set (Figure 5.5B). The water lineshape basis set showed a tighter baseline (Figure 5.5C) in comparison with that of the conventional basis set. Different flexibility of the baseline constraint indicates that more degrees of freedom are required to fit with the conventional basis set. The fluctuating baseline generated from the conventional basis set made it possible to more closely fit the in-vivo lines than was possible for the water lineshape basis set. However, in this example the oscillating baseline causes unrealistic signal phasing (for example see PCh line (blue) in Figure 5.5A). In general, the estimates of metabolite concentration are higher for the conventional basis set.

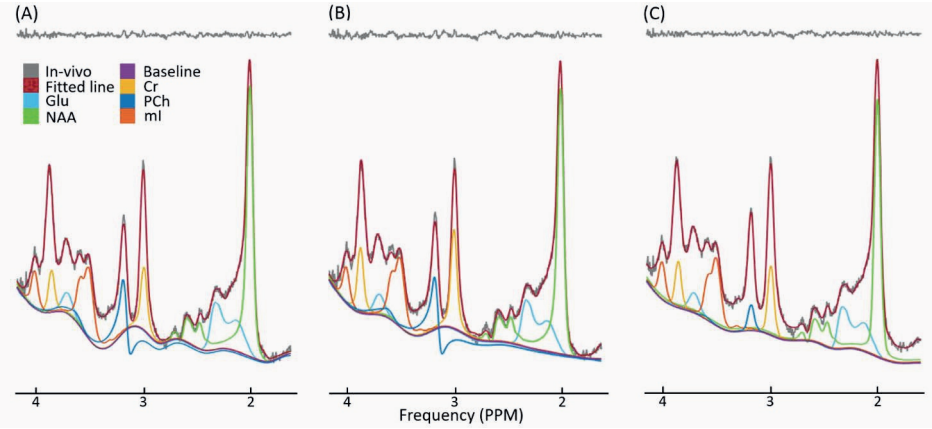

Figure 5.5. LCModel results for an exemplary spectrum, acquired with a linewidth of 39 Hz, fitted by (A) the conventional basis set, (B) the conventional basis set with restricted baseline estimation and (C) the water lineshape basis set. Fitted lines, baselines, residuals and the highest concentration metabolites (Glu, NAA, Cr, PCh, and mI) are shown. The different baselines correspond to loose (A), and tighter (B and C) baseline constraints which mean that more degrees of freedom are required to fit (A). The fluctuating baseline generated from the conventional basis set made it possible to more closely fit the in-vivo lines than was possible for the water lineshape basis set. However, in this example the oscillating baseline causes unrealistic signal phasing (for example see PCh line (blue) in Fig 5.5A). In general, the estimates of metabolite concentration are higher for the conventional basis set. The restricted baseline from the conventional basis set with constrained regularization still showed the phasing problem even if its level is decreased and there remained a higher level of the residual signal in comparison with other two approaches.

The average number of detected metabolites averaged over subjects for the two different b asis s ets, a re compared b etween t hree shimming groups in Figure 5.6. As shimming conditions get worse, both the number of detected metabolites decreased. The total number of metabolites detected was higher for the water lineshape approach for all shim groups, but the number with CRLB<30% was the same or less. When a restricted baseline estimation was used, the conventional basis set detected a decreased number of metabolites than with the other two approaches for linewidths of 20 to 30 Hz.

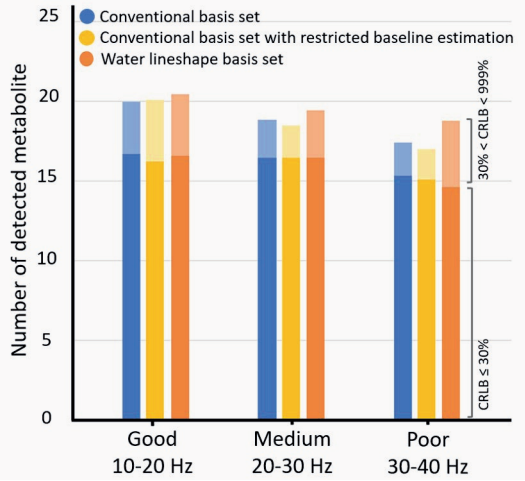

Figure 5.6. Comparison of an average number of detected metabolites for the conventional basis set and the water lineshape basis set under three shimming conditions. For all shimming conditions, the water lineshape basis set detected more metabolites than the conventional basis set. However, the number of detected metabolites by the water lineshape basis set with CRLB < 30% was the same or less than that detected by the conventional basis set for all groups. When a restricted baseline estimation was used, the conventional basis set detected a decreased number of metabolites.

5.4 Discussion

This study demonstrated the effect of linewidth on estimates of metabolite concentration when using the realistic spectral model fitting. Lineshape modifications using the reference lineshapes from the water signal (Adalid et al., 2017; Slotboom et al., 1998) or the B_0 map (Li et al., 2015) for the spectral fitting model have previously been reported. Similar to these previous studies, modified spectral models using the water lineshape in this study also improved the consistency and stability of spectral quantification for the B_0 field inhomogeneity induced broad linewidth. For most metabolites, the water lineshape fitting method estimated more consistent metabolite concentration levels with smaller variations compared to the conventional fitting method, for the different field homogeneity conditions tested. However, the conventional fitting method had numerically lower values of the CRLB parameter.

A common limitation of spectral fitting methods is their lack of uniqueness (Belkic and Belkic, 2010). The objective of non-linear or linear least square fitting is to minimize the squared deviations from the mean (SDM) between the spectral models and the experimental spectrum without considering practical metabolite levels. Therefore, spectral fitting is always at risk of over- (detecting wrong signals) and under- (missing correct signals) fitting,

in the situation that in-vivo spectra do not have enough information for accurate quantification due to the inhomogeneous B_0 field. This problem was also observed in our spectral fitting results. Even though there is no ground truth for the metabolite concentration level, if we assume that the spectral quantification result of the narrow linewidth spectrum, which was acquired under homogenous B0 field conditions, is closest to the ground truth regarding the metabolite levels, then the conventional basis over-estimated metabolite concentrations for the spectra obtained under the inhomogeneous B0 field conditions: medium and poor shim groups (see Figure 5.3A), whereas the water line shape basis gave similar estimates over the linewidth range examined. LCModel considers an additional line broadening term with a Voigt lineshape, which is the product of Lorentzian and Gaussian forms, to take into account the B0 field inhomogeneity induce broad lineshape. More importantly, LCModel finds the best compromise between the broad in-vivo peak and model utilizing the smoothest peak profile (Marshall et al., 1997). Even if, these additional line broadening terms are considered by default in the LCModel, the conventional approach quantified metabolite concentrations with greater variations than did the water lineshape basis set. Figure 5.4A also substantiates the overestimation by the conventional approach as the corresponding concentration was significantly increased (p-value <0.005) for the poor shim results.

The different degrees of freedom for spectral fitting appear to be a major reason for the difference between the two quantification approaches. As shown in Figure 5.5, the result from each method showed significantly different baseline flexibilities, which should be nearly flat in the ideal situation, because LCModel quantified MM and lipid signals using additional non-parametric models. The flexibility of the baseline determines the degrees of freedom of the baseline correction (Pradhan et al., 2016). LCModel adjusts the number of spline knots to change the spacing between knots that defines the level of freedom (Provencher, 1993). The loosely restricted baseline of the conventional approach confirms that this method has a higher degree freedom for fitting than the water lineshape fitting that showed a tightly restricted baseline. This baseline fluctuation is a typical pattern that the LCModel analysis shows for a broad linewidth (Zhang and Shen, 2014). A highly flexible baseline due to the decreased spacing between knots made it possible to closely approach the total in-vivo line. However, it also allows a relatively high degree of freedom in terms of the spectral fitting. For the closely approached fitting line to the in-vivo line, LCModel provides improved the goodness of fit by decreasing the uncertainty of fitting results. However,

improved precision does not necessarily mean that the metabolite was estimated correctly (Zhang and Shen, 2014). A fluctuating baseline may cause constrained phasing(see PCh line (blue) in Figure 5.5A) and also overestimate metabolites. The water lineshape basis set showed a flatter baseline, which is characteristic of a narrow linewidth, even though the linewidth of the *in-vivo* spectrum is broad (see Fig 5.5B). Even if T_2 relaxation times of the water and metabolites differ, the measured linewidths are similar for all shim conditions (see Table 5.1). In practice the lineshape is dominated by T_2' at ultrahigh field, and the T_2 contribution can be neglected. In comparison with the conventional basis set, the water lineshape basis set has a largely identical lineshape to the resultant spectra. Hence the line broadening part of the fitting algorithm will accommodate the lineshape thus limiting the degrees of freedom, and reducing the risk of over- or under-fitting.

LCModel allows the modification of the baseline flexibility via a hidden menu. In this study, we tested the effect of modifying the control parameter with regard to the baseline flexibility. When the restricted baseline estimation was used, the baseline of the conventional basis set showed similar fluctuation levels to those of the water lineshape basis set. A constrained baseline for the conventional basis set showed an improved quantification performance in terms of accuracy and stability in comparison with the conventional method (see Figure 5.3). However, the improvement was inferior to that of the water lineshape method (see Figure 5.4). Moreover, the arbitrarily constrained baseline failed to detect all metabolites detected by the other approaches when the B_0 field was not homogeneous. We hence conclude that the water lineshape method is generally superior to the modified conventional method.

The LCModel estimates the goodness-of-fit in the output results according to the CRLB (Provencher, 1993). This index helps in assessing the precision of the spectral fitting method. It is widely accepted that a typical exclusion cut-off for this index is 30% (Dyke et al., 2017; Godlewska et al., 2017b; Považan et al., 2018). However, recently Kreis (Kreis, 2016) pointed out that the relative CRLB as a standard index has a limitation for use as an exclusion criterion, because low concentration metabolites necessarily show high CRLB values. For this reason, we included all detected metabolites for the analyses irrespective of CRLB. A relatively broadened and flattened spectral lineshape due to poor field inhomogeneity compared to that of the good-shim spectrum has insufficient information to detect a signal with high precision, resulting in relatively larger fitting error. This explanation is commonly applied regardless of fitting methods. As shown in our results (see Figure 5.4B),

the mean CRLB increases as the linewidth broadens for both fitting approaches. Nevertheless, the water lineshape approach showed a higher mean CRLB than the conventional approach. The poorer fitting quality for the water lineshape can be explained by two reasons: the water lineshape fitting shows higher CRLB for most metabolites (see Figure 5.3B) regardless of the field inhomogeneity. In addition, this approach detects additional metabolites with relatively high CRLB values (above 30%) that were not detected by the conventional fitting method (see Figure 5.6). The Increased CRLB value of the water lineshape method was mainly driven by these two factors.

For the range of linewidths used in this study and under the assumption that an adequate water suppression can still be achieved, this study shows that the results obtained are considerably less sensitive to the linewidth for water lineshape fitting compared to the case of the conventional spectral fitting method. The spectral quantification procedure decomposes individual metabolites from the predefined *in-vivo* signal as a post processing step. An error in the estimate of one metabolite can affect the estimates of others. Although this water lineshape approach is less precise compared to the conventional approach, considering the fundamental objective of proton spectroscopy, the water lineshape fitting approach is superior to the conventional approach in terms of accuracy.

Our initial motivation for using the water lineshape method was to minimize differences between *in-vivo* and fitted model lineshapes so that LCModel quantification is less affected by the actual lineshape. In addition, we assumed that water lineshape is able to correct the lineshape better than mathematical algorithms since the lineshape modification by the B_0 field inhomogeneity is not specified and increasing the number of correction steps may cause over- or under-fitting. As the water lineshape method also relies on the lineshape correction algorithms that are inherent to LCModel (i.e., we did not turn off any lineshape and line broadening steps), the water lineshape method augments LCModel. The improvement in the stable metabolite concentration over the total metabolites confirms that the water lineshape approach in combination with LCModel fitting can be used for effective spectral estimation with enhanced accuracy in situations involving a wide linewidth.

5.5 Supplementary material

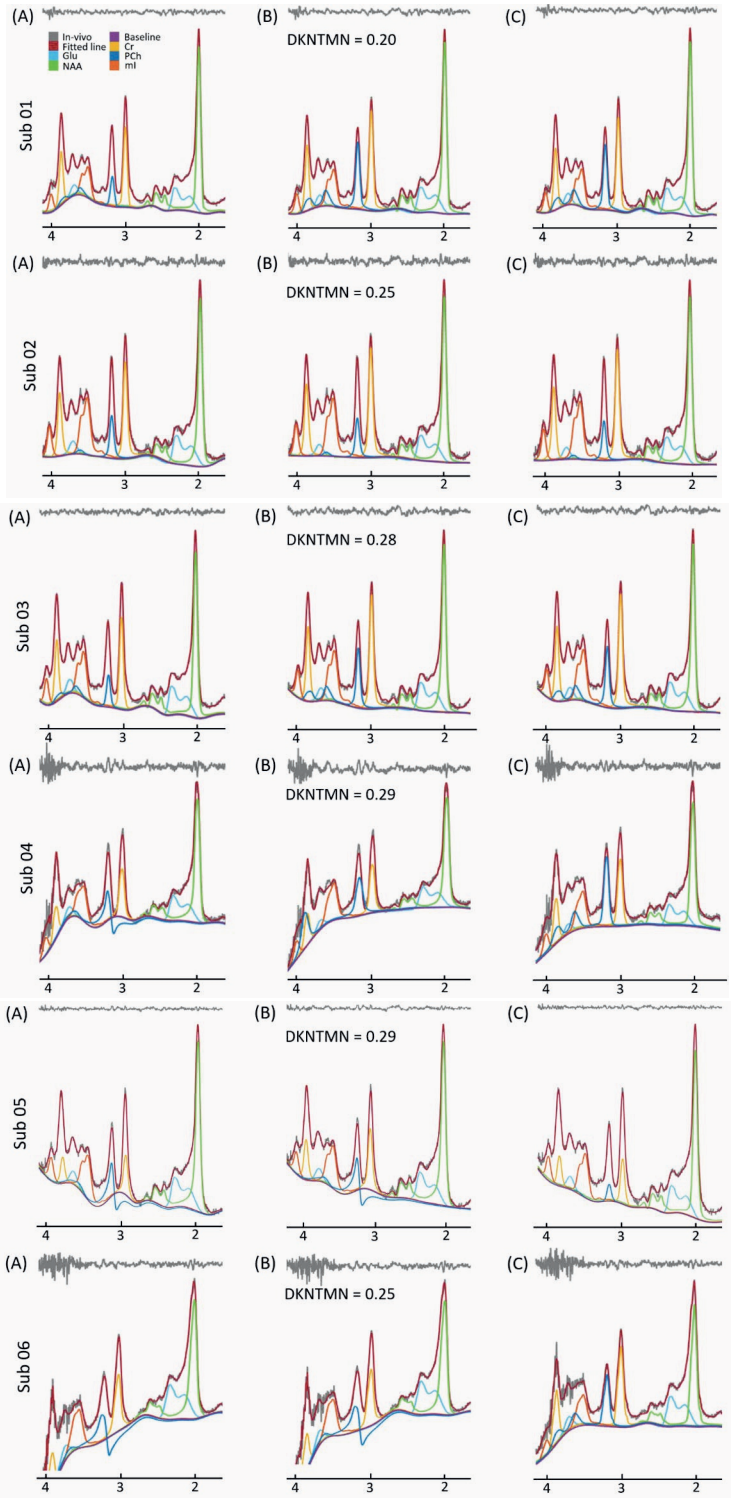

Figure 5.S1 Examples of the LCModel result that were fitted by (A) the conventional basis set, (B) the conventional basis set with restricted baseline estimation and (C) the water lineshape basis set. Fitted lines, baselines, residuals and the highest concentration metabolites (Glu, NAA, Cr, PCh, and mI) are shown. For the restricted baseline estimation, the used value of DKMTMN is shown on each Figure (B).

Table 5.S1 LCModel control parameters that were used for (A) the conventional basis set, (B) the conventional basis set with restricted baseline estimation and (C) the water lineshape basis set. Note that default values provided by LCModel were used for the unmentioned parameters

Parameter	Description (Provencher, 2016)	(A) Conventional basis set	(B) Conventional basis set with restricted baseline estimation	(C) Water lineshape basis set
attmet	the attenuation of the singlet	1.0 (Default)		
wconc	NMR-visible water concentration	35880 (Default)		
atth2o	the attenuation of water when TE=38	0.62		
namrel	basis met for relative concentration	'NAA'		
ppmst	left edge of the window	4.2		
ppmend	right edge of the window	0.6		
neach	number of metabolites for individual plots	99		
echot	echo time	38.00		
dows	water scaling	T		
doecc	eddy current correction	T		
nunfil	data points	1024		
deltat	dwell time	4.000e-04		
hzpppm	field strength	2.9715e+02		
DKNTMN	node spacing of the spline function	0.1 (Default)	0.20 ~ 0.29	0.1 (Default)

CHAPTER 6.

Implications of the magnetic susceptibility difference between grey and white matter for single-voxel proton spectroscopy at 7 T

Abstract

Magnetic susceptibility differences between grey matter (GM) and white matter (WM) can potentially affect lineshapes and chemical shifts in single-voxel spectroscopy. This study aimed to investigate the consequences and potential utility of these effects. Spectroscopy voxels were segmented into GM, WM, and cerebrospinal fluid based on T_1-weighted images. GM and WM lineshapes were computed using multi-echo gradient-echo images to measure the frequency distribution. Twenty 7 Tesla single voxel spectra with corresponding T_1-weighted images were acquired from the frontal and parietal lobes from five healthy human volunteers. Consistent frequency shifts (mean [± SD] 4.9 ± 2.0 Hz) and linewidth differences (2.4 ± 1.5 Hz) between the two tissue types were observed. Directly visible metabolites (creatine, choline, and myo-inositol) exhibited frequency shifts and linewidth differences that were consistent with a linear-weighted summation of their expected GM and WM distribution ratios. The magnetic susceptibility difference between GM and WM had a detectable effect on single-voxel proton spectra, which results in both frequency shifts and lineshape broadening. This effect can be used to estimate the relative metabolic distribution in the GM and WM for directly observable metabolites. Fractional distributions estimated with this method demonstrated good agreement with literature values for the selected metabolites.

6.1 Introduction

Magnetic resonance spectroscopy (MRS) is a widely used, non-invasive technique for the measurement of metabolite levels in the human brain. Emerging ultra-high field (≥ 7 Tesla [T]) applications can potentially deliver great benefits in MRS studies, with expected advantages including improved spectral resolution resulting from the increased chemical shift caused by the stronger static magnetic field; a simplified J-coupled spectral pattern; and a higher signal-to-noise ratio (Uğurbil et al., 2003). Ultra-high field MRS has been reported to show improved reliability for quantitative assessments of metabolites that are present at low concentrations or exhibit complex signal patterns (Tkáč et al., 2004). These advantages result in an increased number of detectable metabolites in the human brain (Tkáč et al., 2004). For these reasons, MRS is potentially more important at higher static field strengths.

However, one potential confound has, hitherto, received little attention from the spectroscopy community. Recent imaging studies have reported a potential 5–10 Hz frequency shift between grey matter (GM) and white matter (WM). Several potential causes of this phenomenon have been proposed: deoxyhemoglobin in the blood combined with different vascular densities in the GM and WM (Lee et al., 2010a; Marques et al., 2009; Reichenbach et al., 1997); different concentrations of tissue components, such as myelin (Liu et al., 2011; Ogg et al., 1999), iron (Fukunaga et al., 2010; Haacke et al., 2005; Yao et al., 2009), ferritin (Duyn et al., 2007), and calcium (Wu et al., 2009); geometry and orientation of tissue structures to the B_0 field (He and Yablonskiy, 2009; Lee et al., 2010b); and, finally, the chemical exchange effect (Luo et al., 2010; Shmueli et al., 2011; Zhong et al., 2008).

The magnetic susceptibility difference between GM and WM will generally result in a gradient of the static field at the boundary between the two tissue components, and a frequency shift. This may result in a different lineshape for metabolites in each tissue and, more importantly, a different frequency for each tissue type in spectroscopy. The recorded total signal will be the weighted sum of the signals from each tissue. The potential consequences of this effect are lineshape and frequency shifts for metabolites that are dependent on the distribution of the two tissue types.

A recent study by Maudsley *et al.* (Maudsley et al., 2017) reported a difference in metabolite frequencies that was dependent on the relative volume fractions of GM and WM. Using MRS imaging (MRSI) at 3 T, the authors found a frequency difference of approximately 0.4 Hz between GM and WM from the water frequency for N-acetylaspartate (NAA), 0.4

Hz for creatine (Cr), and 0.6 Hz for choline (Cho). In addition, these shifts exhibited a linear dependence on the relative GM and WM concentrations. This finding reflects a frequency shift for different environments. Prior to this study, Chadzynski, *et al.* (Chadzynski et al., 2011) also evaluated frequency differences for tissue-dependent variation using MRSI at 3T. The frequency differences from water to each metabolite were slightly different between GM and WM, with differences of approximately 1.2 Hz for total Cho (tCho), 0.9 Hz for total Cr (tCr), and 1.8 Hz for NAA. Based on these previous studies, the current study attempts to directly measure magnetic susceptibility-dependent frequency shifts in GM and WM by combining single-voxel proton spectroscopy at 7 T with frequency mapping using multi-echo gradient-echo (GRE) images that were acquired at the identical spectroscopy voxel position. By measuring at a number of different voxel positions, we were able to assess the way in which susceptibility differences translate into lineshape and frequency variations in practice. This technique also enabled us to compute GM and WM lineshapes and frequency distributions. For spectral lines that can be manually assigned, we examined whether the relative distribution of a metabolite between GM and WM could be estimated from the subtle differences in frequency.

6.2 Materials and Methods

6.2.1 General strategy

Because single-voxel spectroscopy (SVS) has no spatial discrimination within the voxel of interest (VOI), GM and WM signals cannot be directly distinguished from an SVS signal. Therefore, previous studies (Bank et al., 2015; Hofmann et al., 2002) acquired GM and WM signals separately from voxels where one tissue type tends to dominate. In the present study, however, a multi-echo GRE imaging approach was used that was based on the concept that an SVS signal can be considered to be an aggregation of signals from multiple mini-voxels inside a measurement volume. Each single mini-voxel signal offset can be estimated by the phase evolution of the multi-echo GRE images. By sorting mini-voxels into corresponding GM and WM components, we can obtain reference GM and WM signals, and measure the magnetic susceptibility-induced frequency shift between the GM and WM in SVS for a range of voxels.

Each mini-voxel signal has an inherent resonance frequency that can be determined by the local B_0 field strength; an amplitude determined by the spin density, flip angle, and T_1-relaxation; and a lineshape determined by the form of the T_2* relaxation envelope. Each mini-voxel *S(t)* can be expressed as:

$$S(t) = A * exp(-i\omega t) \quad (6.1)$$

in which ω is an angular frequency and A is the amplitude of the mini-voxel signal. By summing all mini-voxel signals, it is possible to obtain an estimate of the total single-voxel signal. This will, however, not be identical to that obtained in SVS because of differences in the T1-weighting of the acquisitions caused by different repetition times (TRs) between the two measurements. For the purposes of this study, however, it was adequate to obtain an estimate of the lineshape and frequency offset for GM and WM separately. Line broadening effects due to respiration were not considered explicitly, but it was assumed that these factors would not be systematically different for both tissue types in the voxel of interest.

6.2.2 Data acquisition

Both magnetic resonance imaging (MRI) and MRS data were acquired from 5 healthy volunteers (1 male, 4 female; mean age, 31.8 ± 2.64 years) using a 7 T (f_0 = 297.21 MHz) whole-body system (Magnetom, Siemens AG, Erlangen, Germany) equipped with a 32-channel phased-array head coil (NOVA Medical, MA). All examinations were performed in accordance with local ethics committee regulations. First, T_1-weighted images were acquired as an anatomical reference. A three-dimensional MPRAGE (Magnetization Prepared Rapid Acquisition Gradient Echo) sequence (Mugler and Brookeman, 1990) was used with the following parameters: matrix size = 256 * 256 * 256 resolution = 1 mm^3 isotropic voxel, TR = 2300 ms, echo time (TE) = 1.35 ms, inversion time (TI) = 1100 ms, and flip angle (FA) = 6°.

Four spectroscopy data sets were collected for different brain regions (left frontal lobe, right frontal lobe, left parietal lobe, and right parietal lobe) in each subject. Spectroscopy voxel positions were adjusted to minimize cerebrospinal fluid (CSF) contamination. To directly detect a frequency shift effect from *in-vivo* spectra, one primarily GM voxel at the occipital cortex and one primarily WM voxel at the dorsolateral prefrontal cortex were also selected. B_0 field shimming was performed using FASTESTMAP (Gruetter and Tkáč, 2000). This was repeated a maximum of 5 times to obtain the best possible B_0 field homogeneity condition. The semi-LASER (Semi-Localized by Adiabatic SElective Refocusing) sequence (Scheenen et al., 2008a; Scheenen et al., 2008b) was used to obtain spectroscopic data from an 8 cm^3 isotropic voxel, with TE = 38 ms, TR = 4500 ms, and 64 signal averages, using WET (water suppression enhanced through T_1 effects) water suppression (Ogg et al., 1994). The spectral acquisition bandwidth was 3500 Hz, which is approximately 12 parts per million (ppm) at 7 T.

Water-unsuppressed spectra were also collected from all spectroscopic voxels that were examined.

GRE imaging with four different TEs followed every spectroscopic scan to obtain a frequency offset distribution at the same location as the spectroscopic voxel with the following parameters: 1 mm^3 isotropic voxel; 3D imaging matrix = 256 * 256 * 20; TR = 60 ms; TEs = 10, 14.24, 18.48, and 22.72 ms; and FA = 20°. To have identical B_0 field homogeneity conditions, shimming steps were not applied before acquiring the GRE imaging scans. Identical image resolution and geometry coordinates to the T_1 weighted image were used to accurately map mini-voxels on the GM and WM locations.

6.2.3 Data processing

A multi-TE B_0 mapping method was used to obtain the frequency distribution within each spectroscopy voxel. The frequency offset f of each sub-voxel was estimated as follows:

$$f(x,y,z) = \Delta\theta(x,y,z)/(2\pi * \Delta TE) \tag{6.2}$$

$$\theta(x,y,z) = \arctan\left(\frac{Im_{TE}}{Re_{TE}}(x,y,z)\right) \tag{6.3}$$

in which, θ denotes the phase angle at a given TE that is obtained from the phase image. Δθ is the phase evolution per increment in TE (ΔTE, spaced by 4.24 ms). Phase changes were calculated by linear regression. A reference lineshape for the spectroscopy voxel was reconstructed by combining individual mini-voxel components of the frequency offset map on the assumption that the reconstructed reference signal is identical to that of the water signal. Segmentation of GM, WM, and CSF maps was performed using the probabilistic segmentation algorithm of SPM12 (Wellcome Trust Centre for Neuroimaging, University College London, UK) (Ashburner and Friston, 2005) on the T_1-weighted images, which were used as an anatomical reference for the spectroscopic scan. GM and WM signals were estimated by recombining frequency components of the frequency offset map at the equivalent voxel positions that corresponded to GM and WM. CSF components were excluded because they were not expected to contain significant quantities of metabolites (Joanna et al., 1993). The size of each mini-voxel is defined by the imaging resolution that is a 1 µl isotropic voxel for both T1-weighted and multi-echo images. Therefore, the spectroscopy voxel of 8 ml contains eight thousand mini voxels. GM and WM volumes were calculated by summing corresponding mini-voxels in the GM and

WM masks. Since the reconstructed lineshape showed a somewhat jagged outline due to the finite number of mini-voxels measured, we applied a 1.5 Hz Lorentzian apodisation. The same level of line broadening to the water lineshape was also applied to compare the reconstructed lineshape and water lineshape under the same conditions. Custom MATLAB (ver. 2016b, Natick, MA) scripts were used for all processing steps.

6.2.4 Data analysis

To compare the spectral similarity between a water lineshape from acquired spectroscopy data and a reconstructed reference lineshape from images, cross-correlation analysis was performed.

Widely used spectral fitting packages, such as LCModel (Provencher, 2001), jMRUI (Stefan et al., 2009), and MIDAS (Maudsley et al., 2006) include various optimization algorithms (i.e. VARPRO for LCModel; Levenberg–Marquardt for jMRUI and MIDAS) to correct potential B_0 instability or magnetic susceptibility-induced frequency shifts. Because these optimization steps are included by default, a quantification method using spectral fitting was not applied in this study to identify individual metabolite frequencies. Instead, peak position linewidths were directly measured after enhancing the spectral resolution to 1 ppb (parts per billion) by zero filling and a manual zero-order phase correction. The highest point of the peak and distance between two half-maximum points were considered to be the peak location and linewidth, respectively given as mean ± SD in Hz. The NAA location was then set as a reference position instead of the water peak to avoid any brain temperature-induced frequency shift because the temperature distribution in the human brain is not homogeneous (Maudsley et al., 2016). Under the assumption that NAA has a concentration of 52.4% in GM and 47.6% in WM (Gasparovic et al., 2009; Kreis, 1997; Maudsley et al., 2009; Pouwels and Frahm, 1998; Tal et al., 2012), the position of the NAA resonance was corrected by this fractional value based on the total frequency shift between the GM and WM of the reconstructed signal.

Three clearly observable metabolites at 4.05 ppm, 3.61 ppm, 3.20 ppm, and 3.01 ppm, designated as myo-inositol2 (MI2), MI1, Cho, and Cr, respectively, were selected to measure peak locations and linewidths. The linewidth of MI was not measured because the half-maximum height was hidden by adjacent peaks. Table 6.1 summarizes concentrations of not only these representative metabolites but also typically detectable brain metabolites. NAA was of course not examined because it was used as a reference value. All preprocessing and measurement steps were performed using the jMRUI software package (ver. 6.0, The MRUI Project) (Stefan et al., 2009).

Table 6.1. Literature concentrations and fractional distributions of typically detectable metabolites in the grey matter (GM) and white matter (WM) of the human brain, obtained by in-vivo proton spectroscopy studies.

Metabolite (Abbreviation)	Concentration (mmol/kg, wet weight* mmol/kg, water** a.u.***)		Fraction value (%)		Brain Region	Technique	Reference
	GM	WM	GM	WM			
Choline (Cho)	1.35±1.5*	1.58±1.1	46.08	53.92	Multiple	Multiple	(Kreis, 1997)
	679±12***	858±15	44.18	55.82	Frontal	MRSI	(Maudsley et al., 2009)
	1.2±0.2*	1.4±0.2	46.15	53.85	Total	MRSI	(Tal et al., 2012)
Phosphocholine (PCh)	0.2±0.2*	0.0±0.1	100	0	Centrumsemiovale & Occipital	SVS	(Hofmann et al., 2002)
Glycerophosphocholine (GPC)	1.3±0.3*	1.9±0.3	40.62	59.38	Centrumsemiovale & Occipital	SVS	(Hofmann et al., 2002)
PCh +GPC	1.3±0.1*	1.9±0.3*	40.62	59.38	Cingulate & Corona Radiata	SVS	(Bank et al., 2015)
Creatine (Cr)	8.36±0.7*	6.27±1.0	57.14	42.86	Multiple	Multiple	(Kreis, 1997)
	3145±42***	2936±59	51.72	48.28	Frontal	MRSI	(Maudsley et al., 2009)
	6.7±0.6*	4.8±0.4	58.26	41.74	Total	MRSI	(Tal et al., 2012)
	17.40±1.51**	9.05±0.93	65.81	34.09	Multiple	MRSI	(Gasparovic et al., 2009)
Phosphocreatine (PCr)	8.1±0.5*	7.8±0.5	50.94	49.06	Cingulate & Corona Radiata	SVS	(Bank et al., 2015)
Myo-inositol (MI)	5.92±1.6*	4.85±2.1	54.97	45.03	Multiple	Multiple	(Kreis, 1997)
	5.4±0.7*	4.6±0.7	54.00	46.00	Total	MRSI	(Tal et al., 2012)
N-Acetylaspartate (NAA)	10.32±0.9*	9.86 + 0.7	51.14	48.86	Multiple	Multiple	(Kreis, 1997)
	8.4±0.9**	8.0±0.9	51.22	48.78	Multiple	SVS	(Pouwels and Frahm, 1998)
	4523±59***	4857±67	48.22	51.78	Frontal	MRSI	(Maudsley et al., 2009)
	8.4±0.7*	7.6±0.5	52.50	47.50	Multiple	MRSI	(Tal et al., 2012)
	20.96±0.84**	17.22±1.61	54.86	45.14	Multiple	MRSI	(Gasparovic et al., 2009)
N-Acetylaspartylglutamic acid (NAAG)	0.9±0.5**	2.3±0.4	28.13	81.87	Multiple	SVS	(Pouwels and Frahm, 1998)

In order to investigate the contribution of each metabolite to the observed peak in the GM and WM, absolute quantification of each metabolite was performed with water scaling using LCModel (Ver. 6.3-1L, S-Provencher, ON, Canada) (Provencher, 1993, 2001) for the additionally acquired primarily GM and WM voxels.

Measured peak positions were used to examine whether we could determine the relative distribution between the GM and WM. Under the assumption that the metabolic frequency shift is given by the linear weighted sum of the metabolic distribution ratios in the GM and WM, relative concentrations in the GM and WM could then be calculated on the basis that:

$$\Delta S = \frac{([D_{WM}][F_{WM}][T_{WM}]f_{WM}+[D_{GM}][F_{GM}][T_{GM}]f_{GM})}{([D_{WM}][F_{WM}][T_{WM}]+[D_{GM}][F_{GM}][T_{GM}])} \qquad (6.4)$$

in which ΔS is the observed shift in resonance frequency from the theoretical value in Hz, $[D_{WM}]$ and $[D_{GM}]$ are the fractional concentrations in the GM and WM, $[F_{GM}]$ and $[F_{WM}]$ are tissue volume fractions in the GM and WM. The potential effect of T_2 relaxation time variation over individual metabolites was also considered. $[T_{WM}]$ and $[T_{GM}]$ are the fractional T_2 correction factor in the GM and WM.

Estimated fractional distributions, according to Equation 4, were compared with values reported in the literature. As the identifiable signals that

we measured are in fact compounds of multiple resonances located at the same chemical shift (Govindaraju et al., 2000), fractional distribution values from the literature were used to calculate the weighted average of the metabolites using the values from Table 6.1. It is important to note that metabolic concentrations reported in arbitrary units were excluded. The NMRSIM module of the Topspin package (ver. 3.6, Bruker Biospin, Rheinstetten, Germany) was used to simulate MI, glycine (Gly), Cho, phosphocholine (PCh), glycerophosphocholine (GPC), Cr, and phosphocreatine (PCr), with identical acquisition parameters to those used *in-vivo*.

6.3 Results

Figure 6.1A shows a T_1-weighted image of the 8 mL spectroscopy voxel from one representative subject in the axial plane within the spectroscopy voxel. The corresponding GM (blue), WM (green) and CSF(orange) masks, segmented on the basis of T_1-weighted images, are shown in Figure 6.1B. A frequency offset distribution, calculated by multi-echo GRE images inside the spectroscopy voxel of Figure 6.1A using a color scale with a range of 40 Hz, is shown in Figure 6.1C.

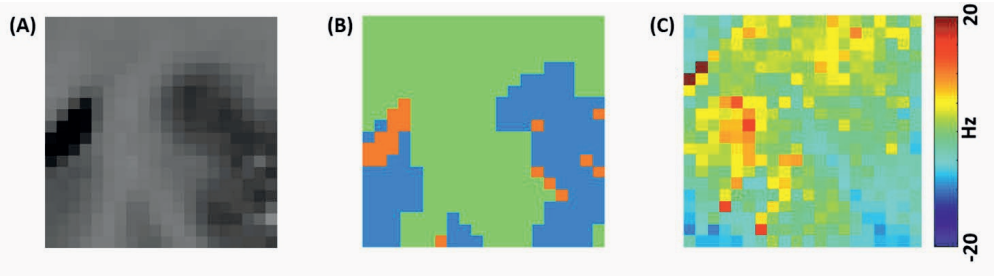

Figure 6.1. (A) A T_1-weighted image of the voxels of interest from one representative subject. (B) corresponding grey matter (GM, blue), white matter (WM, green), and cerebrospinal fluid (orange) image segmentation mask. to identify mini-voxel coordinates corresponding to GM and WM. Frequency offset map (C) calculated from multi-echo gradient-echo images inside the 8 mL spectroscopy voxel of (A). The frequency offset range is -20 Hz to 20 Hz.

Examples of each processing step from a single subject are shown in Figure 6.2. First, a water signal is shown, which was acquired from an *in-vivo* spectroscopy scan in which the water suppression was turned off (A), and a reconstructed reference signal (B) from the multi-echo imaging data. The average water linewidth in real mode was 15.7 ± 1.4 Hz for the water lineshape from the *in-vivo* scan. The average correlation coefficient between the water lineshape and reconstructed reference lineshape was 0.988 ± 0.007, over all voxels. Figure 6.2C shows a signal separation result that was generated by the corresponding frequency offset map (Figure 6.1B) and segmentation masks (Figure 6.1C). Blue and orange represent the

GM and WM, respectively. Figure 6.2D shows separate GM (blue) and WM (red) signals, as well as the water signal as a reference (yellow), normalized to the same peak value.

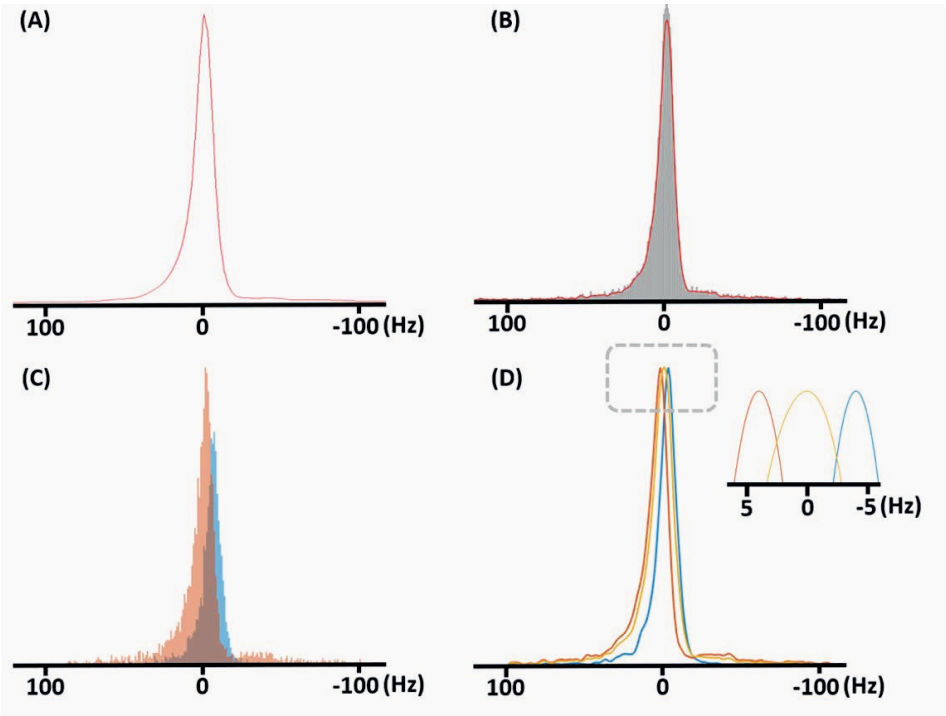

Figure 6.2. Example of an acquired spectroscopy water signal (A), shown as a reference. (B) Histogram for the frequency offset distribution (grey) of 8000 mini-voxels. The histogram outline (red) reflects the sum of the of the mini-voxel signals. As we applied line broadening of 1.5 Hz to generate a smooth lineshape from the histogram, the amplitude of the fitted line (red) is somewhat lower than actual amplitude (grey). (C) Classified mini-voxel components of the grey matter (GM, blue) and white matter (WM, red) by segmentation masks from a single subject, and (D) separated GM (blue) and WM (red) lineshapes after applying a smoothing step with a line-broadening factor of 1.5 Hz. Water (yellow) is shown as a reference lineshape. The inset to figure (D) illustrates an expanded view of frequency differences between the GM and WM lineshapes. Note that signal intensities are normalized by their maximum values to obtain an intuitive comparison.

The frequency shift relative to the NAA reference signal was found, and the linewidth difference between the separated GM and WM signals for all voxels that were examined calculated: these results are summarized in Table 6.2. The average frequency shift between the GM and WM was 4.9 Hz. The averaged GM signal was shifted 2.5 Hz in the negative frequency direction compared with the water signal, while the averaged WM signal was shifted 2.4 Hz in the positive direction. All subjects showed identical shift directions for the GM and WM signals, indicating that the shift was caused by intrinsic susceptibility differences, and not by differences in the shim.

Table 6.2. Observed frequency shift and linewidth differences between separated grey matter (GM) and white matter (WM) signals (see Figure 6.2D) from the reconstructed signal. Note that A center frequency of the reconstructed reference frequency was assumed to be 0 parts per million (ppm)

	Observed frequency shift		Observed linewidth
	(Hz)	(ppb)	(Hz)
GM	-2.5 ± 1.3	-8.4 ±4.4	14.8 ± 2.1
Difference between the GM and WM	**4.9 ± 2.0**	**16.5 ±6.7**	**2.4 ± 1.5**
WM	2.4 ± 1.3	8.1 ± 4.4	14.0 ± 2.1

Average linewidths of the GM and WM signals after separation were 14.8 ± 2.1 Hz and 14.0 ± 2.1 Hz, respectively. The difference between the averaged GM and averaged WM linewidths by $(|\sum GM_{linewidth}/n - \sum WM_{linewidth}/n|)$ was approximately 0.8 Hz. However, because the linewidth of one specific tissue type was not always wider than that of the other, individually compared linewidth differences between the two tissue types by ($|\sum(GM_{linewidth} - WM_{linewidth})|/n$) were found to be > 0.8 Hz. The mean individual linewidth difference between the GM and WM was 2.4 ± 1.5 Hz. Considering that the averaged water linewidth was 15.7 Hz, the linewidths of separated GM and WM signals were both somewhat narrower than that of the water signal.

Figure 6.3 shows the simulation results of metabolites that that constitute the signals measured at 4.05 ppm, 3.61 ppm, 3.20 ppm, and 3.01 ppm. (Figure 6.3A) Selected MI peaks at 3.6144 ppm and 4.0538 ppm were uncontaminated by Gly. Cr: PCr and PCh: GPC coincide perfectly at 3.01 ppm and 3.20 ppm, respectively (see Figure 6.3B and 6.3C). Therefore, we refer to the 3.01 ppm peak as tCr, and the 3.20 ppm peak as tCho. A significant contribution of Cho to the 3.20 ppm signal would have broadened the line by approximately 4.5 Hz, which was not observed in practice. Hence, the calculated relative distributions for these resonances between WM and GM on the basis of the literature are: MI (GM 54.49%, WM 45.51%) (Kreis, 1997; Tal et al., 2012), tCho (PCh + GPC: GM 40.62%, WM 59.38%) (Bank et al., 2015);, and tCr (Cr + PCr: GM 58.71%, WM 41.29%) (Bank et al., 2015; Gasparovic et al., 2009; Kreis, 1997; Maudsley et al., 2009; Tal et al., 2012).

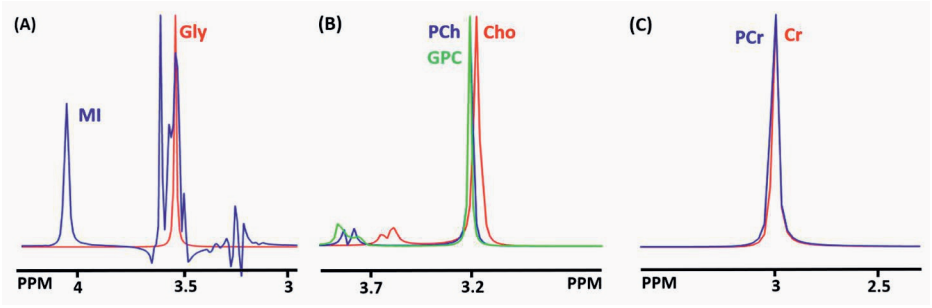

Figure 6.3. Simulated signals of (A) MI (blue) and Glycine (Gly, red), (B) choline (Cho, red), phosphocholine (PCh, blue), glycerophosphocholine (GPC, green) and (C) creatine (Cr, red) and phosphocreatine (PCr, blue). Spectral overlap of myo-inositol (MI) and Gly was not seen at the two chemical shifts where MIs were measured (4.05 and 3.6ppm, A). Because PCh and GPC have the same resonance at 3.2 ppm, and PCr and Cr have the same resonance at 3 ppm, the 3.2 ppm peak was referred to as total Cho (tCho), and the 3-ppm peak as total Cr (tCr). The fractional distribution of tCho and tCr in the grey matter and white matter were calculated by using weighted averages of the metabolite values and the corresponding absolute concentrations in millimole (mM) from Table 6.1. Note that all simulated signals were normalized to the same peak value for an accurate comparison.

Two spectra from the GM and WM voxels of one representative subject are compared in Figure 6.4A. The GM voxel had 82.9% GM and 17.1% WM, and the WM voxel had 29.9 % GM and 70.1 % WM. After NAA referencing, a clear frequency shift was observed for tCr, tCho, and MI. By contrast, two in-vivo spectra acquired from voxels that included similar tissue volume contents (74.1 %: 24.2 % and 76.0 %: 21.9 % for the GM: WM, respectively) did not show a noticeable frequency difference for the selected metabolites (Figure 6.3B). Values for the peak positions shown in Figure 6.4A are given in Table 6.3A, and absolute concentrations of the metabolites contributing to the measured peaks are also summarized in Table 6.3B. Most metabolites except GABA, GPC and Gly showed similar concentrations between the GM and WM voxel.

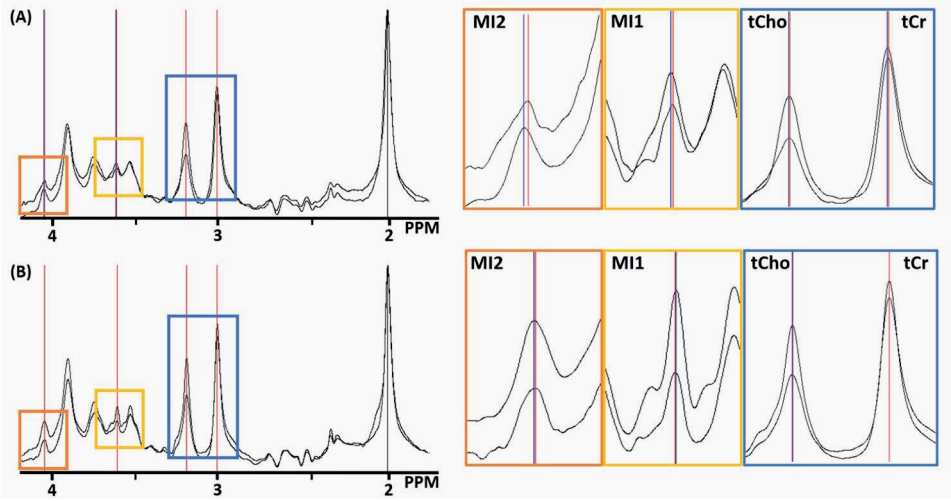

Figure 6.4. Peak position comparison of two spectra from a single subject that were acquired where the grey matter (GM) and white matter (WM) volumes differ markedly (A) 82.9%: 17.1% (GM: WM, red) and 29.9%: 70.1% (GM: WM, blue) and are near equal (B) 74.1%: 24.2% (GM: WM, red) and 76.0%: 21.9% (GM: WM, blue). Spectra from unequally distributed GM and WM voxels (A) demonstrated greater frequency differences compared with those from relatively equally distributed voxels (B). Peak positions were measured after N-acetylaspartate (NAA). This finding indicates that the measurable frequency shifts are caused by differences in voxel composition.

Table 6.3. Representative frequency differences (A) between metabolites and NAA based on data shown in Figure 6.4A and estimated metabolite concentrations with CRLB (B) by LCModel fitting for the GM and WM voxels.

(A)	Theoretical difference (ppm) (Govindaraju et al., 2000)	Observed difference (ppm)	
		GM voxel	WM voxel
tCr- NAA	1.019	1.017	1.020
tCho - NAA	1.200	1.200	1.205
MI1 - NAA	1.606	1.603	1.610
MI2 - NAA	2.046	2.042	2.050

(B)		GM voxel			WM voxel		
		Conc (mM)	CRLB (%)	/NAA	Conc (mM)	CRLB (%)	/NAA
2 ppm	NAA	8.041	1	1	7.586	2	1
	NAAG	0.674	14	0.084	0.924	10	0.122
3 ppm	Cr	1.549	12	0.193	1.297	18	0.171
	PCr	4.946	4	0.615	5.027	5	0.663
	GSH	1.777	7	0.221	1.718	7	0.214
	GABA	1.123	38	0.14	0.277	157	0.037
3.2 ppm	Cho	0	999	0	0	999	0
	PCh	0	999	0	0	999	0
	GPC	0.68	5	0.085	1.347	4	0.178
3.6 / 4 ppm	MI	4.405	5	0.548	5.162	5	0.68
	Gly	0.574	25	0.071	0.032	540	0.004

Grey matter (GM) voxel contained 82.9%: white matter (WM) voxel contained 27.1%; WM voxel had 29.9%: 70.1% (GM: WM). tCho: total choline; tCr total creatine; MI: myo-inositol; NAA: N-acetylaspartate; ppm: parts per million

Figure 6.5 shows an averaged spectrum in real mode across all 20 *in-vivo* datasets that were acquired from 4 regions in 5 subjects. The measured metabolite positions and linewidths for MI, tCho, and tCr are also summarized in Table 6.4. NAA was used as a reference peak at 2.0076 under the assumption that NAA is distributed in the ratio of 52.4:47.6 for the GM: WM. For the three other metabolites considered, we measured chemical shifts of tCr 3.0256 ppm (literature value, 3.0270 ppm), tCho 3.2096 ppm (3.2080 ppm), MI1 3.6129 ppm (3.6144 ppm), and MI2 4.0521 ppm (4.0538 ppm) relative to NAA 2.0076 ppm (2.0080 ppm), which has a frequency independent of brain temperature (Govindaraju et al., 2000).

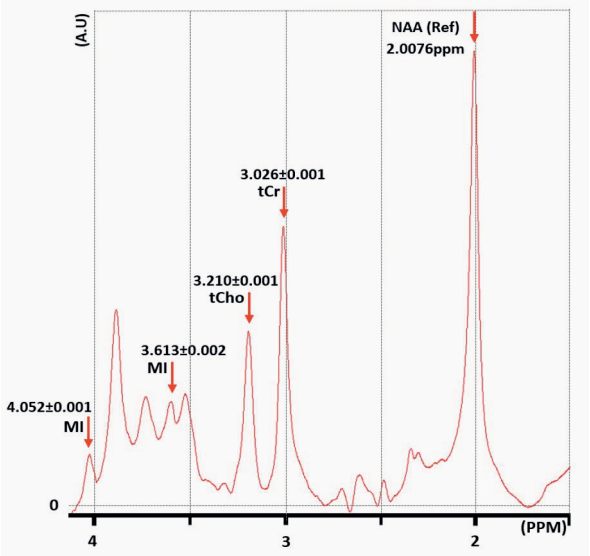

Figure 6.5. An averaged spectrum across all 20 in-vivo datasets that were acquired from 4 regions in 5 subjects N-acetyl aspartate (NAA) showing the peak locations of 4 metabolites (two myo-inositols [MI], total choline [tCho], and total creatine [tCr]), which are clearly visible. The measured locations of MI (literature values, 3.6144 parts per million [PPM] and 4.0538 ppm), tCho (3.2080 ppm), and tCr (3.0270 ppm) were at 3.613 ± 0.02, 4.0521 ± 0.02, 3.2096 ± 0.01, and 3.0256 ± 0.01 ppm, respectively, for in-vivo measurements. Note that NAA was at 2.0076 ppm as a reference peak on the assumption that NAA is distributed at an approximate ratio of 51.6:48.4 (grey matter: white matter).

Previously reported metabolic T2 relaxation times at 7 T (shown in parentheses) are as follows: tCho (GM 197 ms, WM 130 ms); tCr (GM 127 ms, WM 109 ms); and MI (GM 160 ms, 100 ms) at 7T (An et al., 2017; Marjańska et al., 2012). Individually calculated fractional distributions between the GM and WM using Equation 4 with its corresponding parameters are summarized in Table 6.4. Estimated mean fractional distribution ratios for the selected metabolites showed good agreement with the literature values that were collated from multiple literature values shown in Table 6.1.

Table 6.4. Measured frequency shifts and linewidths of metabolites in the in-vivo spectra after referencing by NAA (see Figure 6.3)

	Chemical Shift (ppm) (Govindaraju et al., 2000)		Frequency shift (Hz) a - b	Average Linewidth (Hz)	Averaged fractional distribution from Table.6.1 (%)		Estimated fractional distributions (%)	
	Theoretical[a]	Observed[b]			GM	WM	GM	WM
tCr	3.0270	3.026 ± 0.001	-0.4 ± 0.3	15.432 ± 2.341	58.71	41.29	62.27 ± 8.01	37.73 ± 8.01
tCho	3.2080	3.210 ± 0.001	0.4 ± 0.3	14.343 ± 1.465	40.62	59.38	42.48 ± 5.25	57.52± 5.25
MI1	3.6144	3.613 ± 0.002	-0.4 ± 0.3	-	54.49	45.51	61.75 ± 6.30	38.25 ± 6.30
MI2	4.0538	4.052 ± 0.001	-0.5 ± 0.3	-	54.49	45.51	60.24 ± 7.13	39.76± 7.13

The calculated distribution between grey matter (GM) and white matter (WM) on the basis of metabolic frequency shifts obtained using Equation 4, which considers segmented tissue volume fractions. Note that the theoretical distribution of GM and WM of each metabolite is calculated by weighted averaging literature values by its corresponding concentration in Table 6.1. The linewidth of MI was not measured because the half-maximum height was hidden by adjacent peaks. tCho: total choline; tCr total creatine; NAA: N-acetylaspartate; ppm: parts per million

The scatter plots shown in Figure 6.6A illustrate the estimated frequency differences from imaging between the GM and WM over B_0 field inhomogeneity. Estimated frequency shifts from imaging varied directly with B_0 field inhomogeneity. Figure 6.6B shows the proportion of each tissue type contributes to the whole frequency difference for each subject.

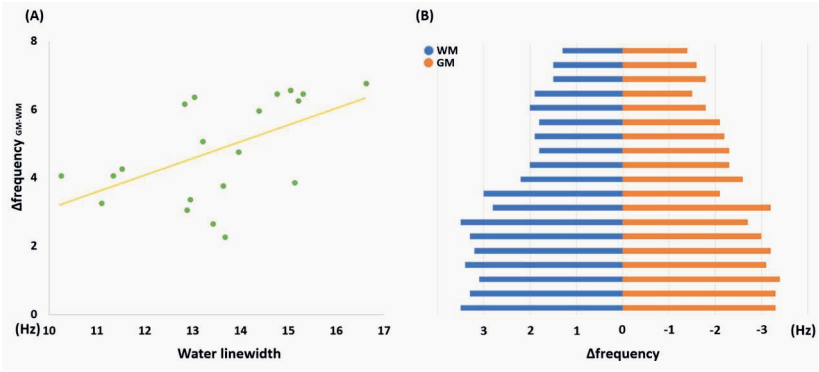

Figure 6.6. Scatter plot (A) of estimated frequency differences from imaging between grey matter (GM) and white matter (WM) as a function of water linewidth. The weak dependency of the two parameters indicates that the shim is not the main factor in determining the frequency difference. Bar plot (B) shows the frequency offsets for GM and WM for each voxel measured. The consistent difference in sign for the frequency shift measured indicates that it is caused by an intrinsic property of the tissue.

Individually calculated fractional GM distributions against the measured frequency difference between the reconstructed GM and WM signals are illustrated in the scatter graph with linear regression (solid line) and 95% confidential interval (dotted line) lines for MI (Figure 6.7A), tCho (Figure 6.7B), and tCr (Figure 6.7C). Note that the green horizontal line of each plot is a literature value of its corresponding metabolite. Averaged fractional distributions in the GM and WM are also summarized in Table 6.4. This

approach estimated consistent fractional distributions for all metabolites that were tested in good agreement with the literature values.

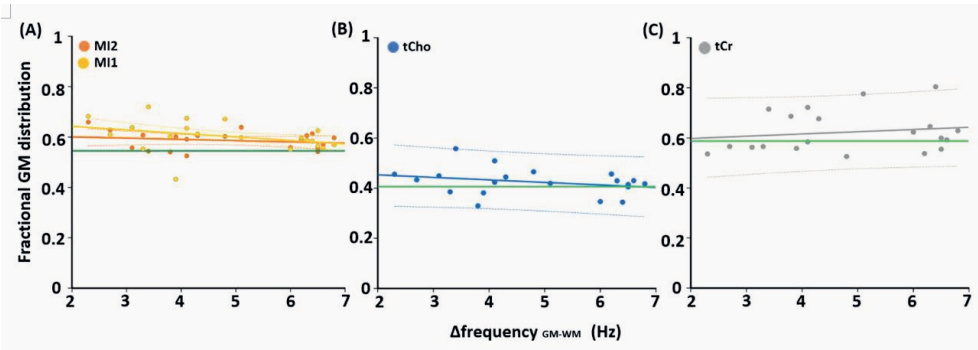

Figure 6.7. Scatter plots of the fractional grey matter (GM) distribution against the measured frequency difference between the reconstructed GM and white matter (WM) signals with linear regression (solid line) and 95% confidential interval (dotted line) lines for MI (A), total choline (tCho) (B), and total creatine (tCr) (C). These were estimated by applying Equation 4 at the single subject level. This approach estimated consistent fractional distributions for all metabolites we tested, with no obvious dependence on the frequency difference between WM and GM. Note that the green horizontal line of each plot is a literature value of its corresponding metabolite. Averaged fractional distributions in the GM and WM are also summarized in Table 6.4.

6.4 Discussion

This study demonstrates the feasibility of reconstructing a spectroscopy reference signal by imaging and separating corresponding GM and WM lineshapes directly. The frequency difference, which was calculated from separated GM and WM signals, demonstrated a level of magnetic susceptibility-induced frequency shift similar to that of other imaging experiments at 7 T (Duyn et al., 2007; Fukunaga et al., 2010; Haacke et al., 2005; Lee et al., 2010a; Lee et al., 2010b; Liu et al., 2011; Luo et al., 2010; Marques et al., 2009; Maudsley et al., 2016; Ogg et al., 1999; Reichenbach et al., 1997; Shmueli et al., 2011; Wu et al., 2009; Yao et al., 2009; Zhong et al., 2008. This frequency difference could be clearly distinguished at our experimental resolution, and led to discernible effects in the resulting spectra. The fact that metabolites may be unequally distributed between the GM and WM (Table 6.1) implies that metabolite linewidths and frequency shifts may vary slightly depending on the relative GM-to-WM distribution and volume fractions of the GM and WM in each voxel.

The following sections cover the assumptions that we made in the present study. First, we selected the NAA peak as a reference to avoid several effects that possibly could occur if the water signal was used as the reference. It is widely known that the resonance frequency can be influenced not only by magnetic susceptibility differences but also by temperature and pH changes. The maximal temperature difference across

regions in the brain parenchyma is approximately 2°C, which equals 20 ppb by temperature dependency of 0.01 ppm/°C for water (Peters et al., 1998). In addition, Lutz et al. (Lutz et al., 1993) reported that water resonance possibly changes with 0.04 ppm/pH unit for 6 < pH < 7.8. We could exclude this effect of both temperature and pH differences because the water peak was not used as a reference. However, a potential frequency shift of NAA was not investigated in the current study. Age has also been found to be an important factor that results in magnetic susceptibility changes (Li et al., 2014), and this effect was most prominently shown in NAA (Maudsley et al., 2017). We neglected this effect here because the age range of our subject group exhibited the smallest frequency shift in the previous study (Maudsley et al., 2017), and furthermore, the age range of our subjects was relatively narrow (31.8 ± 2.7 years). Besides, as NAAG is predominantly concentrated in WM, it may cause a bias of the frequency shift in the WM voxel. However, we did not consider this potential effect since NAAG has a far lower concentration than NAA. In addition to NAAG, GABA, Gly and GPC showed unequal concentrations in the GM and WM, however, concentrations of GABA and Gly were relatively much smaller than that of main metabolites: Cr and MI, respectively. In addition, GPC exclusively contributed to the 3.2 ppm peak. Therefore, the underlying low concentration metabolites are not expected to induce a bias in the measurement.

Additional cellular compartmentalization-induced effects (He and Yablonskiy, 2009) on individual metabolites were negligible because the metabolites studied here are stored in the same compartment. In fact, NAA, Cr, and Cho are mainly localized in the intracellular space (Nicolay et al., 2001), and the MI in the extracellular compartment is only at micromolar concentrations (Fisher et al., 2002). We also did not consider possible concentration variations in metabolites between regions. However, it has been shown that concentrations of NAA, Cho, Cr, and MI are comparable between the two brain regions that signals were acquired from: the frontal and parietal lobes (Maudsley et al., 2009).

Differences in the B_0 distribution between GM and WM can lead to different lineshapes and frequency offsets. The measured frequency difference between separated GM and WM signals and B_0 field inhomogeneity were only moderately linearly related (see Figure 6.6A). If for example the frequency differences we found were driven by shim quality, where the spatial distribution of GM/WM would then give rise to the frequency difference, then we would expect that there would be a strong relationship between total linewidth and frequency difference. We would also expect that the frequency difference between WM and GM would be symmetrically distributed about 0 Hz (see Figure

6.6B). The fact that we find neither effect is indicative that the frequency differences are driven primarily by susceptibility differences with a secondary effect of shim.

Using our best available shim quality (i.e. water linewidth of 15.7 ± 1.4 Hz), by iterated shimming procedures, our finding of 4.9 Hz or 16.5 ppb at 7 T demonstrated a larger degree of frequency shift between the GM and WM compared with another spectroscopy study (Maudsley, *et al.* (Maudsley et al., 2017) reported the maximal values of 4.5 ppb). Maudsley *et al.* (Maudsley et al., 2017) measured frequency differences of the GM and WM metabolite signals relative to water, whereas our shift was measured from the separated water signals obtained by imaging. When we compared the frequency difference between largely GM and WM voxels (Figure 6.3) relative to water, as was done by Maudley, *et al.* (Maudsley et al., 2017), the difference was 2.2 Hz or 6.5 ppb. Even allowing for the tissue fraction of the GM and WM voxels we tested here, our finding with this approach is relatively larger than 4.5 ppb of Maudley, *et al.* (Maudsley et al., 2017). We cannot eliminate the differences between the two studies being a consequence of different measurement environments, such as the static field strength, acquisition strategy, and measurement method. Our result is in close agreement with that of the imaging study performed by Duyn, *et al.* (Duyn et al., 2007), which reported that the mean frequency shift between the GM and WM was 4.7 Hz or 15.7 ppb at the same field strength that was used in our study.

The calculated GM-to-WM concentration ratios for the selected directly measurable metabolites are in close agreement with those in the literature (Gasparovic et al., 2009; Kreis, 1997; Maudsley et al., 2009; Tal et al., 2012) (see Table 6.4), suggesting that the measured peak position can be represented as the sum of the two peaks weighted by their GM-to-WM ratio and voxel volume fraction. As three variables, f_{GM}, f_{WM}, and ΔS of Equation 4 that were used to estimate fractional distributions in the GM and WM, were acquired at the single subject level, estimated fractional distribution values demonstrated consistency, regardless of B_0 homogeneity for all three metabolites (see Figure 6.7). Thus, for the metabolites shown in Table 6.4, this is a feasible approach to assess the GM and WM metabolite concentrations *in-vivo* by combining proton spectroscopy with multi-echo imaging.

One point warranting further discussion is the Cho signal. A comprehensive analysis encompassing the metabolic distributions of individual components of all choline-containing compounds (Cho, PCh and

GPC) is, to the best of our knowledge, currently unavailable. Instead, most studies quantify this Cho group as a single tCho signal. We assigned a chemical shift of 3.2080 ppm to tCho. However, this chemical shift value corresponds to that of PCh, and not of free Cho (Govindaraju et al., 2000). Our simulated result showed that this 3.2080 ppm peak is mainly composed of PCh and GPC, and that Cho is located at a somewhat shifted position of 3.1850 ppm. Our finding of tCho distributions of 42.35%:57.65% in the GM and WM agree fairly well with PCh + GPC concentrations in the GM and WM: 40.62%: 59.38% that were reported as PCh + GPC by Bank, *et al.* (Bank et al., 2015), and with the 43.63%: 56.36% obtained by estimating PCh and GPC separately (Hofmann et al., 2002) .

Previous studies (Khiat et al., 2000; Miller et al., 1996) have indicated that the Cho signal group consists primarily of PCh and GPC, with < 5% of the signal arising from free Cho itself. Nevertheless, this 3.2 ppm signal group is often designated as Cho. Given that the Cho literature (Kreis, 1997) reported similar absolute concentrations with PCh + GPC, with a similar fractional distribution in the GM and WM, it appears reasonable that the 3.2 ppm signal of this and other studies, is mostly representative of PCh + GPC. In addition, the measured linewidth of the 3.2 ppm signal being identical to that of the water linewidth supports the notion that PCh and GPC (which have identical chemical shifts) mainly contribute this signal; if Cho were present in significant concentrations then this would act to broaden the linewidth, as its chemical shift is 3.1850 ppm, which should then broaden the total line by approximately 4.46 Hz compared to the water signal.

The T_1 relaxation times of GM and WM have been reported by another study (Wright et al., 2008) to be approximately 1900 ms and 1120 ms, respectively, at 7 T. Ernst angles calculated from these T_1 values were 14° and 18° for the GM and WM, respectively. We used a 20° excitation, which is close to the Ernst angle of both the GM and WM. The resulting small differences in the lineshape caused by differences in T_1-relaxation appeared to be negligible (e.g., Figure 6.2). Furthermore, the major goal of this study was to investigate the frequency offset, which is independent of this effect.

Chemical shift displacement error (CSDE) is one typical limitation of SVS. However, there is no chemical shift difference between the image voxel and the water signal in SVS. Herein, we assumed that the metabolite lineshapes are identical to the water lineshape: this study did not consider CSDE as a possible source of error. It has been reported that the semi-LASER sequence we used in this study demonstrates outstanding performance to minimize the CSDE using adiabatic refocusing RF pulses with high bandwidths. The semi-LASER sequence that we used in this study has a maximal CSDE of 1.7 mm/ppm, which corresponds to 8.4% of the spectroscopy voxel. It would, in theory, be possible to extend the imaging volume so that the CSDE for each metabolite could be accounted for: this would come at the expense of some increase in the scanning duration.

In conclusion, this study identified the effects of a susceptibility difference on the GM and WM signal lineshapes and frequencies for single voxel spectroscopy. We found a level of frequency shift similar to that reported in other imaging studies. This leads to detectable increases in linewidth, an effect that will increase with further increases in the static field strength. The acquisition of additional information via imaging made it possible to estimate the relative metabolic distribution in GM and WM. This may offer a potential method for assessing metabolite concentrations in GM/WM while accounting for partial volume effects.

CHAPTER 7.

Summary

7.1 Summary

GABA is the main inhibitory neuro-transmitter; hence, it is important in behavior, cognition, and the body's response to stress in the human brain. NMR spectroscopy is a valuable modality to monitor GABA levels non-invasively. Even though ultrahigh static B_0 field and multichannel phased array receiver along with a specially designed GABA acquisition method such as the GABA editing technique improve the performance of the GABA detection, it is still difficult to accurately detect GABA owing to its low concentration. This thesis investigated methodological approaches to improve the sensitivity and reproducibility of the acquisition, and increase the accuracy and precision of the quantification for GABA at 7 T.

In **Chapter 3,** we compared two representative GABA acquisition methods, the standard acquisition and the GABA editing methods using the simultaneous acquisition of two methods using an interleaved sequence for precise comparison. GABA editing method suffers from one technical limitation; the edited GABA signal is contaminated by the co-edited MM. In this study, we found that the ability to reliably measure the GABA resonance at 2.28 ppm leads to the accurate estimates of GABA concentration without MM contamination. After compensating tissue volume and TE variations, two methods showed comparable accuracy with LCModel analysis. In addition, estimated fractional GABA concentrations in the GM and WM showed good agreement with literature values. Our proposed approach, that used the 2.28 GABA resonance, estimates pure GABA accurately without MM contamination. Our findings also confirmed that GABA is heavily concentrated in GM. Therefore, regional GM volume is an important contributor to the GABA concentration variation measured. However, the GABA editing method was superior in terms of precision.

The study presented in **Chapter 4**, assessed the coil combination techniques for GABA detection. The multichannel phased-array receiver, which normally has 16 or 32 channels, is standard hardware in the modern MR scanner. The multichannel acquisition makes it possible to improve the SNR of the acquired signal for single voxel spectroscopy together with the optimized coil weighting strategy. However, the widely-used signal weighting method is not optimal for the GABA spectroscopy. This chapter compared previously proposed weighting methods and proposed modified methods that exclude lower SNR coil data to maximize SNR. In this chapter, we assessed the coil combination strategies in terms of not only the spectral SNR improvement but also the spectral fitting precision

improvement. With the proposed coil weighting approach, the SN^2R weighting method provided reliable GABA quantification by decreasing the spectralfitting error. Judging from the spectral fitting precision, SN^2R weighting with a limited number of coils is an optimal coil combination method for both representative GABA acquisition approaches. In addition, optimized selective coil weighted combination does not require a dominant signal in the time domain; therefore, we can use strong water suppression, which can eliminate baseline distortion and spurious signals and lead to reliable and consistent detection of low concentration metabolites.

Favorable B_0 homogeneity is considered to be a critical prerequisite to obtain good results in GABA spectroscopy because it directly affects the spectral lineshape. An inhomogeneous B_0 field leads to not only SNR reduction but also broadens the linewidth and causes it to deviate from a Lorentzian form. However, shimming is not invariably successful. Most quantification algorithms assume that the spectral lineshape can be represented using a Lorentzian function. If the experimental lineshape is apparently different from the ideal form, it is difficult to expect an accurate quantification result. Even if quantification algorithms contain correction steps, it is challenging to precisely correct the distorted lineshapes using regular mathematical algorithms. In addition, while correcting a resultant spectrum, there is a risk of losing critical spectral information and compromising the SNR. In **Chapter 5,** we suggested one potential solution that uses the water lineshape fitting model for spectral fitting. This study demonstrated the effect of linewidth on the estimates of metabolite concentration when using the realistic spectral model fitting. For most metabolites, the water lineshape fitting method estimated more consistent metabolite concentration levels with smaller variations compared with the conventional fitting method, for the different field homogeneity conditions tested. However, the conventional fitting method had numerically lower values of the CRLB parameter. Although this water lineshape approach is less precise compared with the conventional approach, considering the fundamental objective of proton spectroscopy, the water lineshape fitting approach is superior to the conventional approach in terms of accuracy.

In **Chapter 6**, we investigated one confound that has, hitherto, been largely ignored by the spectroscopy community: that of a potential frequency shift caused by magnetic susceptibility differences between the grey and white matter. Imaging experiments found approximately 5 - 10 Hz frequency shift between white matter and grey matter. This study

demonstrated the feasibility of reconstructing a spectroscopy reference signal by imaging and separating corresponding GM and WM lineshapes directly. The frequency difference, which was calculated from separated GM and WM signals, found a level of magnetic susceptibility-induced frequency shift similar to that of other imaging experiments at 7 T. In addition to the frequency shift, we also found linewidth differences between the two tissue types in single-voxel spectroscopy. These findings explain the differences in the chemical shift and the linewidth of metabolites caused by the differing distributions between the grey and white matter. In addition, we demonstrated its use in quantifying the fractional distribution of metabolites in the grey and white matter. The calculated GM-to-WM concentration ratios for the selected directly measurable metabolites are in close agreement with those in the literature, suggesting that the measured peak position can be represented as the sum of the two peaks weighted by their GM-to-WM ratio and voxel volume fraction. The acquisition of additional information via imaging made it possible to estimate the relative metabolic distribution in GW and WM. This may offer a potential method for assessing metabolite concentrations in GM/WM while accounting for partial volume effects.

7.2 Future direction

The research work presented in this thesis seems to have raised more questions that it has answered. There are several possible research directions that should be pursued.

The choices of TEs of the interleaved sequence used in this study were 80 ms for the GABA-editing and 38 ms for the non-editing approaches. These TEs are slightly longer than expected values because an increased number of gradient pulses were required to have sufficient gradient performance. Ideally, 68 ms is a theoretical TE the GABA-editing method and shorter TE is better for the non-editing acquisition. Through the implementation of the acquisition sequences, it should be investigated whether both methods have similar accuracy and precision for the GABA detection when the shorter TEs are used.

Besides the GABA editing method, other spectral editing approaches such as lactate (Sotak and Freeman, 1988), glutathione (Terpstra et al., 2003) and 2-hydroxyglutarate (2HG)(Choi et al., 2012b) also suffer from the co-edited signals (e.g. co-edited NAA for GSH-editing, co-edited Glx to for 2HG-editing). As we showed in Chapter 2, the spectral fitting

approach that uses all resonance groups potentially solves the co-edited signal problem. Therefore, it should be investigated with our LCModel analysis approach in combination with the spectral acquisition at the ultrahigh field, if it is possible to solve the co-edited signal problem for other metabolite editing strategies.

The proposed coil combination method used in this thesis provides improved SNR and spectral fitting precision. This work focused on the single voxel GABA spectroscopy. Once expanded the range of its usage, this technique could be useful for magnetic resonance spectroscopy imaging (MRSI), where SNR is a major concern. By moving to other metabolites, the optimal coil combination method could be further investigated for each metabolite.

The original motivation for the development of realistic spectral fitting models in Chapter 5 was to accurately measure metabolite concentration. In Chapter 5, we showed that the realistic fitting model, which considered the lineshape modification by the B_0 field inhomogeneity, improved the accuracy in quantifying the metabolite concentration. Furthermore, in Chapter 6, we also found that magnetic susceptibility differences between the tissue types slightly modify the spectral lineshape and chemical shift. In future work, modifying the lineshape and quantifying metabolite more accurately, not only B_0 inhomogeneity but also magnetic susceptibility differences, should be considered.

Samenvatting

Samenvatting

GABA is de voornaamste inhibiterende neurotransmitter. Als gevolg is het belangrijk voor gedrag, cognitie en de reactie van het lichaam op stress in het mensenbrein. NMR-spectroscopie is een waardevolle manier om hoeveelheden GABA niet-invasief te meten. Hoewel ultrahoge statische B_0 velden en zogenaamde multichannel phased array ontvangers samen met speciaal ontwikkelde GABA-acquisitie methodes zoals GABA-bewerking technieken de kwaliteit van GABA-detectie verbeteren, is het nog steeds moeilijk om GABA correct te meten door zijn lage concentraties. Deze thesis onderzocht methodologische toepassingen om de gevoeligheid en reproduceerbaarheid van de meting te verbeteren en de correctheid en precisie van GABA-kwantificatie bij 7T te verhogen.

In **Hoofdstuk 1** worden de natuurkundige achtergrond en principes van NMR-spectroscopie uitgelegd. **Hoofdstuk 2** introduceert de voornaamste meet- en kwantificatiemethodes die in deze thesis gebruikt worden om GABA te detecteren.

In **Hoofdstuk 3** vergelijken we twee veelvoorkomende GABA meetmethodes: de standaard PRESS meting en de GABA-bewerking methode (MEGA). Wij maken gebruik van de gelijktijdige meting van de twee methodes aan de hand van een gewoven protocol voor nauwkeurige vergelijking. GABA-bewerking lijdt aan één technische beperking: het gemonteerde GABA-signaal is vervuild door de meegemonteerde macromoleculen. In dit onderzoek hebben we gezien dat het consistent kunnen meten van van de GABA-resonantie bij 2,28 ppm leidt tot correcte schattingen van GABA-concentraties zonder MM-vervuilingen. Na te hebben gecorrigeerd voor weefsels en TE variaties lieten twee methodes vergelijkbare nauwkeurigheid zien met een LCModel analyse. Daarnaast toonden geschatte GABA-concentratie fracties in de grijze en witte massa's overeenstemming met de waardes uit de literatuur. De methode die wij voorstellen, waarbij gebruik gemaakt wordt van 2,28 GABA-resonantie, schat pure GABA nauwkeurig zonder MM-vervuilingen. Onze bevindingen bevestigden ook dat GABA sterk geconcentreerd is in grijze massa. Daarom levert plaatselijk grijze massa volume een belangrijke bijdrage aan de gemeten GABA-concentratie variaties.

Het onderzoek dat in **Hoofdstuk 4** gepresenteerd wordt, toetste de spoelcombinatie technieken voor GABA-detectie. De zogenaamde multichannel phased-array ontvangers, die normaliter 16 tot 32 kanalen bevatten, is standaarduitrusting bij moderne MR-Scanners. Meten met

een veelvoud van kanalen, samen met een geoptimaliseerde spoelweging strategie, maakt het mogelijk om de SNR van het gemeten signaal per voxel spectroscopie te verbeteren. Echter is de meest-gebruikte signaalwegingsmethode niet optimaal voor GABA-spectroscopie. Dit hoofdstuk vergeleek eerder-voorgestelde wegingsmethodes en droeg een aangepaste methode voor die data afkomstig van spoelen met een lage SNR negeert om SNR te maximaliseren. In dit hoofdstuk toetsten we de spoelcombinatiestrategieën niet alleen op basis van de verbetering in de spectrale SNR, maar ook op basis van de verbetering in spectrale fitting-precisie. Met de voorgestelde spoelwegingsmethode gaf de SN2R wegingsmethode betrouwbare GABA-kwantificaties door de spectrale fitting-foutmarge te verkleinen. Kijkende naar de spectrale fitting-precisie blijkt dat SN^2R-weging met een beperkt aantal spoelen de optimale spoelcombinatiemethode voor beide GABA-meetmethodes uit hoofdstuk 3 is. Daarbij komt dat geoptimaliseerde, selectieve spoelwegingscombinatie geen dominant signaal vereist in het tijdsdomein. Daarom kunnen we sterke wateronderdrukking gebruiken, wat vervormingen in de basislijn en valse signalen elimineert en leidt tot betrouwbare en consistente detectie van lage concentratie metabolieten.

Gunstige B_0 homogeniteit wordt gezien als cruciaal om goede resultaten in GABA-spectroscopie te behalen, omdat het direct invloed heeft op de spectrale lijncontour. Een inhomogeen B_0 veld leidt niet alleen tot een verlaagde SNR, maar het verbreedt ook de lijnbreedte en zorgt ervoor dat deze afwijkt van de Lorentziaanse vorm. Veldcorrecties zijn echter niet altijd succesvol. De meeste kwantificatiealgoritmes nemen de aanname dat de spectrale lijncontour vertegenwoordigd kan worden met een Lorentziaanse functie. Als de experimentele lijncontour blijkt af te wijken van de ideale vorm, dan is het irreëel een correct kwantificatieresultaat te verwachten. Zelfs wanneer kwantificatiealgoritmes een correctiestap meenemen, dan blijft het uitdagend om de vervormde lijncontouren goed te corrigeren met alledaagse wiskundige algoritmes. Daarnaast bestaat tijdens het corrigeren van een resulterend spectrum het risico dat cruciale spectrale informatie verloren gaat en dat de SNR in het geding komt. In **Hoofdstuk 5** stellen we één potentiële oplossing voor die gebruik maakt van het fittingmodel van het waterlijncontour voor spectrale fitting. Dit onderzoek demonstreerde wat het effect is van de lijnbreedte op de geschatte waardes van metabolietconcentraties wanneer gebruik wordt gemaakt van de realistische spectrale modelfitting. Voor de meeste metabolieten gaf de waterlijncontourfittingmethode een meer consistente schatting van metabolietconcentratieniveaus met kleinere

variaties vergeleken met de gevestigde fittingmethode, onder verschillende veldinhomogeniteiten die zijn getest. De gevestigde fittingmethode had echter numeriek lagere CRLB-waardes. Hoewel deze waterlijncontourmethode minder precies is in vergelijking met de gevestigde manier, is de waterlijncontourfittingmethode, met de doelen die ten grondslag liggen aan proton spectroscopie in gedachte, superieur aan de gevestigde methode op het gebied van correctheid.

In **Hoofdstuk 6** onderzochten we één beïnvloedende factor die, tot nu toe, merendeels is genegeerd door de spectroscopiegemeenschap: de potentiële frequentieverschuiving veroorzaakt door magnetische susceptibiliteitsverschillen tussen grijze en witte massa. Imagingexperimenten lieten een frequentieverschuiving zien van ongeveer 5 – 10 Hz tussen grijze en witte massa. Dit onderzoek toonde dat het haalbaar is om een spectroscopisch referentiesignaal te reconstrueren door corresponderende grijze- en witte-massalijncontouren direct in beeld te brengen en te scheiden. Het frequentieverschil, welk berekend was uit gescheiden grijze- en witte-massasignalen, vertoonde een door magnetische-susceptibiliteit-veroorzaakt frequentieverschilniveau vergelijkbaar met dat van andere imaging experimenten bij 7T. Naast het frequentieverschil zagen we ook lijnbreedteverschillen tussen deze twee weefsels in spectroscopie van één voxel. Deze bevindingen verklaren de verschillen in de chemische verschuiving en de lijnbreedte van metabolieten die veroorzaakt worden door de verschillende verdelingen tussen grijze en witte massa. Daarnaast demonstreerden we de toepassing hiervan bij het kwantificeren van de fractionele distributies van metabolieten in de grijze en witte massa. De berekende grijze-tot-witte-massaconcentratieverhoudingen voor de geselecteerde, direct-meetbare metabolieten komen nauw overeen zoals ze in de literatuur gevonden kunnen worden, wat suggereert dat de gemeten piekpositie gerepresenteerd kan worden als de som van de twee pieken, gewogen aan de hand van de grijze-tot-witte-massaverhouding en de voxelgroottefractie. De meting van verdere informatie via imaging stond het toe om de relatieve metabolietdistributie in grijze en witte massa te schatten. Dit kan een potentiële methode bieden om metabolietconcentraties in grijze en witte massa te beoordelen terwijl er rekening gehouden wordt met deelvolume-effecten.

List Of Publications

List of Publications

Hong, Y.J., Kim, T.K., **Hong, D.**, Park, C.H., Yoo, S.J., Wickum, M.E., Hur, J., Lee, H.J., Kim, Y.J., Suh, Y.J. and Greiser, A., 2016. Myocardial characterization using dual-energy CT in doxorubicin-induced DCM: comparison with CMR T1-mapping and histology in a rabbit model. JACC: Cardiovascular Imaging, 9(7), pp.836-845.

Thielen, J.W., **Hong, D.**, Rohani Rankouhi, S., Wiltfang, J., Fernandez, G., Norris, D.G. and Tendolkar, I., 2018. The increase in medial prefrontal glutamate/glutamine concentration during memory encoding is associated with better memory performance and stronger functional connectivity in the human medial prefrontal–thalamus–hippocampus network. Human brain mapping, 39(6), pp.2381-2390.

Rohani Rankouhi, S., **Hong, D.**, Dyvorne, H., Balchandani, P. and Norris, D.G., 2018. MASE-sLASER, a short-TE, matched chemical shift displacement error sequence for single-voxel spectroscopy at ultrahigh field. NMR in Biomedicine, 31(7), p.e3940.

Kim, P.K., Hong, Y.J., Sakuma, H., Chawla, A., Park, J.K., Park, C.H., **Hong, D.**, Han, K., Lee, J.Y., Hur, J. and Lee, H.J., 2018. Myocardial Extracellular Volume Fraction and Change in Hematocrit Level: MR Evaluation by Using T1 Mapping in an Experimental Model of Anemia. Radiology, 288(1), pp.93-98.

Hong, D., van Asten, J.J., Rankouhi, S.R., Thielen, J.W. and Norris, D.G., 2018. Implications of the magnetic susceptibility difference between grey and white matter for single-voxel proton spectroscopy at 7 T. Journal of Magnetic Resonance, 297, pp.51-60.

Thielen, J.W., Gancheva, S., **Hong, D.**, Rohani Rankouhi, S., Chen, B., Apostolopoulou, M., Anadol-Schmitz, E., Roden, M., Norris, D.G. and Tendolkar, I., 2019. Higher GABA concentration in the medial prefrontal cortex of Type 2 diabetes patients is associated with episodic memory dysfunction. Human brain mapping, 40(14), pp.4287-4295.

Hong, D., van Asten, J.J., Rankouhi, S.R., Thielen, J.W. and Norris, D.G., 2019. Effect of linewidth on estimation of metabolic concentration when using water lineshape spectral model fitting for single voxel proton spectroscopy at 7 T. Journal of Magnetic Resonance, 304, pp.53-61.

Hong, D., Rohani Rankouhi, S., Thielen, J.W., van Asten, J.J. and Norris, D.G., 2019. A comparison of sLASER and MEGA-sLASER using simultaneous interleaved acquisition for measuring GABA in the human brain at 7T. PloS one, 14(10), p.e0223702.

Hong, D., Rohani Rankouhi, S., Thielen, J.W., van Asten, J.J. and Norris, D.G., Optimal phased-array signal combination strategies from separate coil elements for GABA spectroscopy at 7T, In preparation

Acknowledgments

Acknowledgments

I wish to extend my eternal gratitude and immense thanks to each one of you for helping me to achieve the greatest personal accomplishment of my life.

First of all, I would like to thank my supervisor, Prof. David Norris. This thesis would not have been possible without his constant tutelage, guidance, support, and commitment.

I would also like to thank my supervisory committee members, Prof. Arend Heerschap, Prof. Roland Kreis, and Prof. Jamie Near. I also would like to thank Prof. Harald Quick and Prof. Mark Ladd for their encouragement and enthusiasm throughout my project. Additionally, I would like to express my gratitude to Prof. Hernán Jara and Prof. Osamu Sakai in Boston.

Many thanks go to my project partners: Seyedmorteza Rohani Rankouhi and Jan-Willem Thielen. It has been truly great to work with you guys. I also appreciate Sjaak van Asten. His kind and generous sharing of technical information helped my projects to progress smoothly.

I already miss both our former and current ELH members in Essen: Oliver Kraff, Maximilian Völker, Bixia Chen, Stefan Rietsch, Marcel Gratz, Stephan Orzada, Sascha Brunheim, Stefan Maderwald, Thomas Ernst, Sören Johst, Viktor Pfaffenrot, Peter Koopmans, Yacine Noureddine, Lena Schäfer, Beate Fraß, Corinna Heldt, Judith Kösters and Sigrid Radermacher. All your kind and warm consideration made for a wonderful and unforgettable five years in Germany.

I would also like to thank our MR technique members in Nijmegen: Daniel Gomez, Jennifer Schulz, Irati Markuerkiaga, Bart Gips, Lauren Bains, Rasim Boyacioglu, Jose Marques, Kwok Shing Chan, Tim van Mourik, Zahra Fazal, Riccardo Metere, and Marcel Zwiers. Even if we did not see each other every day, our seminars and physics club meetings were always good.

Finally, to my parents, sister, brother in law, nephew Jaeha and all my friends, who are far too numerous to thank individually for all their love and support—a resounding THANK YOU!

vielen Dank für alles!!

Bibliography

Bibliography

Adalid, V., Döring, A., Kyathanahally, S.P., Bolliger, C.S., Boesch, C., Kreis, R., 2017. Fitting interrelated datasets: metabolite diffusion and general lineshapes. Magnetic Resonance Materials in Physics, Biology and Medicine 30, 429-448.

An, L., Li, S., Shen, J., 2017. Simultaneous determination of metabolite concentrations, T1 and T2 relaxation times. Magnetic Resonance in Medicine 78, 2072-2081.

Andreychenko, A., Boer, V.O., Arteaga de Castro, C.S., Luijten, P.R., Klomp, D.W., 2012. Efficient spectral editing at 7 T: GABA detection with MEGA-sLASER. Magnetic Resonance in Medicine 68, 1018-1025.

Andreychenko, A., Klomp, D.W., de Graaf, R.A., Luijten, P.R., Boer, V.O., 2013. In vivo GABA T2 determination with J-refocused echo time extension at 7 T. NMR in Biomedicine 26, 1596-1601.

Ashburner, J., Friston, K.J., 2005. Unified segmentation. Neuroimage 26, 839-851.

Bai, X., Edden, R.A., Gao, F., Wang, G., Wu, L., Zhao, B., Wang, M., Chan, Q., Chen, W., Barker, P.B., 2015. Decreased γ-aminobutyric acid levels in the parietal region of patients with Alzheimer's disease. Journal of Magnetic Resonance Imaging 41, 1326-1331.

Banerjee, A., Ganji, S., Hulsey, K., Dimitrov, I., Maher, E., Ghose, S., Tamminga, C., Choi, C., 2012. Measurement of glycine in gray and white matter in the human brain in vivo by 1H MRS at 7.0 T. Magnetic Resonance in Medicine 68, 325-331.

Bank, B., Emir, U., Boer, V., Asten, J., Maas, M., Wijnen, J., Kan, H., Oz, G., Klomp, D., Scheenen, T., 2015. Multi-center reproducibility of neurochemical profiles in the human brain at 7 T. NMR in Biomedicine 28, 306-316.

Bartha, R., Drost, D., Menon, R., Williamson, P., 2000. Spectroscopic lineshape correction by QUECC: combined QUALITY deconvolution and eddy current correction. Magnetic Resonance in Medicine 44, 641-645.

Behar, K.L., Ogino, T., 1993. Characterization of macromolecule resonances in the 1H NMR spectrum of rat brain. Magnetic Resonance in Medicine 30, 38-44.

Behar, K.L., Rothman, D.L., Spencer, D.D., Petroff, O.A., 1994. Analysis of macromolecule resonances in 1H NMR spectra of human brain. Magnetic Resonance in Medicine 32, 294-302.

Belkic, D., Belkic, K., 2010. Signal processing in magnetic resonance spectroscopy with biomedical applications. CRC Press.

Bellance, N., Pabst, L., Allen, G., Rossignol, R., Nagrath, D., 2012. Oncosecretomics coupled to bioenergetics identifies α-amino adipic acid, isoleucine and GABA as potential biomarkers of cancer: Differential expression of c-Myc, Oct1 and KLF4 coordinates metabolic changes. Biochimica Et Biophysica Acta (BBA)-Bioenergetics 1817, 2060-2071.

Bhagwagar, Z., Wylezinska, M., Jezzard, P., Evans, J., Ashworth, F., Sule, A., Matthews, P.M., Cowen, P.J., 2007. Reduction in occipital cortex γ-aminobutyric acid concentrations in medication-free recovered unipolar depressed and bipolar subjects. Biological Psychiatry 61, 806-812.

Bhagwagar, Z., Wylezinska, M., Jezzard, P., Evans, J., Boorman, E., Matthews, P.M., Cowen, P.J., 2008. Low GABA concentrations in occipital cortex and anterior cingulate cortex in medication-free, recovered depressed patients. International Journal of Neuropsychopharmacology 11, 255-260.

Bhattacharyya, P., Phillips, M., Stone, L., Lowe, M., 2011. In-vivo MRS measurement of gray-matter and white-matter GABA concentration in sensorimotor cortex using a motion-controlled MEGA-PRESS Sequence. Magnetic Resonance Imaging 29, 374.

Bland, J.M., Altman, D., 1986. Statistical methods for assessing agreement between two methods of clinical measurement. The lancet 327, 307-310.

Bloch, F., 1946. Nuclear induction. Physical Review 70, 460.

Boer, V., van Lier, A., Hoogduin, J., Wijnen, J., Luijten, P., Klomp, D., 2011. 7-T 1H MRS with adiabatic refocusing at short TE using radiofrequency focusing with a dual-channel volume transmit coil. NMR in Biomedicine 24, 1038-1046.

Bogner, W., Hangel, G., Esmaeili, M., Andronesi, O.C., 2017. 1D-spectral editing and 2D multispectral in vivo1H-MRS and 1H-MRSI-Methods and applications. Analytical Biochemistry 529, 48-64.

Bottomley, P., Charles, H., Roemer, P., Flamig, D., Engeseth, H., Edelstein, W., Mueller, O., 1988. Human in vivo phosphate metabolite imaging with 31P NMR. Magnetic Resonance in Medicine 7, 319-336.

Bottomley, P.A., 1984. Selective volume method for performing localized NMR spectroscopy. Google Patents.

Bottomley, P.A., Griffiths, J.R., 2016. Handbook of magnetic resonance spectroscopy in vivo: MRS theory, practice and applications. John Wiley & Sons.

Brown, M.A., 2004. Time-domain combination of MR spectroscopy data acquired using phased-array coils. Magnetic Resonance in Medicine 52, 1207-1213.

Bühl, M., van Mourik, T., 2011. NMR spectroscopy: quantum-chemical calculations. Wiley Interdisciplinary Reviews: Computational Molecular Science 1, 634-647.

Cai, K., Haris, M., Singh, A., Kogan, F., Greenberg, J.H., Hariharan, H., Detre, J.A., Reddy, R., 2012. Magnetic resonance imaging of glutamate. Nature Medicine 18, 302.

Cavassila, S., Deval, S., Huegen, C., Van Ormondt, D., Graveron-Demilly, D., 2000. Cramer-Rao bound expressions for parametric estimation of overlapping peaks: influence of prior knowledge. Journal of Magnetic Resonance 143, 311-320.

Cavassila, S., Deval, S., Huegen, C., Van Ormondt, D., Graveron-Demilly, D., 2001. Cramér–Rao bounds: an evaluation tool for quantitation. NMR in Biomedicine: An International Journal Devoted to the Development and Application of Magnetic Resonance In vivo 14, 278-283.

Cawley, N., Solanky, B.S., Muhlert, N., Tur, C., Edden, R.A., Wheeler-Kingshott, C.A., Miller, D.H., Thompson, A.J., Ciccarelli, O., 2015. Reduced gamma-aminobutyric acid concentration is associated with physical disability in progressive multiple sclerosis. Brain 138, 2584-2595.

Chadzynski, G.L., Bender, B., Groeger, A., Erb, M., Klose, U., 2011. Tissue specific resonance frequencies of water and metabolites within the human brain. Journal of Magnetic Resonance 212, 55-63.

Chang, P., Nassirpour, S., Henning, A., 2018. Modeling real shim fields for very high degree (and order) B0 shimming of the human brain at 9.4 T. Magnetic Resonance in Medicine 79, 529-540.

Chen, C., Morris, P., Francis, S., Gowland, P., 2015. A comparison of MEGA-sLASER and STEAM for in vivo quantification of GABA at 7T. Proc. Int. Soc. Magn. Reson. Med, p. 0203.

Chen, C., Sigurdsson, H.P., Pépés, S.E., Auer, D.P., Morris, P.G., Morgan, P.S., Gowland, P.A., Jackson, S.R., 2017. Activation induced changes in GABA: functional MRS at 7 T with MEGA-sLASER. Neuroimage 156, 207-213.

Chen, M., Li, G., Zhang, Z., Chen, L., Pei, M., Yan, X., Li, J., 2016. The anterior cingulate cortex GABA levels with varied tissue composition measured by in vivo single voxel MRS. Proc. Int. Soc. Magn. Reson. Med.

Choi, C., Banerjee, A., Ganji, S., Dimitrov, I., Ghose, S., Tamminga, C., 2012a. Contamination-free measurement of GABA in the human brain by optimized PRESS at 7.0 T in vivo Proc. Intl. Soc. Mag. Reson. Med.

Choi, C., Bhardwaj, P.P., Kalra, S., Casault, C.A., Yasmin, U.S., Allen, P.S., Coupland, N.J., 2007. Measurement of GABA and contaminants in gray and white matter in human brain in vivo. Magnetic Resonance in Medicine 58, 27-33.

Choi, C., Ganji, S.K., DeBerardinis, R.J., Hatanpaa, K.J., Rakheja, D., Kovacs, Z., Yang, X.-L., Mashimo, T., Raisanen, J.M., Marin-Valencia, I., 2012b. 2-hydroxyglutarate detection by magnetic resonance spectroscopy in IDH-mutated patients with gliomas. Nature Medicine 18, 624.

Choi, I.-Y., Lee, S.-P., Merkle, H., Shen, J., 2006. In vivo detection of gray and white matter differences in GABA concentration in the human brain. Neuroimage 33, 85-93.

Chowdhury, F.A., O'Gorman, R.L., Nashef, L., Elwes, R.D., Edden, R.A., Murdoch, J.B., Barker, G.J., Richardson, M.P., 2015. Investigation of glutamine and GABA levels in patients with idiopathic generalized epilepsy using MEGAPRESS. Journal of Magnetic Resonance Imaging 41, 694-699.

D'Hulst, C., Heulens, I., Van der Aa, N., Goffin, K., Koole, M., Porke, K., Van De Velde, M., Rooms, L., Van Paesschen, W., Van Esch, H., 2015. Positron Emission Tomography (PET) Quantification of GABAA Receptors in the Brain of Fragile X Patients. PloS One 10, e0131486.

De Graaf, A., Van Dijk, J., BoéE, W., 1990. QUALITY: quantification improvement by converting lineshapes to the Lorentzian type. Magnetic Resonance in Medicine 13, 343-357.

De Graaf, R.A., Pan, J.W., Telang, F., Lee, J.-H., Brown, P., Novotny, E.J., Hetherington, H.P., Rothman, D.L., 2001. Differentiation of glucose transport in human brain gray and white matter. Journal of Cerebral Blood Flow and Metabolism 21, 483-492.

Deelchand, D.K., Van de Moortele, P.-F., Adriany, G., Iltis, I., Andersen, P., Strupp, J.P., Vaughan, J.T., Uğurbil, K., Henry, P.-G., 2010. In vivo 1H NMR spectroscopy of the human brain at 9.4 T: initial results. Journal of Magnetic Resonance 206, 74-80.

Dong, Z., Peterson, B.S., 2009. Spectral resolution amelioration by deconvolution (SPREAD) in MR spectroscopic imaging. Journal of Magnetic Resonance Imaging 29, 1395-1405.

Dong, Z., Zhang, Y., Liu, F., Duan, Y., Kangarlu, A., Peterson, B.S., 2014. Improving the spectral resolution and spectral fitting of 1H MRSI data from human calf muscle by the SPREAD technique. NMR in Biomedicine 27, 1325-1332.

Durst, C.R., Michael, N., Tustison, N.J., Patrie, J.T., Raghavan, P., Wintermark, M., Velan, S.S., 2015. Noninvasive evaluation of the regional variations of GABA using magnetic resonance spectroscopy at 3 Tesla. Magnetic Resonance Imaging 33, 611-617.

Duyn, J.H., van Gelderen, P., Li, T.-Q., de Zwart, J.A., Koretsky, A.P., Fukunaga, M., 2007. High-field MRI of brain cortical substructure based on signal phase. Proceedings of the National Academy of Sciences 104, 11796-11801.

Dyke, K., Pépés, S.E., Chen, C., Kim, S., Sigurdsson, H.P., Draper, A., Husain, M., Nachev, P., Gowland, P.A., Morris, P.G., 2017. Comparing GABA-dependent physiological measures of inhibition with proton magnetic resonance spectroscopy measurement of GABA using ultra-high-field MRI. Neuroimage 152, 360-370.

Edden, R.A., Intrapiromkul, J., Zhu, H., Cheng, Y., Barker, P.B., 2012a. Measuring T2 in vivo with J-difference editing: Application to GABA at 3 tesla. Journal of Magnetic Resonance Imaging 35, 229-234.

Edden, R.A., Puts, N.A., Barker, P.B., 2012b. Macromolecule□suppressed GABA-edited magnetic resonance spectroscopy at 3T. Magnetic Resonance in Medicine 68, 657-661.

Erdogmus, D., Yan, R., Larsson, E.G., Principe, J.C., Fitzsimmons, J.R., 2004. Image construction methods for phased array magnetic resonance imaging. Journal of Magnetic Resonance Imaging 20, 306-314.

Ernst, T., Kreis, R., Ross, B., 1993. Absolute quantitation of water and metabolites in the human brain. I. Compartments and water. Journal of Magnetic Resonance, Series B 102, 1-8.

Fisher, S.K., Novak, J.E., Agranoff, B.W., 2002. Inositol and higher inositol phosphates in neural tissues: homeostasis, metabolism and functional significance. Journal of Neurochemistry 82, 736-754.

Frahm, J., Merboldt, K.-D., Hänicke, W., 1987. Localized proton spectroscopy using stimulated echoes. Journal of Magnetic Resonance (1969) 72, 502-508.

Fukunaga, M., Li, T.-Q., van Gelderen, P., de Zwart, J.A., Shmueli, K., Yao, B., Lee, J., Maric, D., Aronova, M.A., Zhang, G., 2010. Layer-specific variation of iron content in cerebral cortex as a source of MRI contrast. Proceedings of the National Academy of Sciences 107, 3834-3839.

Ganji, S.K., An, Z., Banerjee, A., Madan, A., Hulsey, K.M., Choi, C., 2014. Measurement of regional variation of GABA in the human brain by optimized point-resolved spectroscopy at 7 T in vivo. NMR in Biomedicine 27, 1167-1175.

Gasparovic, C., Yeo, R., Mannell, M., Ling, J., Elgie, R., Phillips, J., Doezema, D., Mayer, A.R., 2009. Neurometabolite concentrations in gray and white matter in mild traumatic brain injury: an 1H–magnetic resonance spectroscopy study. Journal of Neurotrauma 26, 1635-1643.

Geramita, M., van der Veen, J.W., Barnett, A.S., Savostyanova, A.A., Shen, J., Weinberger, D.R., Marenco, S., 2011. Reproducibility of prefrontal γ-aminobutyric acid measurements with J□edited spectroscopy. NMR in Biomedicine 24, 1089-1098.

Godlewska, B.R., Clare, S., Cowen, P.J., Emir, U.E., 2017a. Ultra-high-field magnetic resonance spectroscopy in psychiatry. Frontiers in psychiatry 8, 123.

Godlewska, B.R., Pike, A., Sharpley, A.L., Ayton, A., Park, R.J., Cowen, P.J., Emir, U.E., 2017b. Brain glutamate in anorexia nervosa: a magnetic resonance spectroscopy case control study at 7 Tesla. Psychopharmacology 234, 421-426.

Govind, V., Young, K., Maudsley, A.A., 2015. Corrigendum: Proton NMR chemical shifts and coupling constants for brain metabolites. Govindaraju V, Young K, Maudsley AA, NMR Biomed. 2000; 13: 129–153. NMR in Biomedicine 28, 923-924.

Govindaraju, V., Young, K., Maudsley, A.A., 2000. Proton NMR chemical shifts and coupling constants for brain metabolites. NMR in Biomedicine 13, 129-153.

Granot, J., 1986. Selected volume excitation using stimulated echoes (VEST). Applications to spatially localized spectroscopy and imaging. Journal of Magnetic Resonance (1969) 70, 488-492.

Griswold, M.A., Jakob, P.M., Heidemann, R.M., Nittka, M., Jellus, V., Wang, J., Kiefer, B., Haase, A., 2002. Generalized autocalibrating partially parallel acquisitions (GRAPPA). Magnetic Resonance in Medicine: An Official Journal of the International Society for Magnetic Resonance in Medicine 47, 1202-1210.

Gruetter, R., Tkáč, I., 2000. Field mapping without reference scan using asymmetric echo-planar techniques. Magnetic Resonance in Medicine 43, 319-323.

Haacke, E.M., Cheng, N.Y., House, M.J., Liu, Q., Neelavalli, J., Ogg, R.J., Khan, A., Ayaz, M., Kirsch, W., Obenaus, A., 2005. Imaging iron stores in the brain using magnetic resonance imaging. Magnetic Resonance Imaging 23, 1-25.

Hall, E.L., Stephenson, M.C., Price, D., Morris, P.G., 2014. Methodology for improved detection of low concentration metabolites in MRS: optimised combination of signals from multi-element coil arrays. Neuroimage 86, 35-42.

Hardy, C.J., Bottomley, P.A., Rohling, K.W., Roemer, P.B., 1992. An NMR phased array for human cardiac 31P spectroscopy. Magnetic Resonance in Medicine 28, 54-64.

Harris, A.D., Glaubitz, B., Near, J., John Evans, C., Puts, N.A., Schmidt-Wilcke, T., Tegenthoff, M., Barker, P.B., Edden, R.A., 2014. Impact of frequency drift on gamma-aminobutyric acid-edited MR spectroscopy. Magnetic Resonance in Medicine 72, 941-948.

He, X., Yablonskiy, D.A., 2009. Biophysical mechanisms of phase contrast in gradient echo MRI. Proceedings of the National Academy of Sciences 106, 13558-13563.

Hofmann, L., Slotboom, J., Jung, B., Maloca, P., Boesch, C., Kreis, R., 2002. Quantitative 1H-magnetic resonance spectroscopy of human brain: Influence of composition and parameterization of the basis set in linear combination model-fitting. Magnetic Resonance in Medicine 48, 440-453.

Houtepen, L.C., Schür, R.R., Wijnen, J.P., Boer, V.O., Boks, M., Kahn, R.S., Joëls, M., Klomp, D.W., Vinkers, C.H., 2017. Acute stress effects on GABA and glutamate levels in the prefrontal cortex: A 7T 1H magnetic resonance spectroscopy study. NeuroImage: Clinical 14, 195-200.

Intrapiromkul, J., Zhu, H., Cheng, Y., Barker, P.B., Edden, R.A., 2013. Determining the in vivo transverse relaxation time of GABA in the human brain at 7T. Journal of Magnetic Resonance Imaging 38, 1224-1229.

Ip, I.B., Berrington, A., Hess, A.T., Parker, A.J., Emir, U.E., Bridge, H., 2017. Combined fMRI-MRS acquires simultaneous glutamate and BOLD-fMRI signals in the human brain. Neuroimage 155, 113-119.

Jensen, J.E., Renshaw, P.F., 2005. Grey and white matter GABA level differences in the human brain using two-dimensional, J-resolved spectroscopic imaging. NMR in Biomedicine 18, 570-576.

Joanna, L., James, P., Anthony, A., Garnette, R.S., 1993. Nuclear magnetic resonance study of cerebrospinal fluid from patients with multiple sclerosis. Canadian Journal of Neurological Sciences 20, 194-198.

Keltner, J.R., Wald, L.L., Christensen, J.D., Maas, L.C., Moore, C.M., Cohen, B.M., Renshaw, P.F., 1996. A technique for detecting GABA in the human brain with PRESS localization and optimized refocusing spectral editing radiofrequency pulses. Magnetic Resonance in Medicine 36, 458-461.

Khiat, A., Bard, C., Lacroix, A., Boulanger, Y., 2000. Recovery of the brain choline level in treated Cushing's patients as monitored by proton magnetic resonance spectroscopy. Brain Research 862, 301-307.

Kimmich, R., Hoepfel, D., 1987. Volume-selective multipulse spin-echo spectroscopy. Journal of Magnetic Resonance (1969) 72, 379-384.

Klose, U., 1990. In vivo proton spectroscopy in presence of eddy currents. Magnetic Resonance in Medicine 14, 26-30.

Kreis, R., 1997. Quantitative localized 1 H MR spectroscopy for clinical use. Progress in nuclear magnetic resonance spectroscopy 31, 155-195.

Kreis, R., 2004. Issues of spectral quality in clinical 1H-magnetic resonance spectroscopy and a gallery of artifacts. NMR in Biomedicine 17, 361-381.

Kreis, R., 2016. The trouble with quality filtering based on relative Cramér-Rao lower bounds. Magnetic Resonance in Medicine 75, 15-18.

Kreis, R., Ernst, T., Ross, B., 1993. Absolute quantitation of water and metabolites in the human brain. II. Metabolite concentrations. Journal of Magnetic Resonance, Series B 102, 9-19.

Kreis, R., Slotboom, J., Hofmann, L., Boesch, C., 2005. Integrated data acquisition and processing to determine metabolite contents, relaxation times, and macromolecule baseline in single examinations of individual subjects. Magnetic Resonance in Medicine 54, 761-768.

Lee, J., Hirano, Y., Fukunaga, M., Silva, A.C., Duyn, J.H., 2010a. On the contribution of deoxy-hemoglobin to MRI gray–white matter phase contrast at high field. Neuroimage 49, 193-198.

Lee, J., Shmueli, K., Fukunaga, M., van Gelderen, P., Merkle, H., Silva, A.C., Duyn, J.H., 2010b. Sensitivity of MRI resonance frequency to the orientation of brain tissue microstructure. Proceedings of the National Academy of Sciences 107, 5130-5135.

Lemke, C., Hess, A., Clare, S., Bachtiar, V., Stagg, C., Jezzard, P., Emir, U., 2015. Two-voxel spectroscopy with dynamic B0 shimming and flip angle adjustment at 7 T in the human motor cortex. NMR in Biomedicine 28, 852-860.

Levenberg, K., 1944. A method for the solution of certain non-linear problems in least squares. Quarterly of applied mathematics 2, 164-168.

Li, N., An, L., Shen, J., 2015. Spectral fitting using basis set modified by measured B0 field distribution. NMR in Biomedicine 28, 1707-1715.

Li, W., Wu, B., Batrachenko, A., Bancroft-Wu, V., Morey, R.A., Shashi, V., Langkammer, C., Bellis, M.D., Ropele, S., Song, A.W., 2014. Differential developmental trajectories of magnetic susceptibility in human brain gray and white matter over the lifespan. Human Brain Mapping 35, 2698-2713.

Li, Y., Xu, D., Ozturk-Isik, E., Lupo, J., Chen, A., Vigneron, D., Nelson, S., 2012. T1 and T2 metabolite relaxation times in normal brain at 3T and 7T. J Mol Imaging

Dynam S 1, 002.

Lingford-Hughes, A., Hume, S.P., Feeney, A., Hirani, E., Osman, S., Cunningham, V.J., Pike, V.W., Brooks, D.J., Nutt, D.J., 2002. Imaging the GABA-benzodiazepine receptor subtype containing the α5-subunit in vivo with [11C] Ro15 4513 positron emission tomography. Journal of Cerebral Blood Flow and Metabolism 22, 878-889.

Liu, C., Li, W., Johnson, G.A., Wu, B., 2011. High-field (9.4T) MRI of brain dysmyelination by quantitative mapping of magnetic susceptibility. Neuroimage 56, 930-938.

Luo, J., He, X., Andre'd'Avignon, D., Ackerman, J.J., Yablonskiy, D.A., 2010. Protein-induced water 1 H MR frequency shifts: contributions from magnetic susceptibility and exchange effects. Journal of Magnetic Resonance 202, 102-108.

Lutz, N., Kuesel, A., Hull, W., 1993. A 1H-NMR method for determining temperature in cell culture perfusion systems. Magnetic Resonance in Medicine 29, 113-118.

Marjańska, M., Auerbach, E.J., Valabrègue, R., de Moortele, V., Adriany, G., Garwood, M., 2012. Localized 1H NMR spectroscopy in different regions of human brain in vivo at 7 T: T2 relaxation times and concentrations of cerebral metabolites. NMR in Biomedicine 25, 332-339.

Marques, J.P., Maddage, R., Mlynarik, V., Gruetter, R., 2009. On the origin of the MR image phase contrast: an in vivo MR microscopy study of the rat brain at 14.1 T. Neuroimage 46, 345-352.

Marshall, I., Higinbotham, J., Bruce, S., Freise, A., 1997. Use of voigt lineshape for quantification of in vivo1H spectra. Magnetic Resonance in Medicine 37, 651-657.

Marsman, A., Mandl, R.C., Klomp, D.W., Bohlken, M.M., Boer, V.O., Andreychenko, A., Cahn, W., Kahn, R.S., Luijten, P.R., Pol, H.E.H., 2014. GABA and glutamate in schizophrenia: A 7 T 1H-MRS study. NeuroImage: Clinical 6, 398-407.

Maudsley, A., 1995. Spectral lineshape determination by self-deconvolution. Journal of Magnetic Resonance, Series B 106, 47-57.

Maudsley, A., Darkazanli, A., Alger, J., Hall, L., Schuff, N., Studholme, C., Yu, Y., Ebel, A., Frew, A., Goldgof, D., 2006. Comprehensive processing, display and analysis for in vivo MR spectroscopic imaging. NMR in Biomedicine 19, 492-503.

Maudsley, A.A., 2004. Evaluation of variable line□shape models and prior information in automated 1H spectroscopic imaging analysis. Magnetic Resonance in Medicine 52, 1246-1254.

Maudsley, A.A., Domenig, C., Govind, V., Darkazanli, A., Studholme, C., Arheart, K., Bloomer, C., 2009. Mapping of brain metabolite distributions by volumetric proton MR spectroscopic imaging (MRSI). Magnetic Resonance in Medicine 61, 548-559.

Maudsley, A.A., Goryawala, M.Z., Sheriff, S., 2016. Effects of tissue susceptibility on brain temperature mapping. Neuroimage.

Maudsley, A.A., Goryawala, M.Z., Sheriff, S., 2017. Effects of tissue susceptibility on brain temperature mapping. Neuroimage 146, 1093-1101.

McCormick, D.A., 1989. GABA as an inhibitory neurotransmitter in human cerebral cortex. Journal of Neurophysiology 62, 1018-1027.

Mescher, M., Merkle, H., Kirsch, J., Garwood, M., Gruetter, R., 1998. Simultaneous in vivo spectral editing and water suppression. NMR in Biomedicine 11, 266-272.

Mescher, M., Tannus, A., Johnson, M.N., Garwood, M., 1996. Solvent suppression using selective echo dephasing. Journal of Magnetic Resonance, Series A 123, 226-229.

Mikkelsen, M., Singh, K.D., Brealy, J.A., Linden, D.E., Evans, C.J., 2016a. Quantification of γ-aminobutyric acid (GABA) in 1H MRS volumes composed heterogeneously of grey and white matter. NMR in Biomedicine 29, 1644-1655.

Mikkelsen, M., Singh, K.D., Sumner, P., Evans, C.J., 2016b. Comparison of the repeatability of GABA-edited magnetic resonance spectroscopy with and without macromolecule suppression. Magnetic Resonance in Medicine 75, 946-953.

Miller, B.L., Changl, L., Booth, R., Ernst, T., Cornford, M., Nikas, D., McBride, D., Jenden, D.J., 1996. In vivo1H MRS choline: Correlation with in vitro chemistry/ histology. Life Sciences 58, 1929-1935.

Morris, G.A., 1988. Compensation of instrumental imperfections by deconvolution using an internal reference signal. Journal of Magnetic Resonance (1969) 80, 547-552.

Mugler, J.P., Brookeman, J.R., 1990. Three-dimensional magnetization-prepared rapid gradient-echo imaging (3D MP RAGE). Magnetic Resonance in Medicine 15, 152-157.

Mullins, P.G., McGonigle, D.J., O'gorman, R.L., Puts, N.A., Vidyasagar, R., Evans, C.J., Edden, R.A., 2014. Current practice in the use of MEGA-PRESS spectroscopy for the detection of GABA. Neuroimage 86, 43-52.

Nagamitsu, S., Sakurai, R., Matsuoka, M., Chiba, H., Ozono, S., Tanigawa, H., Yamashita, Y., Kaida, H., Ishibashi, M., Kakuma, T., 2016. Altered SPECT 123I-iomazenil Binding in the Cingulate Cortex of Children with Anorexia Nervosa. Frontiers in psychiatry 7.

Napolitano, A., Kockenberger, W., Auer, D.P., 2013. Reliable gamma aminobutyric acid measurement using optimized PRESS at 3 T. Magnetic Resonance in Medicine 69, 1528-1533.

Naressi, A., Couturier, C., Castang, I., De Beer, R., Graveron-Demilly, D., 2001a. Java-based graphical user interface for MRUI, a software package for quantitation of in vivo/medical magnetic resonance spectroscopy signals. Computers in Biology and Medicine 31, 269-286.

Naressi, A., Couturier, C., Devos, J., Janssen, M., Mangeat, C., De Beer, R., Graveron-Demilly, D., 2001b. Java-based graphical user interface for the MRUI

quantitation package. Magnetic Resonance Materials in Physics, Biology and Medicine 12, 141.

Near, J., Andersson, J., Maron, E., Mekle, R., Gruetter, R., Cowen, P., Jezzard, P., 2013. Unedited in vivo detection and quantification of γ-aminobutyric acid in the occipital cortex using short-TE MRS at 3 T. NMR in Biomedicine 26, 1353-1362.

Nguyen, H.M., Peng, X., Do, M.N., Liang, Z.-P., 2013. Denoising MR spectroscopic imaging data with low-rank approximations. IEEE Transactions on Biomedical Engineering 60, 78-89.

Nicolay, K., Braun, K.P., Graaf, R.A.d., Dijkhuizen, R.M., Kruiskamp, M.J., 2001. Diffusion NMR spectroscopy. NMR in Biomedicine 14, 94-111.

Oblak, A.L., Gibbs, T.T., Blatt, G.J., 2011. Reduced GABA A receptors and benzodiazepine binding sites in the posterior cingulate cortex and fusiform gyrus in autism. Brain Research 1380, 218-228.

Ogg, R.J., Kingsley, R., Taylor, J.S., 1994. WET, a T1-and B1-insensitive water-suppression method for in vivo localized 1H NMR spectroscopy. Journal of Magnetic Resonance, Series B 104, 1-10.

Ogg, R.J., Langston, J.W., Haacke, E.M., Steen, R.G., Taylor, J.S., 1999. The correlation between phase shifts in gradient-echo MR images and regional brain iron concentration. Magnetic Resonance Imaging 17, 1141-1148.

Öngür, D., Prescot, A.P., McCarthy, J., Cohen, B.M., Renshaw, P.F., 2010. Elevated gamma-aminobutyric acid levels in chronic schizophrenia. Biological Psychiatry 68, 667-670.

Ordidge, R., Cresshull, I., 1986. The correction of transient B0 field shifts following the application of pulsed gradients by phase correction in the time domain. Journal of Magnetic Resonance (1969) 69, 151-155.

Ordidge, R.J., Connelly, A., Lohman, J.A., 1986. Image-selected in vivo spectroscopy (ISIS). A new technique for spatially selective NMR spectroscopy. Journal of Magnetic Resonance (1969) 66, 283-294.

Öz, G., Terpstra, M., Tkáč, I., Aia, P., Lowary, J., Tuite, P.J., Gruetter, R., 2006. Proton MRS of the unilateral substantia nigra in the human brain at 4 tesla: detection of high GABA concentrations. Magnetic Resonance in Medicine: An Official Journal of the International Society for Magnetic Resonance in Medicine 55, 296-301.

Perry, T., Berry, K., Hansen, S., Diamond, S., Mok, C., 1971a. Regional distribution of amino acids in human brain obtained at autopsy. Journal of Neurochemistry 18, 513-519.

Perry, T., Hansen, S., Berry, K., Mok, C., Lesk, D., 1971b. Free amino acids and related compounds in biopsies of human brain. Journal of Neurochemistry 18, 521-528.

Peters, R.T., Hinks, R.S., Henkelman, R.M., 1998. Ex vivo tissue-type independence in proton-resonance frequency shift MR thermometry. Magnetic Resonance in Medicine 40, 454-459.

Petroff, O.A., Rothman, D.L., Behar, K.L., Mattson, R.H., 1995. Initial Observations on Effect of Vigabatrin on In Vivo 1H Spectroscopic Measurements of γ-Aminobutyric Acid, Glutamate, and Glutamine in Human Brain. Epilepsia 36, 457-464.

Poullet, J.B., Sima, D.M., Simonetti, A.W., De Neuter, B., Vanhamme, L., Lemmerling, P., Van Huffel, S., 2007. An automated quantitation of short echo time MRS spectra in an open source software environment: AQSES. NMR in Biomedicine: An International Journal Devoted to the Development and Application of Magnetic Resonance In vivo 20, 493-504.

Pouwels, P.J., Frahm, J., 1998. Regional metabolite concentrations in human brain as determined by quantitative localized proton MRS. Magnetic Resonance in Medicine 39, 53-60.

Považan, M., Strasser, B., Hangel, G., Heckova, E., Gruber, S., Trattnig, S., Bogner, W., 2018. Simultaneous mapping of metabolites and individual macromolecular components via ultra-short acquisition delay 1H MRSI in the brain at 7T. Magnetic Resonance in Medicine 79, 1231-1240.

Pradhan, S., Bonekamp, S., Gillen, J.S., Rowland, L.M., Wijtenburg, S.A., Edden, R.A., Barker, P.B., 2015. Comparison of single voxel brain MRS AT 3 T and 7 T using 32-channel head coils. Magnetic Resonance Imaging 33, 1013-1018.

Pradhan, S., Soher, B.J., Barker, P.B., 2016. Quantifying Spectra in the Frequency Domain. eMagRes.

Provencher, S.W., 1993. Estimation of metabolite concentrations from localized in vivo proton NMR spectra. Magnetic Resonance in Medicine 30, 672-679.

Provencher, S.W., 2001. Automatic quantitation of localized in vivo1H spectra with LCModel. NMR in Biomedicine 14, 260-264.

Provencher, S.W., 2016. LCModel & LCMgui user's manual. LCModel Version, 6.3-1L.

Pruessmann, K.P., Weiger, M., Scheidegger, M.B., Boesiger, P., 1999. SENSE: sensitivity encoding for fast MRI. Magnetic Resonance in Medicine 42, 952-962.

Purcell, E.M., Torrey, H., Pound, R.V., 1946. Resonance absorption by nuclear magnetic moments in a solid. Physical Review 69, 37.

Puts, N.A., Edden, R.A., 2012. In vivo magnetic resonance spectroscopy of GABA: a methodological review. Progress in nuclear magnetic resonance spectroscopy 60, 29-41.

Ramsey, N., Purcell, E., 1952. Interactions between nuclear spins in molecules. Physical Review 85, 143.

Raschke, F., Fuster-Garcia, E., Opstad, K., Howe, F., 2012. Classification of single-voxel 1H spectra of brain tumours using LCModel. NMR in Biomedicine 25, 322-

331.

Reichenbach, J.R., Venkatesan, R., Schillinger, D.J., Kido, D.K., Haacke, E.M., 1997. Small vessels in the human brain: MR venography with deoxyhemoglobin as an intrinsic contrast agent. Radiology 204, 272-277.

Richardson, M., Koepp, M., Duncan, J., Brooks, D., Fish, D., 1996. Benzodiazepine receptors in focal epilepsy with cortical dysgenesis: An 11C-flumazenil PET study. Annals of Neurology 40, 188-198.

Rodgers, C.T., Robson, M.D., 2016. Coil combination for receive array spectroscopy: Are data-driven methods superior to methods using computed field maps? Magnetic Resonance in Medicine 75, 473-487.

Roemer, P.B., Edelstein, W.A., Hayes, C.E., Souza, S.P., Mueller, O., 1990. The NMR phased array. Magnetic Resonance in Medicine 16, 192-225.

Rohani Rankouhi, S., Hong, D., Dyvorne, H., Balchandani, P., Norris, D.G., 2018. MASE-sLASER, a short-TE, matched chemical shift displacement error sequence for single-voxel spectroscopy at ultrahigh field. NMR in Biomedicine 31, e3940.

Rothman, D.L., Petroff, O., Behar, K.L., Mattson, R.H., 1993. Localized 1H NMR measurements of gamma-aminobutyric acid in human brain in vivo. Proceedings of the National Academy of Sciences 90, 5662-5666.

Sanaei Nezhad, F., Anton, A., Parkes, L.M., Deakin, B., Williams, S.R., 2017. Quantification of glutathione in the human brain by MR spectroscopy at 3 Tesla: Comparison of PRESS and MEGA-PRESS. Magnetic Resonance in Medicine 78, 1257-1266.

Scheenen, T.W., Heerschap, A., Klomp, D.W., 2008a. Towards 1H-MRSI of the human brain at 7T with slice-selective adiabatic refocusing pulses. Magnetic Resonance Materials in Physics, Biology and Medicine 21, 95.

Scheenen, T.W., Klomp, D.W., Wijnen, J.P., Heerschap, A., 2008b. Short echo time 1H-MRSI of the human brain at 3T with minimal chemical shift displacement errors using adiabatic refocusing pulses. Magnetic Resonance in Medicine 59, 1-6.

Schulte, R.F., Boesiger, P., 2006. ProFit: two-dimensional prior-knowledge fitting of J-resolved spectra. NMR in Biomedicine 19, 255-263.

Shen, J., Rothman, D.L., Brown, P., 2002. In vivo GABA editing using a novel doubly selective multiple quantum filter. Magnetic Resonance in Medicine 47, 447-454.

Shmueli, K., Dodd, S.J., Li, T.Q., Duyn, J.H., 2011. The contribution of chemical exchange to MRI frequency shifts in brain tissue. Magnetic Resonance in Medicine 65, 35-43.

Shungu, D.C., Mao, X., Gonzales, R., Soones, T.N., Dyke, J.P., Veen, J.W., Kegeles, L.S., 2016. Brain γ-aminobutyric acid (GABA) detection in vivo with the J-editing 1H MRS technique: a comprehensive methodological evaluation of sensitivity enhancement, macromolecule contamination and test–retest reliability. NMR

in Biomedicine 29, 932-942.

Sima, D., Garcia, M.O., Poullet, J., Suvichakorn, A., Antoine, J.-P., Van Huffel, S., Van Ormondt, D., 2009. Lineshape estimation for magnetic resonance spectroscopy (MRS) signals: self-deconvolution revisited. Measurement Science and Technology 20, 104031.

Sima, D.M., Van Huffel, S., 2006. Regularized semiparametric model identification with application to nuclear magnetic resonance signal quantification with unknown macromolecular base-line. Journal of the Royal Statistical Society: Series B (Statistical Methodology) 68, 383-409.

Slotboom, J., Boesch, C., Kreis, R., 1998. Versatile frequency domain fitting using time domain models and prior knowledge. Magnetic Resonance in Medicine 39, 899-911.

Smith, S., Levante, T., Meier, B.H., Ernst, R.R., 1994. Computer simulations in magnetic resonance. An object-oriented programming approach. Journal of Magnetic Resonance, Series A 106, 75-105.

Soeiro-de-Souza, M.G., Pastorello, B.F., Leite, C.d.C., Henning, A., Moreno, R.A., Garcia Otaduy, M.C., 2016. Dorsal anterior cingulate lactate and glutathione levels in euthymic bipolar I disorder: 1H-MRS study. International Journal of Neuropsychopharmacology 19.

Soher, B.J., Young, K., Govindaraju, V., Maudsley, A.A., 1998. Automated spectral analysis III: application to in vivo proton MR spectroscopy and spectroscopic imaging. Magnetic Resonance in Medicine 40, 822-831.

Sotak, C.H., Freeman, D.M., 1988. A method for volume-localized lactate editing using zero-quantum coherence created in a stimulated-echo pulse sequence. Journal of Magnetic Resonance 77, 382-388.

Srinivasan, R., Ratiney, H., Hammond-Rosenbluth, K.E., Pelletier, D., Nelson, S.J., 2010. MR spectroscopic imaging of glutathione in the white and gray matter at 7 T with an application to multiple sclerosis. Magnetic Resonance Imaging 28, 163-170.

Starčuk, Z., Starčuková, J., 2016. Quantum-mechanical simulations for in vivo MR spectroscopy: Principles and possibilities demonstrated with the program NMRScopeB. Analytical Biochemistry.

Stefan, D., Di Cesare, F., Andrasescu, A., Popa, E., Lazariev, A., Vescovo, E., Strbak, O., Williams, S., Starcuk, Z., Cabanas, M., 2009. Quantitation of magnetic resonance spectroscopy signals: the jMRUI software package. Measurement Science and Technology 20, 104035.

Tal, A., Kirov, I.I., Grossman, R.I., Gonen, O., 2012. The role of gray and white matter segmentation in quantitative proton MR spectroscopic imaging. NMR in Biomedicine 25, 1392-1400.

Terpstra, M., Cheong, I., Lyu, T., Deelchand, D.K., Emir, U.E., Bednařík, P., Eberly, L.E., Öz, G., 2016. Test-retest reproducibility of neurochemical profiles with

short-echo, single-voxel MR spectroscopy at 3T and 7T. Magnetic Resonance in Medicine 76, 1083-1091.

Terpstra, M., Henry, P.G., Gruetter, R., 2003. Measurement of reduced glutathione (GSH) in human brain using LCModel analysis of difference-edited spectra. Magnetic Resonance in Medicine: An Official Journal of the International Society for Magnetic Resonance in Medicine 50, 19-23.

Terpstra, M., Vaughan, T., Ugurbil, K., Lim, K.O., Schulz, S.C., Gruetter, R., 2005. Validation of glutathione quantitation from STEAM spectra against edited 1H NMR spectroscopy at 4T: application to schizophrenia. Magnetic Resonance Materials in Physics, Biology and Medicine 18, 276.

Tkáč, I., Andersen, P., Adriany, G., Merkle, H., Uğurbil, K., Gruetter, R., 2001. In vivo 1H NMR spectroscopy of the human brain at 7 T. Magnetic Resonance in Medicine 46, 451-456.

Tkáč, I., Henry, P.G., Andersen, P., Keene, C.D., Low, W.C., Gruetter, R., 2004. Highly resolved in vivo 1H NMR spectroscopy of the mouse brain at 9.4 T. Magnetic Resonance in Medicine 52, 478-484.

Uğurbil, K., Adriany, G., Andersen, P., Chen, W., Garwood, M., Gruetter, R., Henry, P.-G., Kim, S.-G., Lieu, H., Tkac, I., 2003. Ultrahigh field magnetic resonance imaging and spectroscopy. Magnetic Resonance Imaging 21, 1263-1281.

Van der Veen, J., De Beer, R., Luyten, P., Van Ormondt, D., 1988. Accurate quantification of in vivo31P NMR signals using the variable projection method and prior knowledge. Magnetic Resonance in Medicine 6, 92-98.

Vanhamme, L., van den Boogaart, A., Van Huffel, S., 1997. Improved method for accurate and efficient quantification of MRS data with use of prior knowledge. Journal of Magnetic Resonance 129, 35-43.

Veen, J.W.v.d., Shen, J., 2013. Regional difference in GABA levels between medial prefrontal and occipital cortices. Journal of Magnetic Resonance Imaging 38, 745-750.

Verhoeff, N.P.L., Petroff, O.A., Hyder, F., Zoghbi, S.S., Fujita, M., Rajeevan, N., Rothman, D.L., Seibyl, J.P., Mattson, R.H., Innis, R.B., 1999. Effects of vigabatrin on the GABAergic system as determined by [123I] iomazenil SPECT and GABA MRS. Epilepsia 40, 1433-1438.

Wald, L.L., Moyher, S.E., Day, M.R., Nelson, S.J., Vigneron, D.B., 1995. Proton spectroscopic imaging of the human brain using phased array detectors. Magnetic Resonance in Medicine 34, 440-445.

Wijtenburg, S.A., Rowland, L.M., Edden, R.A., Barker, P.B., 2013. Reproducibility of brain spectroscopy at 7T using conventional localization and spectral editing techniques. Journal of Magnetic Resonance Imaging 38, 460-467.

Wilson, M., Reynolds, G., Kauppinen, R.A., Arvanitis, T.N., Peet, A.C., 2011. A constrained least-squares approach to the automated quantitation of in vivo 1H magnetic resonance spectroscopy data. Magnetic Resonance in Medicine

65, 1-12.

Wright, P., Mougin, O., Totman, J., Peters, A., Brookes, M., Coxon, R., Morris, P., Clemence, M., Francis, S., Bowtell, R., 2008. Water proton T1 measurements in brain tissue at 7, 3, and 1.5 T using IR-EPI, IR-TSE, and MPRAGE: results and optimization. Magnetic Resonance Materials in Physics, Biology and Medicine 21, 121.

Wu, Z., Mittal, S., Kish, K., Yu, Y., Hu, J., Haacke, E.M., 2009. Identification of calcification with MRI using susceptibility-weighted imaging: a case study. Journal of Magnetic Resonance Imaging 29, 177-182.

Xi, Y., Rocke, D.M., 2008. Baseline correction for NMR spectroscopic metabolomics data analysis. BMC Bioinformatics 9, 324.

Yan, G., Zhang, T., Dai, Z., Yi, M., Jia, Y., Nie, T., Zhang, H., Xiao, G., Wu, R., 2016. A Potential Magnetic Resonance Imaging Technique Based on Chemical Exchange Saturation Transfer for In Vivo γ-Aminobutyric Acid Imaging. PloS One 11, e0163765.

Yao, B., Li, T.-Q., van Gelderen, P., Shmueli, K., de Zwart, J.A., Duyn, J.H., 2009. Susceptibility contrast in high field MRI of human brain as a function of tissue iron content. Neuroimage 44, 1259-1266.

Zhang, Y., Li, S., Marenco, S., Shen, J., 2011. Quantitative measurement of N-acetyl-aspartyl-glutamate at 3 T using TE-averaged PRESS spectroscopy and regularized lineshape deconvolution. Magnetic Resonance in Medicine 66, 307-313.

Zhang, Y., Shen, J., 2013. Soft constraints in nonlinear spectral fitting with regularized lineshape deconvolution. Magnetic Resonance in Medicine 69, 912-919.

Zhang, Y., Shen, J., 2014. Smoothness of in vivo spectral baseline determined by mean-square error. Magnetic Resonance in Medicine 72, 913-922.

Zhang, Y., Shen, J., 2015. Simultaneous quantification of glutamate and glutamine by J-modulated spectroscopy at 3 Tesla. Magnetic Resonance in Medicine.

Zhong, K., Leupold, J., von Elverfeldt, D., Speck, O., 2008. The molecular basis for gray and white matter contrast in phase imaging. Neuroimage 40, 1561-1566.

Zhu, H., Edden, R.A., Ouwerkerk, R., Barker, P.B., 2011. High resolution spectroscopic imaging of GABA at 3 Tesla. Magnetic Resonance in Medicine 65, 603-609.